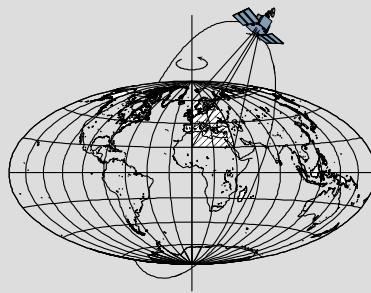# The Role of Glacial Isostatic Adjustment (GIA) Process On the Determination of Present-Day Sea-Level Rise

by

Zhenwei Huang

Report No. 504

Geodetic Science

The Ohio State University
Columbus, Ohio 43210

October 2013

The Role of Glacial Isostatic Adjustment (GIA) Process On the Determination of Present-Day Sea-Level Rise

by

Zhenwei Huang

Report No. 504

Geodetic Science

The Ohio State University

Columbus, Ohio 43210

October 2013

Preface

This report was prepared for and submitted to the Graduate School of The Ohio State University as a dissertation for partial fulfillment of the requirements for the Doctor of Philosophy (PhD) degree.

Abstract

Global sea-level rise has become one of the major social-economic hazards associated with the consequence of global warming. The global sea-level rise signal is largely measurable by using geodetic observations including tide gauge and radar altimetry, over the last century and a half, and during the last two decades, respectively. The changes in the steric component (due to changes in temperature and salinity) and the mass component of the sea-level can be measured by *in situ* hydrographic observations (expendable bathythermograph or XBT, mechanical bathythermograph or MBT, and Argo) over the last six decades, and by data from the spaceborne gravimetry twin-satellite mission, Gravity Recovery And Climate Experiment (GRACE) over the last decade, from 2002–2012, respectively. Geodetic measurements, including tide gauge, radar altimetry and GRACE, are contaminated by the ongoing glacial isostatic adjustment (GIA) process that is the viscoelastic response of the Earth to the loading of glaciation and deglaciation during a glacial cycle. Traditionally the GIA effect is removed from various geodetic sea-level observations by using a predicted correction from a GIA forward model.

In this study, theoretical treatment of how the GIA effect should be specifically addressed for correcting various geodetic sea-level observations is described, and the results of an accuracy assessment study using an ensemble of 15 contemporary GIA models is conducted to estimate the effect of the current GIA model uncertainty on sea-level and ice-sheet mass balance studies. We find that large discrepancies exist in contemporary GIA models and some of the models are not internally consistent with regard to the two theoretically predicted relations. Our result indicates that the GIA model errors could not be ignored in the study of the 20th century and present-day sea-level rise using modern geodetic measurements.

Using the elastic sea-level fingerprint method, recent change in Earth's dynamic oblateness (or J_2), 2003–2012, resulting from present-day ice sheet and mountain glacier/ice cap mass losses is studied. Sensitivity test and result shows that the contribution of mass loss from regions such as the glaciers systems in the Canadian Arctic Archipelago and Alaska are not negligible, although the dominant contributor remains the Antarctic and Greenland ice-sheets.

Combining different sea-level change observations (satellite altimetry, GRACE and Argo), published contemporary studies have claimed the ocean mass component of sea-level budget "closure", meaning that the two independent data types (de-steric satellite altimetry sea-level change and GRACE ocean bottom pressure change) agree with each other during 2004–2012. We argue that the sea-level budget is not closed, or it is a mis-closure depending on the choice of a particular GIA model to correct the GRACE data. The limitation is primarily due to the error in the current GIA models, followed by short or inadequate data span (less than 10 years), and errors in the observations. To mitigate the GIA model error, we develop a method to address the possibility to separate GIA signal and the present-day mass change over the ocean by combining GRACE and steric-corrected radar altimetry observations. For the first time, our result demonstrates a

potential separate of the GIA and present-day mass change signals, and thus proving an improved present-day mass component of the sea-level rise. The estimated averaged ocean GIA crustal uplift ranges from –0.49 to –0.65 mm/yr, compared to –0.29±0.08 mm/yr that is averaged using an ensemble of 14 GIA models. The estimated present-day ocean mass change causing sea level to rise between 2.23 and 2.39 mm/yr, as opposed to the steric-corrected sea level change from radar altimetry observations at 1.52 mm/yr. The limitation is the short data span and errors in the observations, including hydrographic data did not adequately sample the full depth of the ocean or in time, errors in the altimeter and GRACE data.

Table of Contents

Chapter 1   Introduction

1.1   Science Rationale and Global Sea-Level Rise

In the present time, about 200 million people are living within the coastal region or islands, and over two million km^2 of land are less than 1 meter above current sea level [*Stern and Britain*, 2006]. Sea-level rise, which is widely recognized as one of the consequences of anthropogenic climate change, has a substantial social and economic impact [*Shum and Kuo*, 2011].

The 2007 Intergovernmental Panel for Climate Change (IPCC) Fourth Assessment Report (AR4) concluded that the warming of the climate system is unequivocal, and with high certainty that the effect of human activities since 1750 has resulted in global warming [*IPCC*, 2007]. Observational evidence confirms that the anthropogenic increase of average air, land and ocean temperature, melting of snow and ice, and global sea-level rise. The 20th century and present-day sea-level rise are recognized to be measurable signals using tide gauges since the last century and a half, and Earth-orbiting satellite altimetry measurements over the past two decades [*Shum and Kuo,* 2011; 2013].

Quantifying and understanding the causes of the small rate of sea level rise at ~2 mm/yr remains challenging: the signal has a wide range of temporal and spatial scales resulting from complex interactions between various earth-atmosphere-ocean-cryosphere-hydrosphere processes [*Bindoff et al.*, 2007; *Cazenave and Llovel*, 2010; *Shum and Kuo*, 2011].

Global sea level is an indicator of climate change. It is sensitive to both steric change (thermal expansion and salinity change) of the oceans and the water exchange between land and ocean. The causes of sea-level change could be categorized as follows:

1. Ocean volume change results from temperature and salinity variations, which is also known as the steric effect.
2. Ocean mass change. It represents the water mass added into (or removed from) the oceans due to water exchanges in the Earth-atmosphere-hydrosphere-cryosphere system. These include water from polar ice sheets, mountain glaciers and ice caps, lakes, rivers, permafrost, ground water aquifers, dams or reservoirs, and the atmospheric or hydrologic process including precipitation, water vapor, evaporation and their feedbacks.
3. Ocean container change, which results from the ocean floor deformations (e.g., tectonics, glacial isostatic adjustment process etc.).

Sea level is measured in one of the two direct ways: (1) relative to the ocean floor (practically, this is measured by coastal and inland tide gauges and the observation is relative to the benchmark tied to the Earth's crust, known as 'relative sea level'), or (2)

relative to a global datum (practically, this is measured by satellite altimetry, known as the 'absolute sea level').

Recently, two observing system are put into operation to study sea-level change. The first one is Argo network, which is a global array of 3000 free-drifting profiling floats that measure the temperature and salinity of the upper 2000 m of the ocean. The regional array deployments start in 1999 and was scaled up to global deployments by 2004, by November 2007 the 3000-float array is achieved [*Roemmich et al.*, 2009]. Argo is an improved hydrographic system over the current existing drifting systems including expendable bathythermograph (XBT) and mechanical bathythermograph (MBT), which has been measuring the surface and subsurface ocean temperature and salinity over the last 5 decades [*Levitus et al.*, 2009]. The second one is the Gravity Recovery And Climate Experiment (GRACE) that launched in 2002, since then it has successfully provided information about the Earth's gravity field and its variations in monthly temporal and few hundred kilometers spatial resolution [*Tapley et al.*, 2004]. The variations of gravity field could be converted to the surface mass density changes based on the assumption that the primary cause of temporal changes in the Earth's gravity field is the water mass redistribution within a thin layer at the Earth's surface [*Wahr et al.*, 1998]. The derived surface mass density change could then be interpreted in terms of ocean bottom pressure change or equivalent surface elevation change for the purpose of sea-level study [*Chambers and Schroter*, 2011; *Chambers et al.*, 2004].

Figure 1.1 shows the estimated, observed, and projected global sea-level rise from 100BC to 2100. Significant acceleration started from ~1900, which is coincident with the Industrial Revolution. The pre-1900 is estimated based on geological interpretation [*Kemp et al.*, 2011]. Sea-level rise observations are from tide gauges and satellite altimetry [*Church and White*, 2011; *Shum and Kuo*, 2011]. The reconstructed sea-level record is using ocean model, tide gauge and altimetry measurements from 1950 to 2010 [*Meyssignac et al.*, 2012]. It is evident that the projected sea-level rise to the end of this century has a large discrepancy: the model-based (IPCC AR4) projection (lower bound) [*IPCC*, 2007] is an order of magnitude smaller than the empirical projection (upper bound) [*Rahmstorf et al.*, 2007; *Vermeer and Rahmstorf*, 2009]. Sea-level projection is very much needed but highly controversial. Understanding the causes of present sea level change will eventually lead to more accurate or robust of sea-level projection to the next century or beyond, and at the regional or local spatial resolutions for more practical applications.
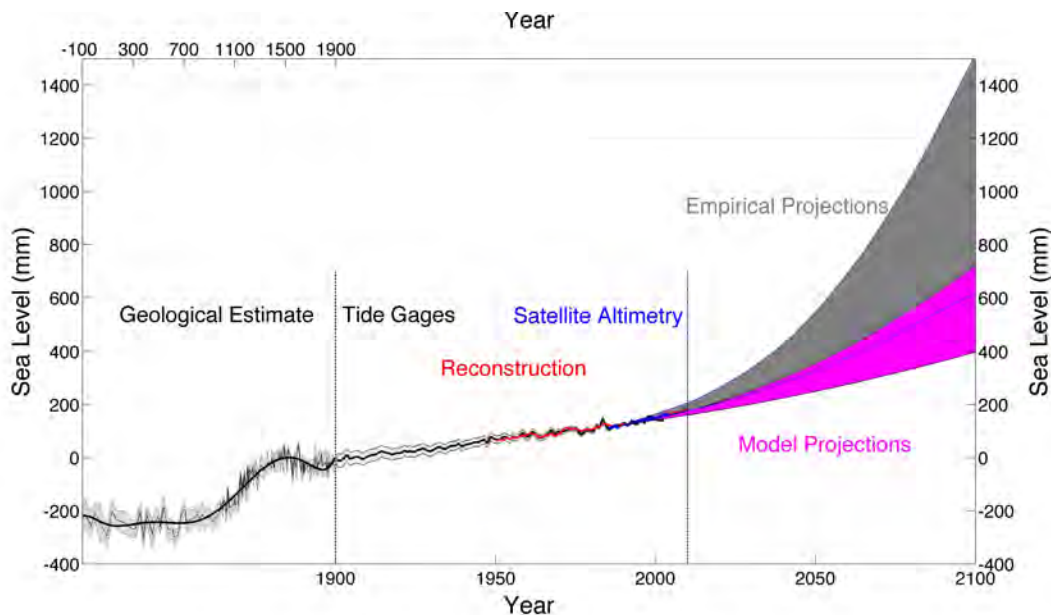
Figure 1.1 Estimated, observed, and projected global sea-level rise from 100BC to 2100. The pre-1900 sea-level rise estimate, –0.1 to 0.6 mm/yr is based on geological analysis [*Kemp et al.*, 2011], and the observed record is from tide gauges (black) and satellite altimetry (blue). The so-called reconstructed sea level record (red), 1950–2010, used ocean model, tide gauge and altimetry [*Meyssignac et al.*, 2012]. Model projected sea-level rise to 2100 (magenta envelop) is from IPCC AR4, and the thermal-only empirical projected sea-level rise to 2100 (grey envelop) is from *Rahmstorf et al.* [2007], *Vermeer and Rahmstorf* [2009], and *Kemp et al.* [2011]. Figure is adapted from *Shum and Kuo* [2013], and updated from *Shum and Kuo* [2011] and *Willis et al.* [2010]

The sea-level budget is closed when the sum of total geophysical contributions (polar ice sheets, mountain glaciers and ice caps, steric/thermal expansion, land water reservoirs, etc.) agree with the observed total sea-level change [*Cazenave et al.*, 2009; *Shum and Kuo*, 2011].

Global monitoring of the sea-level using satellite altimetry starts from the early 1990s, and ocean mass component could be measured by using GRACE satellite gravity mission since 2002. The steric component of sea-level based on spatial and temporal averaging [*Ishii and Kimoto*, 2009] are measured by hydrographic data since the 1950s, and most recently, are more accurately measured by globally sampled Argo array of profiling float starting from 2004.

This study primarily focuses on addressing the scientific question of sea-level budget closure for the opportunity when all the data are concurrently available, that is, GRACE data (2002 to present), satellite radar altimetry data (1992 to present), Argo and other hydrography data (2004 to present for Argo, and 1950 to present for XBT/MBTs). In our study the time period is chosen from 2004 to 2011. Over the overlapping period, combining Argo, satellite altimetry and GRACE, in principle, it is possible to separate the steric component and mass component changes in observed sea-level change and finally understanding the causes of the sea-level rise.

Recent studies have been conducted using data from Argo, satellite altimetry and GRACE to investigate the ocean mass component of the sea-level budget closure [*Cazenave et al.*, 2009; *Leuliette and Miller*, 2009; *Leuliette and Willis*, 2011; *Willis et al.*, 2008]. However, the observations made using satellite altimetry and GRACE are significantly influenced by the effect of ongoing glacial isostatic adjustment (GIA) process. To study this sea-level rise budget with the focus on ocean mass budget, it is necessary to remove GIA effect before interpreting the results. Unfortunately, in these studies this GIA correction they applied is neither consistent for radar altimetry and GRACE, nor same in the quantities. In terms of secular trend, for altimetry measurement, they all apply a number of –0.3 mm/yr to consider the ocean container change induced by GIA that computed from Peltier's GIA model [*Douglas and Peltier*, 2002]. For GRACE observations, *Willis et al.* [2008], *Leuliette and Miller* [2009], and *Leuliette and Willis* [2011] applied a near –1.0 mm/yr correction based on the model developed by *Paulson et al.* [2007], while *Cazenave et al.* [2009] applied a correction of –2.0 mm/yr based on *Peltier* [2009]. In addition, about the GIA correction for GRACE, considerable debate is still ongoing [*Chambers et al.*, 2010; *Peltier et al.*, 2012; *Tamisiea*, 2011].

In order to understand the sea-level rise and to investigate the ocean mass budget, it is vital to have improved understanding of the GIA process and its effect on various sea-level measurements using modern geodetic sensors.

1.2   Glacial Isostatic Adjustment (GIA) Process

Glacial isostatic adjustment is the response of solid Earth to the past changes in surface loading by ice and water (glaciation and deglaciation). During the last ice age, gigantic volumes of ice accumulated over North America, Scandinavia, Greenland and Antarctica, with thickness as large as 3–4 km, reaching its maximum about 21000 years ago, called the Last Glacial Maximum (LGM). Since then, these ancient ice-sheets began to melt, and the melting was completed approximately 4000 years ago with ice sheets disappeared over North America and Scandinavia and decreased its size over Greenland and Antarctica. The melted water flowed into the ocean and caused the sea-level rise. Overall, sea level has risen approximately 120 meters since the LGM [*Peltier*, 2004].
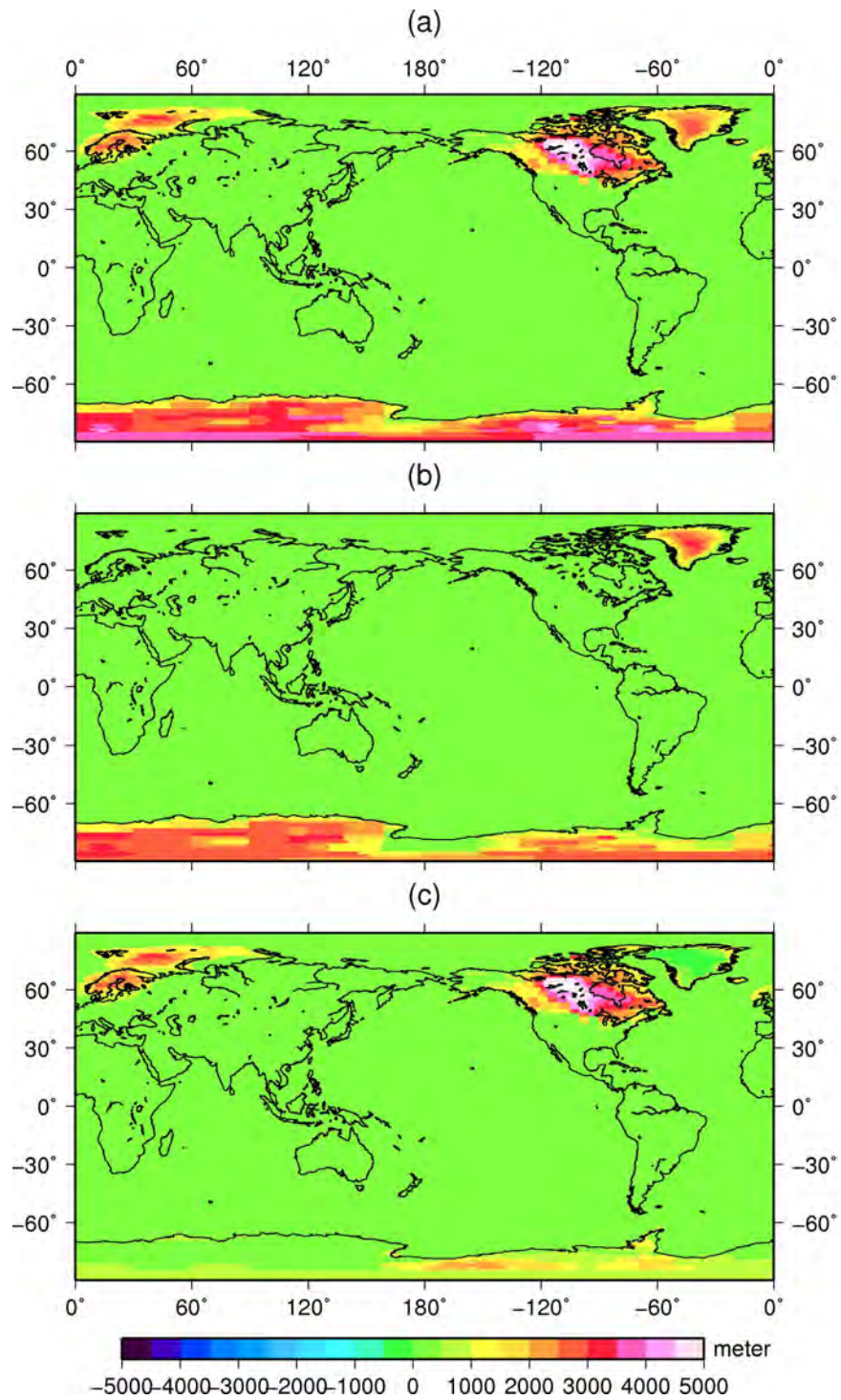
Figure 1.2 Ice thickness from ICE5G ice history model [*Peltier*, 2004]. (a) Ice thickness at the Last Glacial Maximum; (b) Ice thickness at present; (c) The difference of ice thickness between Last Glacial Maximum and present.

When the solid Earth underneath the ice-sheet was depressed during the Ice Age, mantle material flowed away from the loading center to the surrounding region and created a forebulge. When the ice melted away or decreased in size, this forebulge collapse and the mantle material flowed back to the glaciated region, causing the former to subside and the latter to uplift [*Douglas and Peltier*, 2002]. This geophysical process involving the response of the viscoelastic Earth to the loading resulting from deglaciation of ancient ice-sheets can still be observable. For example, the relaxation of Solid Earth from vanishing ice sheets is still ongoing and measures over a centimeter per year in the Hudson Bay area. The ongoing GIA process is viscous response that causes present-day crustal uplift or subsidence mainly near the LGM ice-sheet centers. In addition, Earth's gravity field also changes resulting from this large-scale mass redistribution inside the Earth in the GIA process.

Given the assumed known surface loading history and Earth parameters, GIA modelers could predict current GIA signals by GIA forward modeling. The predictions could be used to remove the GIA contribution from various observations and the residual could be used to study non-GIA related problems, such as polar ice mass balance, water exchanged between land and ocean [*Chen et al.*, 2006; *Velicogna and Wahr*, 2005]. Conversely, glacial isostatic adjustment observations, e.g. crustal displacement and gravity anomaly associated with the GIA process, which are the viscoelastic response of the solid Earth to surface loading changes due to glaciation and deglaciation, allow one to better understand the rheological characteristics of the Earth as well as the ice loading history [*Tamisiea et al.*, 2007].

GIA process affects sea-level change observations, tide gauges, satellite altimetry, and most crucially GRACE. To study the sea-level change, it is critical to understand the GIA contributions in these observations.

The main component of the GIA theory is to solve the sea-level equation. The basic form of the sea-level equation is developed by *Farrell and Clark* [1976]. Solution to the sea-level equation is related to the computation of the Earth's response to the loading. In the past more than 40 years, different groups have developed their GIA models by using different methods to solve the sea-level equation, e.g., normal mode and spectral method [*Peltier*, 1974; *Wu and Peltier*, 1982]; finite element/volume method [*Latychev et al.*, 2005; *Wu*, 2005; *Zhong et al.*, 2003]. To model GIA and accurately obtain predictions, two kinds of input are required. The first one is the Earth model that describes the Earth's structure and rheology parameters. This is used to compute the Earth's response to the surface loading. The second one is ice-loading history, which provides the ice thickness at a specific location for a specific time on Earth.

A benchmark study of the GIA computation codes or software systems is conducted by *Spada et al.* [2011], test computations show a satisfactory agreement between the results adopting different techniques by different GIA modelers participated in the study. However, recent study by *Guo et al.* [2012] shows that these models differ from each other substantially. *Huang et al.* [2013] used an ensemble of 14 GIA models to

investigate their differences when they are applied to correct different geodetic observations in order to estimate the sea-level change over Arctic Ocean.

To study the sea level change and its sources, it is necessary to have a better knowledge about GIA process and its effects. Also, to separate GIA signals from other signals remains research interest in the past decades. Studying the relationship between vertical displacement and gravity change induced by past/present surface loading change could be one potential solution to this separation problem [*De Linage et al.*, 2007; *Fang and Hager*, 2001; *James and Ivins*, 1998; *Purcell et al.*, 2011; *Velicogna and Wahr*, 2002; *Wahr et al.*, 1995].

1.3 Scientific Objectives

In this dissertation, we will focus on studying the GIA process and its effect on different geodetic measurements in determining the sea-level rise and to further investigate the present-day (2004–2012) mass component of the sea-level budget closure. The primary reason to work on the short data span is due to the limitation of GRACE data. Conventional approach is using GIA forward models to correct for GIA effects in sea level, and ice sheet mass balance measurements. Distinct theoretical treatments of the GIA process used to correct for geodetic measurements [*Tamisiea*, 2011] to measure sea level will be described and assessed. An ensemble of 15 different GIA models will be used as a means to assess the current uncertainty of these GIA models.

GIA is not separable from the gravity variation signal observed by GRACE if GRACE is the only data type used. In this study, we will develop the formulism and implement a methodology to jointly invert for the present-day mass change and GIA uplift over the ocean, using steric-corrected radar altimetry and GRACE data incorporating also elastic loading effects.

The scientific objectives of this dissertation include:

1. To quantify the GIA effect on different geodetic observations for global sea-level and ice sheet mass balance measurements, an ensemble of 15 predicted/estimated GIA models was used as a means to estimate the current uncertainty in the GIA models. We would like to address the current GIA forward model uncertainties in the direct measurements of sea-level using various geodetic measurements (tide gauges, altimetry, GRACE), and in the estimates of major geophysical sources contributing to present-day sea-level rise, including Antarctic and Greenland ice sheets.

2. To improve post-processed GRACE observed ice-sheet mass balance and ocean bottom pressure changes, and quantify the current uncertainties due to GIA forward modeling errors, geocenter motion and various other corrections. In particular, we will assess and quantify the dominant effort of the degree 2 zonal coefficient (J_2) or the Earth's oblateness change, on both ice-sheet mass balance and ocean mass variation estimates, in light of the fact that GRACE's J_2 is poorly constrained.

3. To implement an innovative method that to estimate and separate the GIA signal and the present-day ocean mass variations by combining data from GRACE and steric-corrected radar altimetry.To narrow the discrepancy in the present-day ocean mass component of the sea-level rise budget.

1.4 Dissertation Outline

Chapter 2 covers the GIA modeling, including the response of elastic and viscoelastic Earth to changes in surface load, and also the sea-level equation in elastic and viscoelastic situations.

Chapter 3 presents comparisons between contemporary GIA models and provides the uncertainty when using GIA model for different corrections to geodetic measurements.

Chapter 4 provides the geodetic measurements that are used in studying the sea-level rise, including tide gauge recorded relative sea level, radar altimetry measured geocentric sea level and GRACE measured ocean mass change.

Chapter 5 presents the interpretation of recent changes in the Earth's oblateness resulting from mass loss of the polar region ice-sheet and global glaciers in the context of elastic loading using sea-level fingerprint method.

Chapter 6 presents the result of sea-level budget closure problem with focus on ocean mass component and future improvement to close this budget. In addition, the separation of GIA and present-day mass change over ocean using an innovative approach is also implemented and discussed.

Chapter 2   Loading Theory and GIA Modeling

The problem of historical sea-level change due to ice sheets melt could be solved using sea-level equation based on Glacial Isostatic Adjustment (GIA) forward modeling. For the contribution of present day mass change, the pattern of sea-level change due to the redistribution of water that exchanged between land and ocean can be obtained using sea-level fingerprint method under elastic assumption.

To solve these problems, it is necessary to know the Earth's response to its surface load in viscoelastic/elastic situations. In this chapter, the relationships of deformation of the solid Earth and its gravitation potential perturbation due to surface mass load are presented in two types: Green's function approach and spherical harmonic approach.

Green's function is the response of the specific Earth model to a delta function type of force (instantaneous in time and point-like in space). After having derived the Green function, the response of the Earth to arbitrary loads or forces in space and time can be found by convolving these functions with loads of forces.

In the spherical harmonic approach, the surface density is first decomposed into a series of spherical harmonic functions, then the relationship between the surface mass load and the Earth's response is connected by load Love numbers. Normally the spherical harmonic expansion is truncated to a certain degree.

In general, Green's function approach is more accurate than the spherical harmonic approach due to the truncation in the latter.

In this chapter, the development of GIA modeling is also reviewed in general.

2.1   Elastic Deformation

On the surface of a spherical, self-gravitating, elastic Earth, given γ be a unit mass distributed uniformly across a disk with radius α. One could expand γ in a Legendre series [*Farrell*, 1972]:

$$\gamma = \sum_{n=0}^{\infty} \Gamma_n P_n \left(\cos\psi \right) \qquad\qquad \text{2-1}$$

where $P_n \left(\cos\psi \right)$ is the degree n Legendre polynomials, ψ is the angular distance from the center of load, and

$$\Gamma_n = \frac{\left[P_{n-1} \left(\cos\alpha \right) - P_{n+1} \left(\cos\alpha \right) \right]}{4\pi a^2 \left(1 - \cos\alpha \right)} \quad n > 0$$

$$\Gamma_0 = \frac{1}{4\pi a^2} \quad n = 0 \qquad\qquad \text{2-2}$$

where a is the mean radius of the Earth.

The Green's function of deformed gravitational potential is given as:

$$\phi^e(\psi) = \frac{ag}{M_e} \sum_{n=0}^{\infty} \left(1 + k_n'\right) P_n(\cos\psi)$$

2-3

The Green's function of surface vertical displacement is given as:

$$u^e(\psi) = \frac{a}{M_e} \sum_{n=0}^{\infty} h_n' P_n(\cos\psi)$$

2-4

The Green's function of horizontal displacement at the surface is given as:

$$v^e(\psi) = \frac{a}{M_e} \sum_{n=0}^{\infty} l_n' \frac{\partial P_n(\cos\psi)}{\partial\psi}$$

2-5

where M_e is the mass of the Earth, g is the gravitational acceleration at the Earth's surface.

Three dimensionless parameters k_n', h_n' and l_n' are degree n elastic load Love numbers, that are computed using an Earth model by solving a system of ordinary differential equations. In this dissertation, the elastic load Love numbers are computed using the Preliminary Reference Earth Model (PREM) [*Dziewonski and Anderson*, 1981] by [*Guo et al.*, 2004]. Figure 2.1 presents the load Love numbers up to degree 200. According to *Blewitt* [2003], degree 1 load Love numbers are not unique, the origin of the reference frame need to be specified before using these degree 1 load Love numbers.
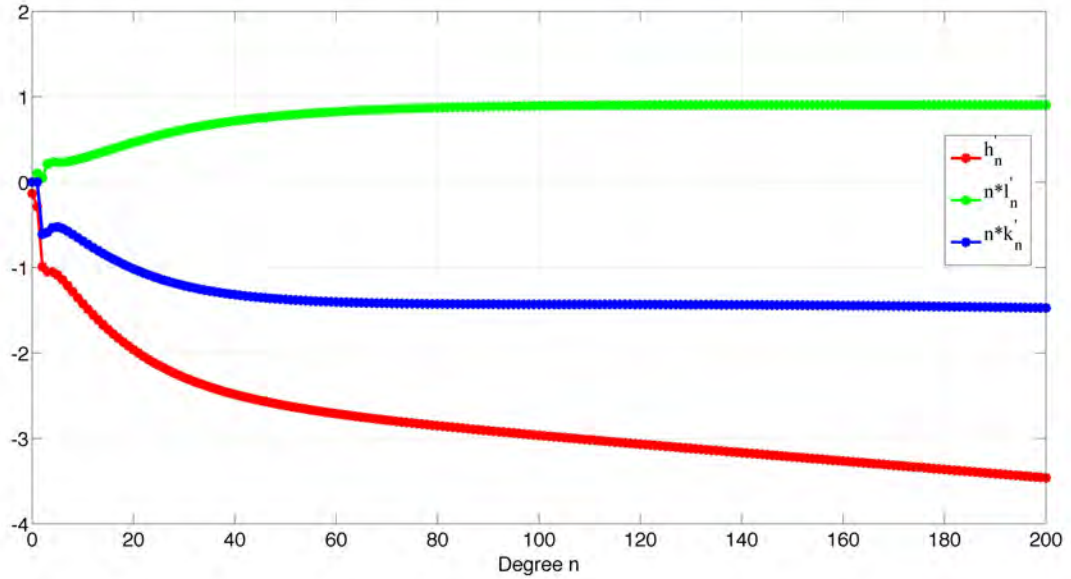

Figure 2.1 Dimensionless load Love numbers calculated using PREM Earth model from *Guo et al.* [2004].

After obtaining different Green's functions induced by point mass, the response of the Earth to surface load can be obtained by convolution between surface load and respect Green's function.

2.2   Viscoelastic Deformation

In the context of GIA forward modeling, the Earth is treated as a Maxwell solid , which has both viscous and elastic properties.

To model the viscoelastic response of the Earth to surface load, the formulation of *Peltier* [1974] is adopted. The viscoelastic response could be treated as the elastic response following by viscous response.

Similar to elastic case, the Green's functions are given as

$$\phi^L(\psi,t) = \frac{ag}{M_e} \sum_{n=0}^{\infty} \left(1 + k_n^L(t)\right) P_n(\cos\psi) \qquad \text{2-6}$$

$$u^L(\psi,t) = \frac{a}{M_e} \sum_{n=0}^{\infty} h_n^L(t) P_n(\cos\psi) \qquad \text{2-7}$$

$$v^L(\psi,t) = \frac{a}{M_e} \sum_{n=0}^{\infty} l_n^L(t) \frac{\partial P_n(\cos\psi)}{\partial \psi} \qquad \text{2-8}$$

On the basis of Maxwell model of the viscoelasticity, the time-dependent load Love numbers $k_n^L(t)$, $h_n^L(t)$ and $l_n^L(t)$ are written in the following according to *Peltier* [1976]

$$h_n^L(t) = h_n^E(t)\delta(t) + \sum_{k=1}^{K} r_k^n \exp\left(-s_k^n t\right) \qquad \text{2-9}$$

$$k_n^L(t) = k_n^E(t)\delta(t) + \sum_{k=1}^{K} q_k^n \exp\left(-s_k^n t\right) \qquad \text{2-10}$$

$$l_n^L(t) = l_n^E(t)\delta(t) + \sum_{k=1}^{K} t_k^n \exp\left(-s_k^n t\right) \qquad \text{2-11}$$

where k_n^E, h_n^E and l_n^E are degree n elastic load Love numbers, $\delta(t)$ is the Dirac delta function and the $\left(r_k^n, q_k^n, t_k^n, s_k^n\right)$ are amplitudes and inverse relaxation times of the set of K purely exponential decaying relaxation modes that is required to specify the time domain behavior of $k_n^L(t)$, $h_n^L(t)$ and $l_n^L(t)$.

Given a general surface load, the viscoelastic response of the Earth could be determined by calculating the space-time convolution of the general load function with the relevant Green's function.

2.3 Sea-Level Equation

In the viscoelastic situation, the vertical displacement of the solid surface is given by

$$R^L(\theta,\lambda,t) = \int_{-\infty}^{t} \iint_{\Omega} a^2 L(\theta',\lambda',t') u^L(\psi,t-t') d\Omega' dt' \qquad \text{2-12}$$

The perturbation to the geopotential on the un-deformed surface is given by

$$\Phi^L(\theta,\lambda,t) = \int_{-\infty}^{t} \iint_{\Omega} a^2 L(\theta',\lambda',t') \phi^L(\psi,t-t') d\Omega' dt' \qquad \text{2-13}$$

where (θ,λ) is the co-latitude and longitude of the observation point, (θ',λ') are the co-latitude and longitude of the load center, Ω indicates the entire surface of the Earth.

Using (2-12) and (2-13), we are going to introduce the sea-level equation that is used to address the Glacial Isostatic Adjustment problem.

The ocean height $S(\theta,\lambda,t)$ is the difference between ocean surface, which is assumed to be coincident with a geoid, and the solid surface, given as

$$S(\theta,\lambda,t) = O(\theta,\lambda)\left[G^L(\theta,\lambda,t) - R^L(\theta,\lambda,t)\right]$$ 2-14

where $O(\theta,\lambda)$ is 'ocean function' which is unity over ocean and zero over land [*Munk and MacDonald*, 1960]

$$G^L(\theta,\lambda,t) = \frac{1}{g}\Phi^L(\theta,\lambda,t) + G^L(t)$$ 2-15

$$G^L(t) = -\frac{M_I(t)}{\rho_W A_O} - \frac{1}{A_O}\left\langle G^L(\theta,\lambda,t) - R(\theta,\lambda,t)\right\rangle$$ 2-16

$G^L(t)$ is introduced to make sure the total mass of water is conserved. $M_I(t)$ is the total mass of the melt ice sheets, A_O is the area of ocean and $\langle * \rangle$ indicates the spatial integration over ocean.

By substituting (2-12), (2-13) and (2-15) into (2-14), we obtain

$$S(\theta,\lambda,t) = O(\theta,\lambda)\left[\begin{array}{c}\int_{-\infty}^{t}\iint_{\Omega}a^2 L(\theta',\lambda',t') \\ \left\{\frac{\phi^L(\psi,t-t')}{g} - u^L(\psi,t-t')\right\}d\Omega' dt' + G^L(t)\end{array}\right]$$ 2-17

This is the sea-level equation for a non-rotating Earth model that was first introduced by *Farrell and Clark* [1976].

The load function $L(\theta,\lambda,t)$ consists of both an ice component and an ocean component. It is conventionally written in the form

$$L(\theta,\lambda,t) = \rho_I I(\theta,\lambda,t) + \rho_W S(\theta,\lambda,t)$$ 2-18

where ρ_I and ρ_W are densities of ice and water respectively. $I(\theta,\lambda,t)$ is the space-time geometry of the ice sheets (from ice-loading history model). Note that sea-level change $S(\theta,\lambda,t)$ exists in both sides of the sea-level equation, thus iteration is needed when solving the sea-level equation.

Equation (2-17) is the basic type of sea-level equation. Since then, several important progresses have been made including consideration of shoreline migration, rotational feedback, the presence of grounded or floating ice, and 3-D Earth structure.

In the basic sea-level equation, the ocean geometry is defined using an ocean function, which is constant and equal to the present form. In reality, the shoreline will migrate according to sea-level rise or fall. To address this issue, a time-varying ocean geometry was performed [*Johnston*, 1993; *Kendall et al.*, 2005; *Lambeck and Nakada*, 1990; *Milne*, 1998; *Mitrovica and Milne*, 2003; *Peltier*, 1994]. Instead of $O(\theta,\lambda)$, $O(\theta,\lambda,t)$ is conventionally used to define the time-varying ocean function in the sea-level equation.

When surface mass load is redistributed in glaciation-deglaciation cycle, the Earth's rotational state is modified. A change in Earth's rotational state deforms both the geoid and solid surface, and hence affects the sea-level, thus further reconfiguring the Earth's surface mass load. This is so-called rotational feedback. It has been studied and included in the extended theory [*Han and Wahr*, 1989; *Kendall et al.*, 2005; *Milne and Mitrovica*, 1998; *Mitrovica and Wahr*, 2011; *Mitrovica et al.*, 2001; *Peltier*, 1998].

The modified sea-level equation concerning shoreline migration and rotational feedback is given as

$$S(\theta,\lambda,t)=O(\theta,\lambda)\left[\int_{-\infty}^{t}\iint_{\Omega}a^{2}\left\{L(\theta',\lambda',t')\left[\frac{\phi^{L}(\psi,t-t')}{g}-u^{L}(\psi,t-t')\right]+\Psi^{R}(\theta',\lambda',t')G^{T}(\psi,t-t')\right\}d\Omega'dt'+G^{L}(t)\right]$$
2-19

where $\Psi^{R}(\theta',\lambda',t')$ is the rotational potential and $G^{T}(\psi,t-t')$ is the tidal Green's function, given as

$$G^{T}(\psi,t-t')=\frac{\phi(\psi,t-t')}{g}-u^{T}(\psi,t-t')$$
2-20

Which can be written as

$$G^{T}(\psi,t)=\frac{1}{g}\sum_{n=1}^{\infty}\left(\delta(t)+k_{n}^{T}(t)-h_{n}^{T}(t)\right)P_{n}(\cos\psi)$$
2-21

where $k_{n}^{T}(t)$ and $h_{n}^{T}(t)$ are time-dependent viscoelastic tidal Love number.

Besides considering shoreline migration and rotational feedback, further refinement of sea-level equation are made to consider the presence of grounded or floating ice [*Milne and Mitrovica*, 1998; *Mitrovica and Milne*, 2003], 3-D Earth structure [*Kaufmann et al.*, 2000; *Nakada and Lambeck*, 1991; *Paulson et al.*, 2005; *Wu and van der Wal*, 2003; *Zhong et al.*, 2003]

2.4 Sea-Level Equation Input and Output

Two inputs are required to solve the Sea-level equation, they are (1) Earth structure and rheology, and (2) Ice-loading history. The Earth structure and its rheological characters are used to compute the Earth's response to the applied surface load (Love numbers and Green's function). The ice-loading history provides the spatial-temporal distribution of the surface mass load.

The Earth models used in GIA modeling are customarily assumed to be spherically symmetrical. These models include an elastic lithosphere of consistent thickness, several layers viscoelastic mantle, the outer liquid core, and inner rigid core. The mantle is usually divided into two layers: upper mantle and lower mantle. The viscosity in each layer is assumed to be uniform. The transition at the core-mantle boundary from solid to liquid indicates that the core plays no part in influencing GIA processes. The Earth's radial elastic and density structure is commonly adopted from the Preliminary Reference

13

Earth Model (PREM) [*Dziewonski and Anderson*, 1981]. The viscosity is either obtained from geophysical inversion, or estimated from independent geophysical studies.

The spherical models are 1-D, which means they only vary along the radial direction. Recently, 3-D Earth structure are adopted in the GIA modeling, which means, the thickness of the lithosphere is allowed to change laterally, and also the viscosity of each layer is allowed to change laterally [*Wang and Wu*, 2006].

Ice loading history consists of ice thickness at each location and also its evolution along with discrete time steps. Most commonly used global modal are ICE-series [*Peltier*, 2002; 2004; *Tushingham and Peltier*, 1991]. Another global model is the RSES model developed by Kurt Lambeck (Research School of Earth Sciences, Canberra, Australia), which has not been published yet as a single data set. It is formed from several individual ice model from different regions, e.g., Fennoscandian part is from FBK8 [*Lambeck et al.*, 1998], Laurentide and Greenland from ICE-1 [*Peltier and Andrews*, 1976], and Antarctica ANT3 model [*Nakada and Lambeck*, 1988].

Besides global ice models, regional models are also available for several regions.

For Antarctica the most commonly used one is developed by Ivins and James [*Ivins and James*, 2005] which have been updated and will be published in 2013. Another one is W12A that is developed by Whitehouse and her colleagues [*Whitehouse et al.*, 2012] and now it is being used in recent Antarctica ice mass balance study [*King et al.*, 2012; *Shepherd et al.*, 2012]. For Greenland, the most commonly used are the Simpson model [*Simpson et al.*, 2009] and the ANU model [*Fleming and Lambeck*, 2004].

The accuracy of a GIA model is strongly dependent upon the accuracy of the input ice model. Difference between different GIA models will be compared and discussed in the next chapter.

The method to solve the sea-level equation includes, but not restricted to: (1) Spectral method based on normal mode theory [*Clark et al.*, 1978; *Peltier*, 1974]; (2) Pseudo-spectral method based on normal mode theory [*Mitrovica and Peltier*, 1991]; (3) Finite element method [*Martinec*, 2000; *Paulson et al.*, 2005; *Wu and van der Wal*, 2003].

The outputs from sea-level equation are the relative sea-level change, the surface displacement and the geopotential change induced by GIA.

2.5 Elastic Loading Relations in Spectral Domain

The gravitational potential of the Earth is given as

$$V(\theta,\lambda,r) = \frac{GM_E}{r} \sum_{n=0}^{\infty} \left(\frac{a}{r}\right)^n \sum_{m=0}^{n} \left\{ \bar{C}_{nm} \cos m\lambda + \bar{S}_{nm} \sin m\lambda \right\} \bar{P}_{nm}(\cos\theta) \qquad \text{2-22}$$

where a is the radius of the Earth, G is the gravitational constant, M_E is the mass of the Earth, r is the geocentric distance, (θ,λ) denotes the co-latitude and longitude respectively, n and m are the degree and order. $\bar{C}_{nm}$ and $\bar{S}_{nm}$ are the (fully-normalized) spherical harmonic coefficients (SHCs). $\bar{P}_{nm}$ is the normalized associated Legendre function.

The degree 0 term is proportional to the total mass of the Earth, and the degree 1 terms are proportional to the position of the Earth's center of mass relative to the chosen coordinate origin. There is no total mass change in the Earth's system, thus degree 0 term does not change with time. In GRACE, the coordinate origin always coincides with the Earth's instantaneous center of mass. Thus, degree 1 terms also disappeared.

It is common to describe the Earth's gravity filed in terms of the shape of geoid.

$$N(\theta,\lambda) = a\sum_{n=0}^{\infty}\sum_{m=0}^{n}\left\{\bar{C}_{nm}\cos m\lambda + \bar{S}_{nm}\sin m\lambda\right\}\bar{P}_{nm}(\cos\theta) \qquad \text{2-23}$$

The time-dependent change of this geoid is:

$$\Delta N(\theta,\lambda) = a\sum_{n=0}^{\infty}\sum_{m=0}^{n}\left\{\Delta\bar{C}_{nm}\cos m\lambda + \Delta\bar{S}_{nm}\sin m\lambda\right\}\bar{P}_{nm}(\cos\theta) \qquad \text{2-24}$$

Spherical harmonic expansion of changes in surface mass density is shown as:

$$\Delta\sigma(\theta,\lambda) = a\rho_W\sum_{n=0}^{\infty}\sum_{m=0}^{n}\left\{\Delta\hat{C}_{nm}\cos m\lambda + \Delta\hat{S}_{nm}\sin m\lambda\right\}\bar{P}_{nm}(\cos\theta) \qquad \text{2-25}$$

where $\Delta\hat{C}_{nm}$ and $\Delta\hat{S}_{nm}$ are the spherical harmonics of surface density, ρ_W is the density of water. Assumption is made that the density changes happen on (or near) the surface of the Earth, in a short time scale, it could be treated as the elastic loading problem.

Spherical harmonic expansion of changes in vertical displacement is shows as:

$$\Delta u_r(\theta,\lambda) = a\sum_{n=0}^{\infty}\sum_{m=0}^{n}\left\{\Delta A_{nm}\cos m\lambda + \Delta B_{nm}\sin m\lambda\right\}\bar{P}_{nm}(\cos\theta) \qquad \text{2-26}$$

From changes of geopotential spherical harmonic coefficients to changes of gravity disturbance spherical harmonic coefficients (denoted by ΔC_{nm}^g and ΔS_{nm}^g for the sake of convenient), the relationship is given as follows.

From SHCs to changes in gravity disturbance:

$$\left\{\begin{matrix}\Delta C_{nm}^g \\ \Delta S_{nm}^g\end{matrix}\right\} = \frac{GM_E}{a^2}(n+1)\left\{\begin{matrix}\Delta\bar{C}_{nm} \\ \Delta\bar{S}_{nm}\end{matrix}\right\} \qquad \text{2-27}$$

In the context of elastic loading problem, the relations from SHCs to changes in surface mass density (i.e., defined as mass/area) is given as [*Wahr et al.*, 1998]

$$\left\{\begin{matrix}\Delta\hat{C}_{nm} \\ \Delta\hat{S}_{nm}\end{matrix}\right\} = \frac{\rho_E}{3\rho_W}\frac{2n+1}{1+k_n'}\left\{\begin{matrix}\Delta\bar{C}_{nm} \\ \Delta\bar{S}_{nm}\end{matrix}\right\} \qquad \text{2-28}$$

where k_n' is the load Love number, ρ_E is the average density of the Earth.

Conversely, from the changes in surface mass density to SHCs:

$$\left\{\begin{matrix}\Delta\bar{C}_{nm} \\ \Delta\bar{S}_{nm}\end{matrix}\right\} = \frac{3\rho_W}{\rho_E}\frac{1+k_n'}{2n+1}\left\{\begin{matrix}\Delta\hat{C}_{nm} \\ \Delta\hat{S}_{nm}\end{matrix}\right\} \qquad \text{2-29}$$

From changes in surface mass density to changes in gravity disturbance:

15

$$\left\{ \begin{array}{c} \Delta C_{nm}^{g} \\ \Delta S_{nm}^{g} \end{array} \right\} = \frac{GM_E}{a^2} \frac{3\rho_W}{\rho_E} \frac{(n+1)(1+k_n^{'})}{2n+1} \left\{ \begin{array}{c} \Delta \hat{C}_{nm} \\ \Delta \hat{S}_{nm} \end{array} \right\} \qquad \text{2-30}$$

Conversely, from changes in gravity disturbance to changes in surface mass density:

$$\left\{ \begin{array}{c} \Delta \hat{C}_{nm} \\ \Delta \hat{S}_{nm} \end{array} \right\} = \frac{a^2}{GM_E} \frac{\rho_E}{3\rho_W} \frac{2n+1}{(n+1)(1+k_n^{'})} \left\{ \begin{array}{c} \Delta C_{nm}^{g} \\ \Delta S_{nm}^{g} \end{array} \right\} \qquad \text{2-31}$$

From changes in surface mass density to changes in vertical displacement:

$$\left\{ \begin{array}{c} \Delta A_{nm} \\ \Delta B_{nm} \end{array} \right\} = \frac{3\rho_W}{\rho_E} \frac{h_n^{'}}{2n+1} \left\{ \begin{array}{c} \Delta \hat{C}_{nm} \\ \Delta \hat{S}_{nm} \end{array} \right\} \qquad \text{2-32}$$

2.6 Sea-Level Fingerprint

Present-day ice melting from the polar region (e.g., Antarctica and Greenland) or mountain glaciers will generate a unique pattern of sea-level change depending upon the location of melting. The resulting distribution of sea-level change will be due to a change in the volume of water in the ocean, and changes to the shape of the gravitational potential as a result of mass redistribution. This is known as the sea-level fingerprint.

The fingerprint represents the forward modeling of relative sea-level change due to the gravitational effect of surface mass redistribution, and it could be addressed by solving the elastic sea-level equation. In this study, sea-level fingerprint for each region is obtained by solving the elastic sea-level equation with consideration the rotational feedback effect.

After obtaining the unique sea-level patterns from different sources of melting, we also obtain the mass redistribution. Thus, it is possible to study the contribution of mass changes in the polar region to changes in Earth's oblateness and also the sea-level change, which will be discussed in Chapter 5.

2.7 Chapter Summary

In this chapter, both the elastic and viscoelastic response of the Earth to the surface load are formulated, and GIA forward modeling is described after introducing the sea-level equation. The spectral relations between surface mass changes and other quantities, such as vertical displacement and geoid change, are provided in the context of elastic loading.

Chapter 3   Comparison of GIA Models

This Chapter presents the contemporary regional and global GIA models that are available to us. Comparison is made between those GIA models. In the end, GIA corrections for different geodetic measurements are also discussed and compared in detail.

The model comparison is conducted in the following ways: (1) Spatial (global and regional) comparison, (2) Spectral comparison. In addition, two inherent relations described by *Wahr et al.* [1995] are used here to provide an alternative method to quantify the differences between GIA models.

3.1   Contemporary GIA Models

The GIA models used in this study are (1) Global models, which are listed in Table 3.1. (2) Regional models for Antarctic, IJ05 [*Ivins and James*, 2005] and W12A [*Whitehouse et al.*, 2012].

Descriptions of global models are summarized in Table 3.1, in where references for more information are also provided. We adopt the "short name" convention as in *Guo et al.* [2012]. The convention is as follows, the first 3 letters denote the author(s), the following number/letter denotes the ice history used in the model (e.g., 5 means ICE-5G), the next 3 letters (if any) indicate Earth model/rheology or other information, and the last 'R' (if included) is used to indicate that rotational feedback is considered in the model. For 'O' in Pel_5_VM2_R_O and Pel_5_VM4_R_O, it indicates that these two models are older than the lately updated model Pel_5_VM2_R obtained from Peltier's website (http://www.atmosp.physics.utoronto.ca/~peltier/data.php). Most of the models are from two sources, the first one is the website of the Special Bureau for Loading (SBL) of the Global Geophysical Fluid Center (GGFC) of the International Earth Rotation and Reference System Service (IERS)[1] the second one is from the author(s) via private communication.

Most commonly used models in GRACE community are Pau-5-R and Pel-5-VM2-R. About Pau-5-R model, we have only the gravitational potential data, so in this study, this model is only used to correct GRACE observations, it is not used to correct tide gauge and satellite altimetry observations. Centrifugal potential effect is removed from Pel_5_VM2_R_O and Pel_5_VM4_R_O in order to correct GRACE observation. The WaO_EGOD model is the estimation from geodetic observation data (EGOD) [*Wu et al.*, 2010], and no ice history or Earth parameter information is used during the computation.

3.2   Comparison between GIA Models

---

[1] Currently, the SBL website is down and will be back with all the data later. At present, all data from this website can be downloaded from ftp://dutlru2.lr.tudelft.nl/pub/wouter/pgs.tar.gz

Comparison between different GIA models is made in spatial and spectral domain.

3.2.1 Comparison in the Spatial Domain (global)

The direct way is to compare the GIA prediction/estimation in the spatial domain.

Figure 3.1 presents the different GIA predicted/estimated uplift rate. The similar patterns over North America, Scandinavia, Antarctica and Greenland could be seen in most of the models. The differences between models mainly come from different ice history models used in the GIA modeling. For example, since there are no data in ICE-1G ice model over Antarctica, therefore, GIA predicted uplift rate is almost zero in SaS-1 over Antarctica, thus it is not suitable for studying Antarctica. For WaO_EGOD model over Greenland, it is different from the other GIA models, mainly because this model is estimated using a combination of geodetic measurements and ocean model, thus, it is not a GIA prediction from GIA forward modeling. This estimation over Greenland could potentially help the GIA modeler to adjust/validate their ice history model over Greenland.

Figure 3.2 shows the different GIA predicted/estimated relative sea level (RSL) rate. Similar to uplift rate comparison, the differences mainly come from the different ice loading history used in the GIA forward modeling. This quantity could be used to totally remove the GIA effect from tide gauge recorded relative sea level.

Table 3.1 A brief description of the 14 GIA models used in this study as modified from *Guo et al.* [2012]. Abbreviations: ATU—author(s); IH—ice history; UMV—upper mantle viscosity in 10^{21} Pa s; LMV—lower mantle viscosity in 10^{21} Pa s; LT—lithosphere thickness in km; NLE—number of layers of Earth model; PREM—preliminary reference earth model; LH—lateral heterogeneity; RF—rotational feedback; CT—Computation technique; RF—reference, NM—Normal mode, NI—Numerical integration, SEM—Spectral element method, SA—Semi-analytic, FEM—Finite element.

Model	AUT	IH	UMV	LMV	LT	NLE	LH	RF	CT	SR	REF
Pau_5_R[1]	Paulson	ICE-5G	0.9	3.6	98	5	No	Yes	NM	PC	[Paulson et al., 2007]
Pel_4_VM2	Peltier	ICE-4G[2],[3]	0.4-1.5	1.3-3.9	90	PREM	No	No	NM (NI)	PC	[Peltier, 2002]
Pel_5_VM2_R	Peltier	ICE-5G	0.4-1.5	1.3-3.9	90	PREM	No	Yes	NM (NI)	Website[9]	[Peltier, 2004]
Pel_5_VM2_R_O	Peltier	ICE-5G	0.4-1.5	1.3-3.9	90	PREM	No	Yes	NM (NI)	SBL[10]	[Peltier, 2004]
Pel_5_VM4_R_O	Peltier	ICE-5G	0.4-1.5	1.3-3.9	90	PREM	No	Yes	NM (NI)	SBL	[Peltier, 2004]
SKM_O_R	Sasgen, Klemann and Martinec	Own	0.52	5.9	120	4	No	Yes	SEM	PC	[Sasgen et al., 2012]
SaS_1	Spada and Stocchi	ICE-1G[4]	1	2	100	4	No	No	NM (SA)	SBL	SBL
SaS_3	Spada and Stocchi	ICE-3G	1	2	100	4	No	No	NM (SA)	SBL	SBL
SVv_3_REF	Schotman, Vermeersen and van Hove	ICE-3G[5]	0.5	5	115	5	No	No	NM (SA)	SBL	SBL
SVv_L_ALT	Schotman, Vermeersen and van Hove	Lambeck[6]	1	1	98	5	No	No	NM (SA)	SBL	SBL
vdW_5	van der Wal	ICE-5G[7]	0.9	3.6	98	6	No	No	NM (SA)	PC	[van der Wal et al., 2011]
vdW_5_R	van der Wal	ICE-5G[7]	0.9	3.6	98	6	No	Yes	NM (SA)	PC	[van der Wal et al., 2011]
WaW_4	Wang and Wu	ICE-4G	0.6	3-6	115	5	Yes	No	FEM	PC	[Wang and Wu, 2006]
WaW_5	Wang and Wu	ICE-5G[7]	0.6	3-6	115	5	Yes	No	FEM	PC	[Wang and Wu, 2006]
WaO_EGOD	Wu and others	This model is estimated from geodetic Observations[8]								PC	[Wu et al., 2010]

19

Figure 3.3 presents the different GIA predicted/estimated geoid rate. Most of the differences come from different ice loading history. Besides this, the rotational feedback effect causes another major differences in the predicted geoid rate, and this rotational feedback also brings potential larger uncertainties.

Figure 3.4, Figure 3.5 and Figure 3.6 present the absolute sea-level rate, GRACE-type mass rate and gravity anomaly rate derived from GIA predicted/estimated relative sea-level, geoid rate respectively.

3.2.2 Comparison in the Spatial Domain (regional)

For regional comparison, two regions that attract the most attention are presented: (1) Antarctica and (2) Greenland.

Figure 3.7 summarized the selected GIA prediction/estimation over Antarctica. The first row is the uplift rate plots, and the second row is the geoid rate plots. Differences in uplift rate include the location and amplitude of the uplift dome. Differences in geoid rate are also significant in both location and amplitude. This will cause significant uncertainties when they are used in ice mass balance study. Later we will compare them when they are used to correct GRACE result.

Figure 3.8 summarized the selected GIA prediction/estimation over Greenland. The most obvious one is WaO_EGOD model that has significant negative values in the center areas of Greenland. SKM-O-R model is different with others in the southwest and northeast part. This may due to the ice loading history they have used in their modeling.
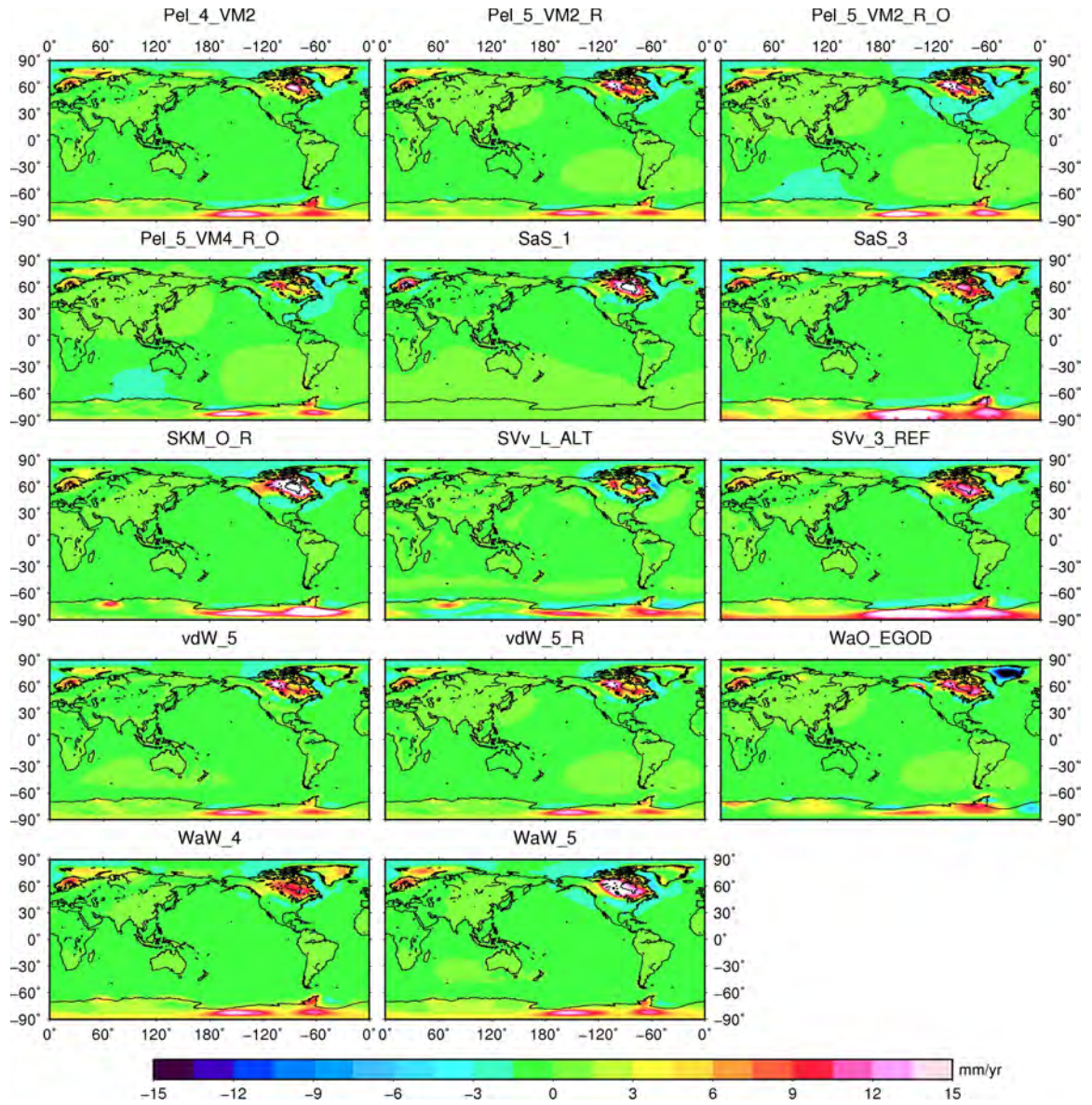
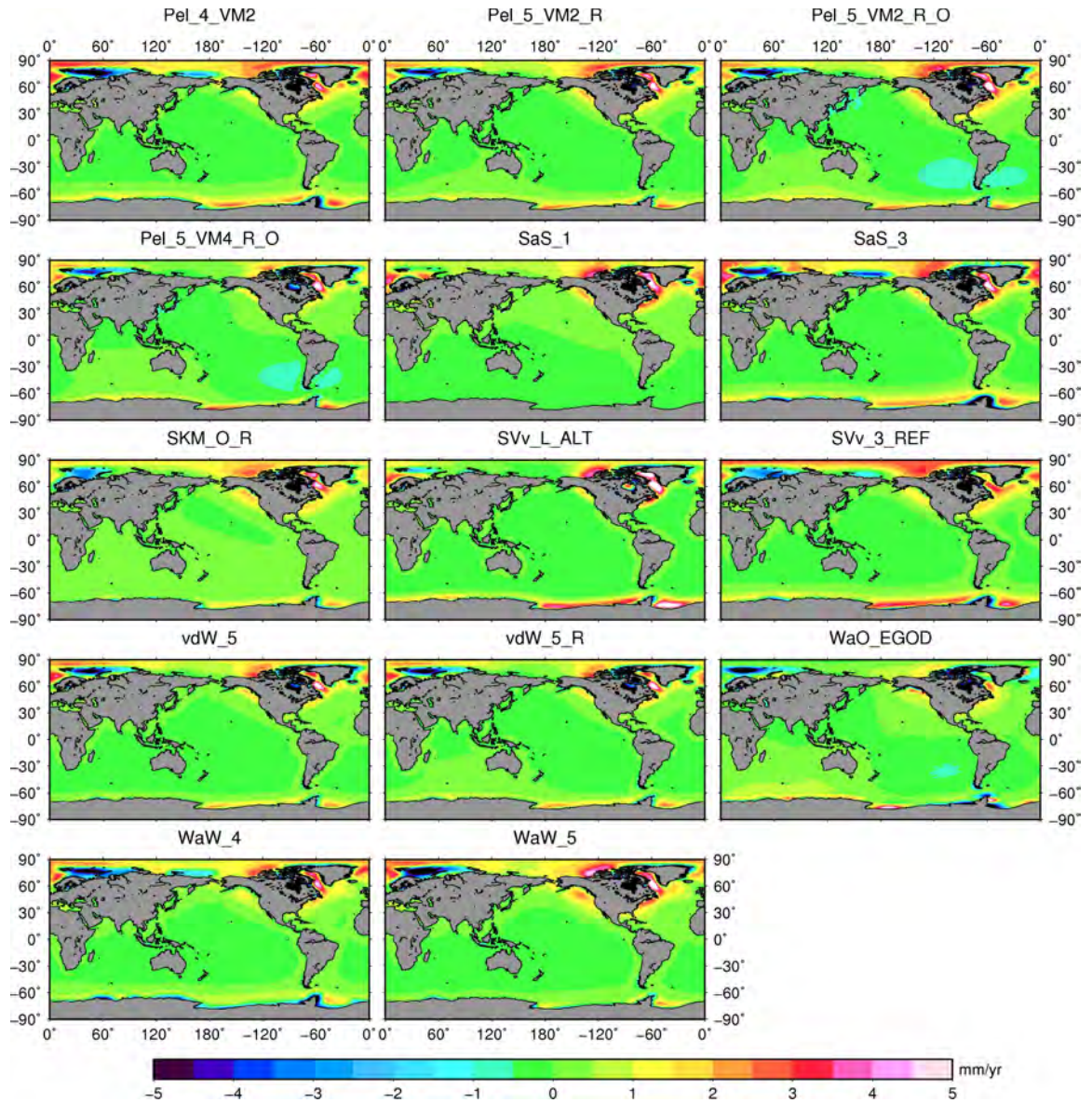Figure 3.1 GIA model predicted/estimated uplift rate.

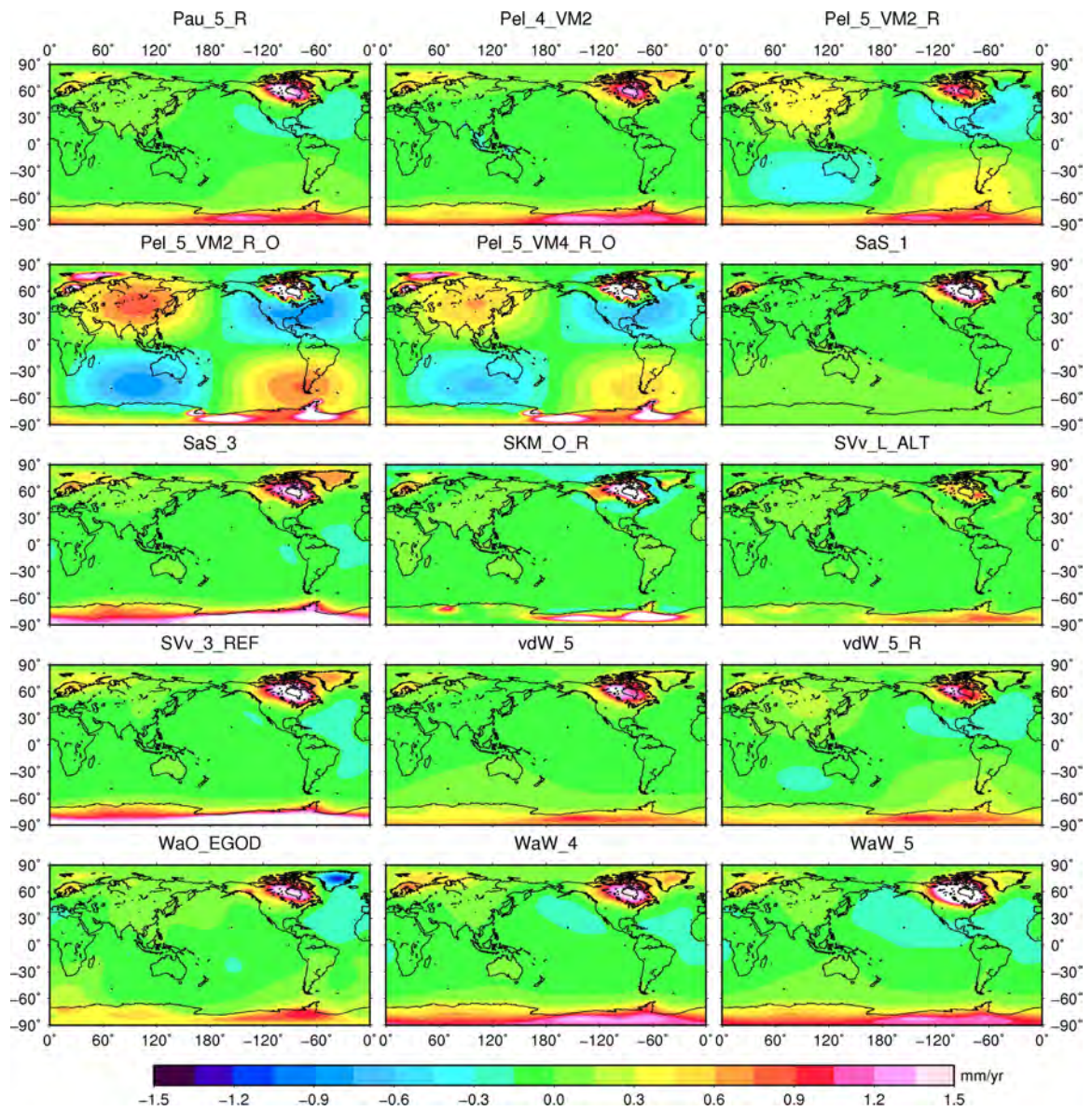Figure 3.2 GIA model predicted/estimated relative sea-level (RSL) rate.

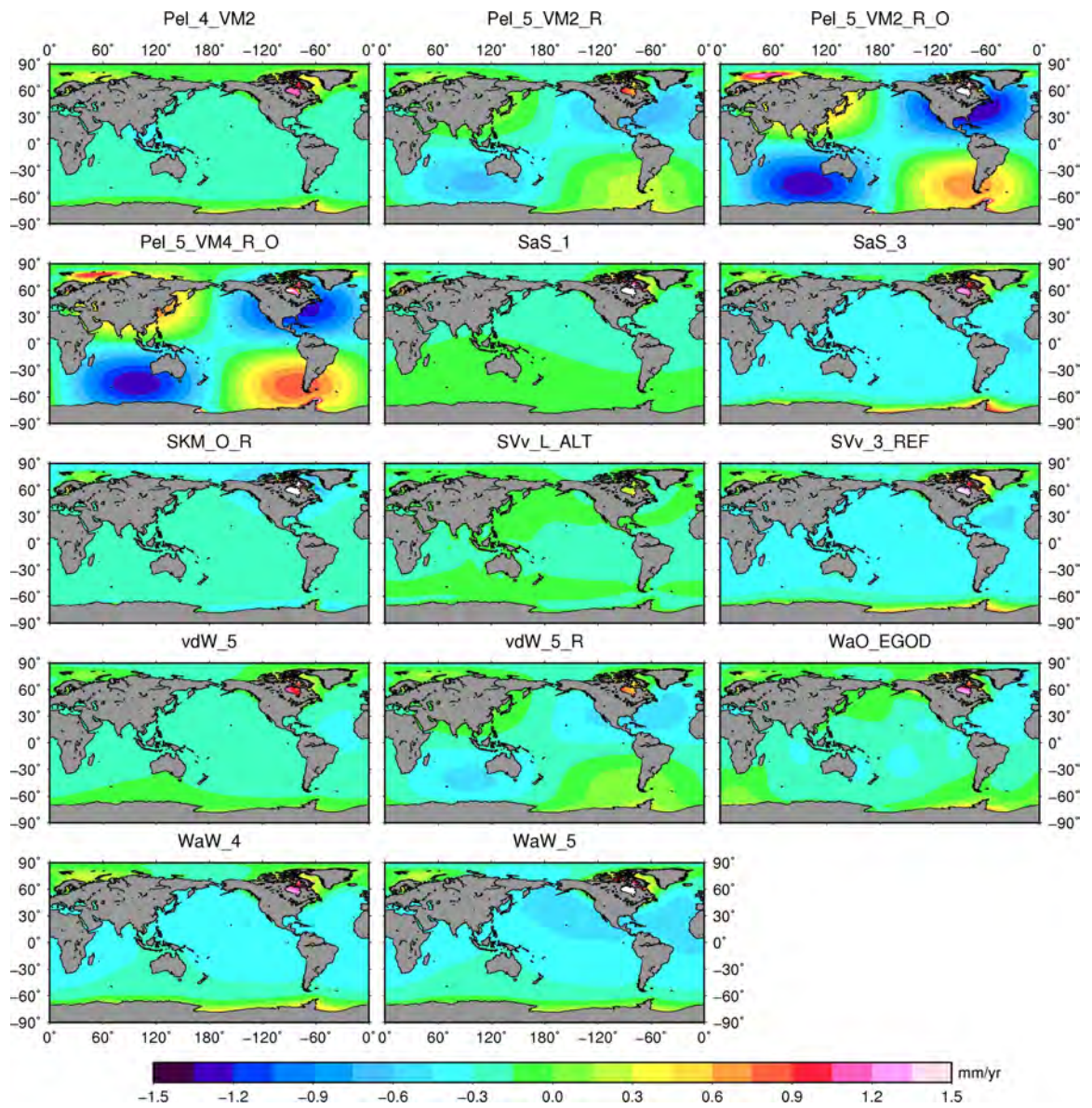Figure 3.3 GIA model predicted/estimated geoid rate

Figure 3.4 Absolute sea-level (ASL) rate computed from predicted/estimated GIA model.

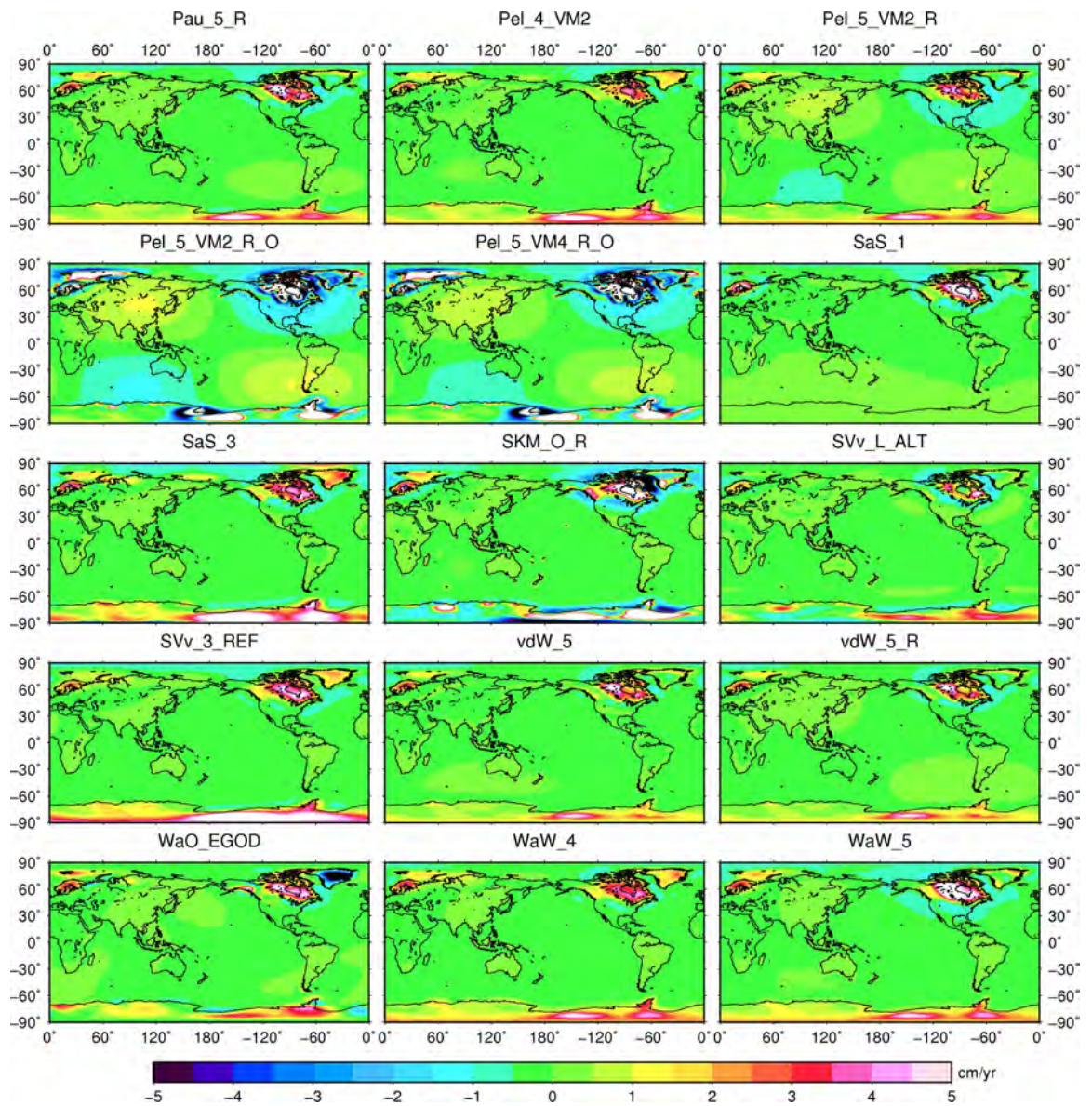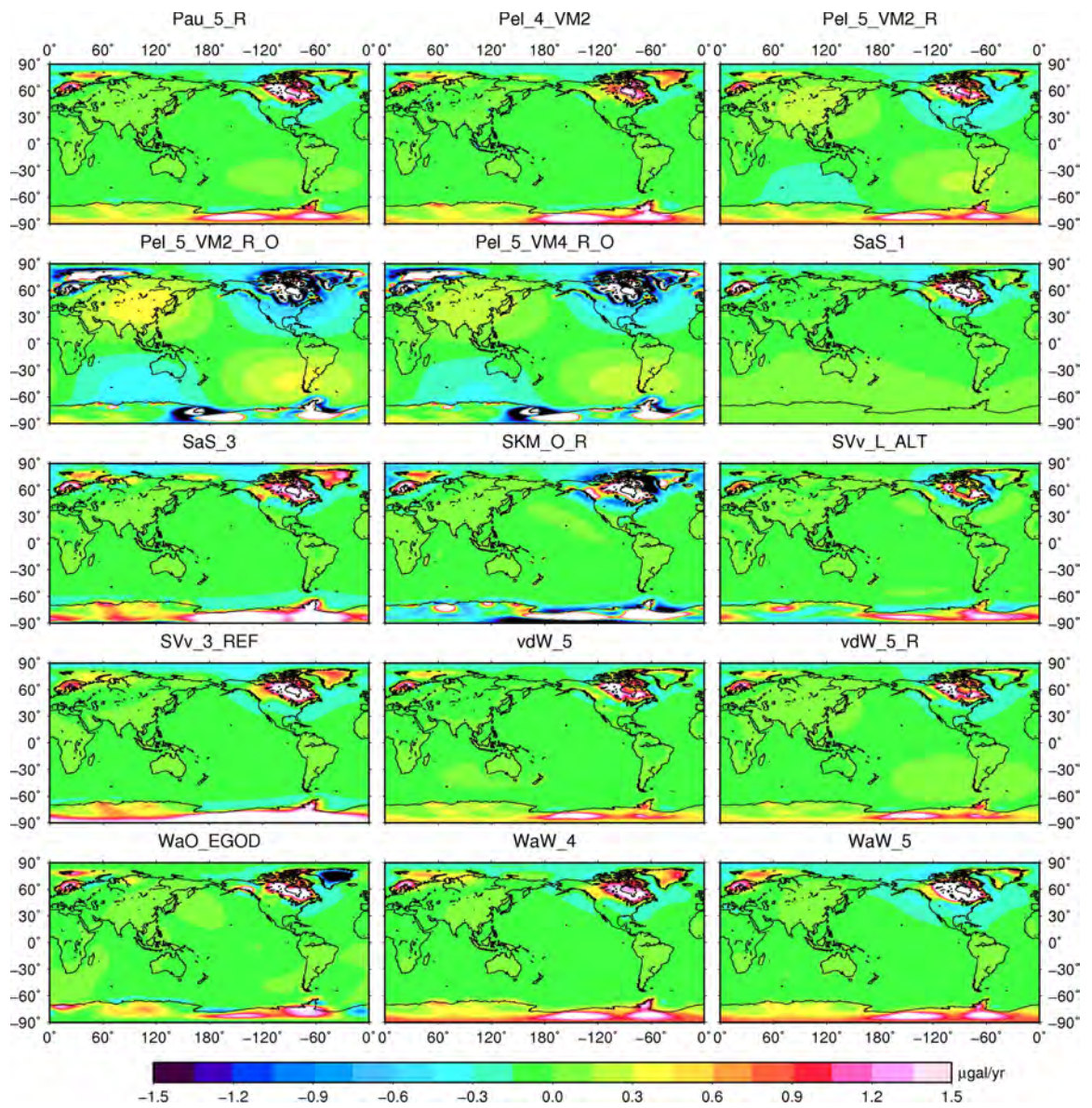Figure 3.5 GRACE-type mass change rate computed from predicted/estimated GIA geoid rate.

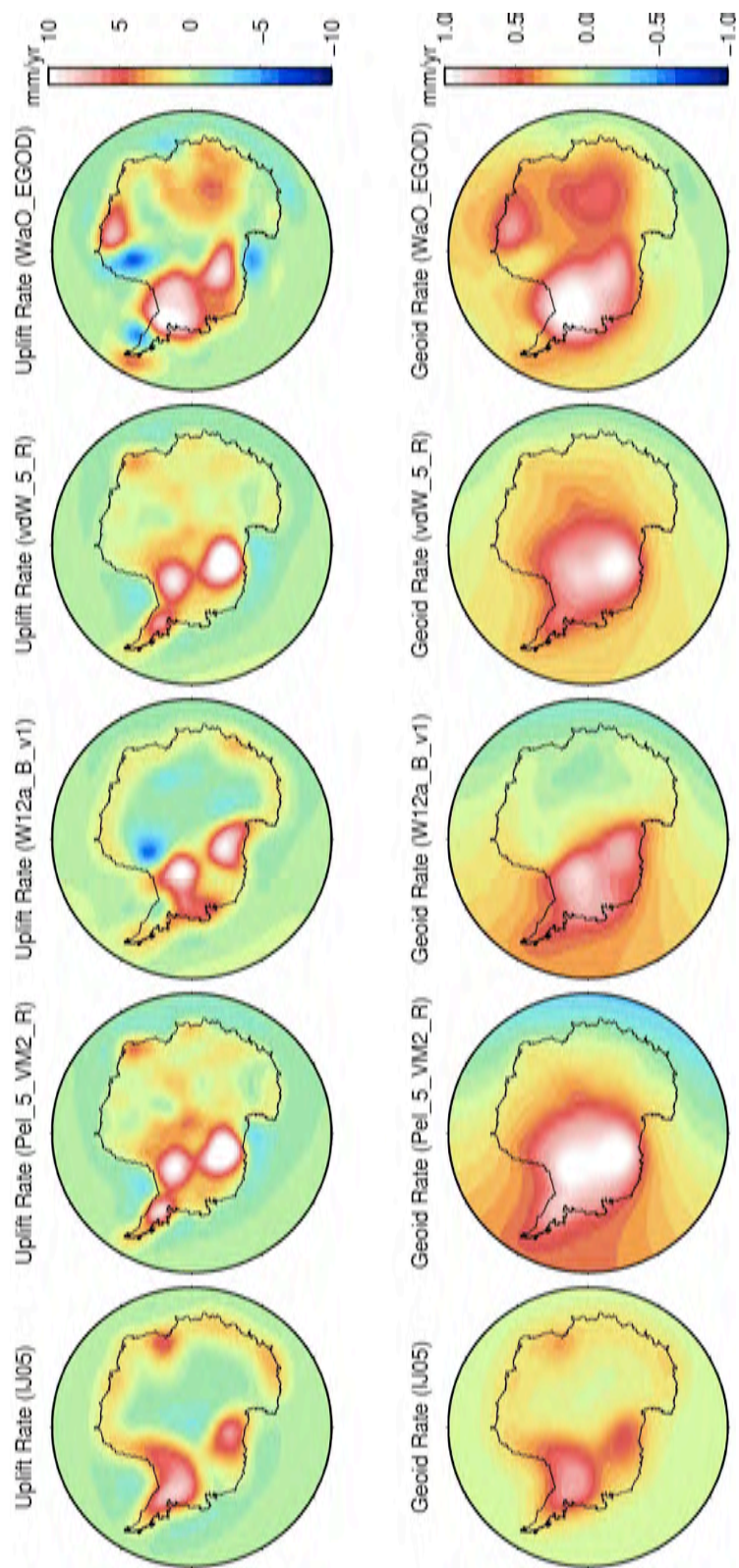Figure 3.6 GIA gravity anomaly rate computed from predicted/estimated GIA geoid rate.

Figure 3.7 GIA model prediction/estimation over Antarctica. Top: uplift rate. Bottom: geoid rate. Unit is mm/yr.
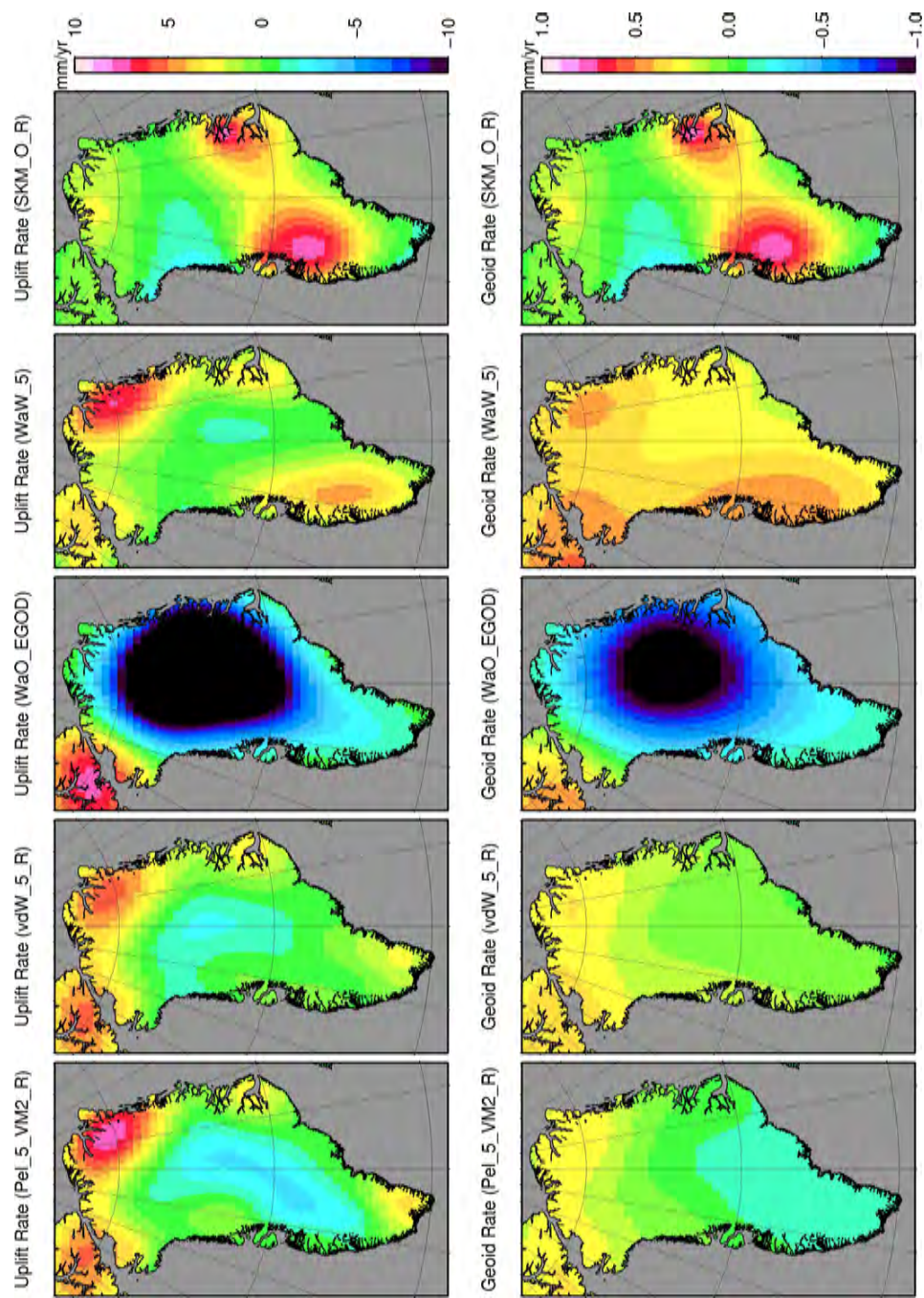
Figure 3.8 GIA model prediction/estimation over Greenland. Top: uplift rate. Bottom: geoid rate. Unit is mm/yr.

3.2.3　Comparison in the Spectral Domain

To compare those models in the spectral domain, we use the quantity, σ_n^2, called the "degree variance" and is defined as

$$\sigma_n^2 = \sum_{m=0}^{n} \left(C_{nm}^2 + S_{nm}^2 \right) \qquad\qquad 3\text{-}1$$

where n is the degree and m is the order of the spherical harmonic coefficients C_{nm} and S_{nm}.

All the global models are decomposed using spherical harmonic expansion up to degree 60. The reason to do this is that it is the same with the maximum degree of GRACE Level-2 product. In the next, we will compute the GRACE-type mass rate from these GIA models. The plots are shown for the spherical harmonic coefficients from degree 2 to degree 60. Figure 3.9 summarizes the 'degree variances' for GIA uplift rate, RSL rate and geoid rate respectively.

For the geoid rate spectrum, most GIA models show the similar pattern except for Pel_5_VM2_R_O, Pel_5_VM4_R_O, and SKM_O_R for degree larger than 8. Svv_L_ALT shows a different pattern in the lower degree. For degree 2, the differences between different models are significant, this will cause significant difference when using for calculating the GRACE-type mass change correction.

For the uplift rate spectrum, most GIA models show the similar pattern except for SVv_3_REF (degree larger than 30) and SVv_L_ALT (degree lower than 10).

For the relative sea-level rate spectrum, it is similar to uplift rate spectrum, most GIA models show the similar pattern except for SVv_3_REF (degree larger than 30) and SVv_L_ALT (degree lower than 10).
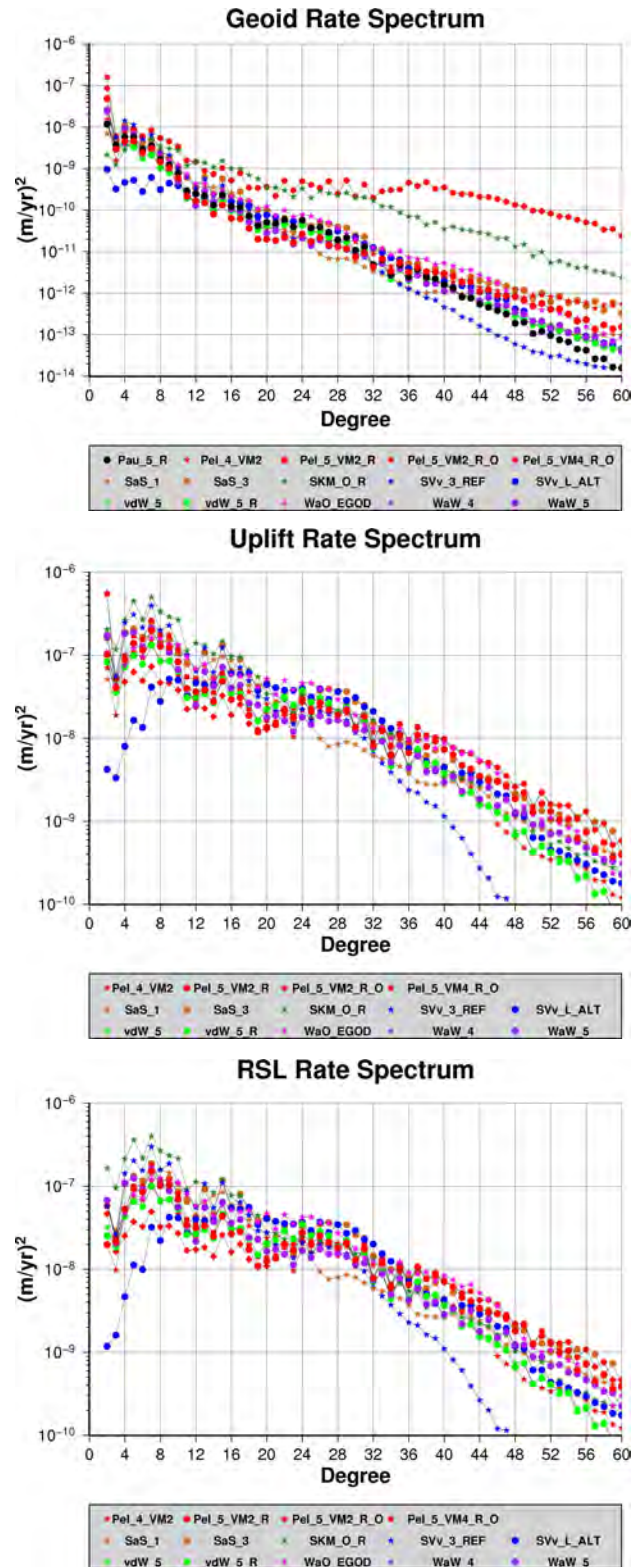
Figure 3.9 Spectrum of GIA model predicted/estimated quantities: geoid rate (Top), uplift rate (Middle) and relative sea-level (Bottom).

30

3.3   Two Inherent Relations

This work is an extension of *Guo et al.* [2012].

Besides spatial comparison and spectral comparison, another comparison is also made by using two approximate inherent relations that was found by *Wahr et al.* [1995]. These relations are for the viscous contribution only, i.e., the effect of GIA induced passive relative sea-level changes and its elastic loading effect are not included. The viscous effect of uplift and geoid rates can be wrote in the form of spherical harmonic series:

$$\dot{U} = a \sum_{n=2}^{N_{max}} \sum_{m=0}^{n} \left[\dot{\bar{A}}_{nm} \cos m\lambda + \dot{\bar{B}}_{nm} \sin m\lambda \right] \bar{P}_{nm}(\cos\theta) \qquad 3\text{-}2$$

$$\dot{N} = a \sum_{n=2}^{N_{max}} \sum_{m=0}^{n} \left[\dot{\bar{C}}_{nm} \cos m\lambda + \dot{\bar{S}}_{nm} \sin m\lambda \right] \bar{P}_{nm}(\cos\theta) \qquad 3\text{-}3$$

where the 'dot' denotes the time differentiation.

The viscous effect of gravity change rate as observed by GRACE (In here, only the mass contribution is considered, and the uplift related free air correction as for instruments on land is not included) is then given as

$$\dot{g} = \frac{GM_E}{a^2} \sum_{n=2}^{N_{max}} \sum_{m=0}^{n} (n+1) \left[\dot{\bar{C}}_{nm} \cos m\lambda + \dot{\bar{S}}_{nm} \sin m\lambda \right] \bar{P}_{nm}(\cos\theta) \qquad 3\text{-}4$$

According to *Wahr et al.* [1995], they found that, for a large range of Earth parameters that should comprise those of the real Earth, the following relation between uplift and geoid rates holds:

$$\left\{ \begin{array}{c} \dot{\bar{A}}_{nm} \\ \dot{\bar{B}}_{nm} \end{array} \right\} \approx \frac{2n+1}{2} \left\{ \begin{array}{c} \dot{\bar{C}}_{nm} \\ \dot{\bar{S}}_{nm} \end{array} \right\} \qquad 3\text{-}5$$

Based on this relation, they further found an uplift-gravity relation:

$$\dot{U} \approx A\dot{g}, \quad A=6.5 \, \text{mm}/\mu\text{gals} \qquad 3\text{-}6$$

In this study, we will 'simulate' uplift rates using geoid rate and gravity rate, respectively:

$$\dot{U}_N = a \sum_{n=2}^{N_{max}} \sum_{m=0}^{n} \frac{2n+1}{2} \left[\dot{\bar{C}}_{nm} \cos m\lambda + \dot{\bar{S}}_{nm} \sin m\lambda \right] \bar{P}_{nm}(\cos\theta) \qquad 3\text{-}7$$

$$U_g = A \frac{GM_E}{a^2} \sum_{n=2}^{N_{max}} \sum_{m=0}^{n} (n+1) \left[\dot{\bar{C}}_{nm} \cos m\lambda + \dot{\bar{S}}_{nm} \sin m\lambda \right] \bar{P}_{nm}(\cos\theta) \qquad 3\text{-}8$$

According to (3-5), (3-7) and (3-8), we use the following quantities to determine the misfit of the GIA models to the relations of *Wahr et al.* [1995] (hereafter we use 'Wahr's rule' to represent these relations)

$$\left\{ \begin{array}{c} \delta\dot{\bar{A}}_{nm} \\ \delta\dot{\bar{B}}_{nm} \end{array} \right\} = \left\{ \begin{array}{c} \dot{\bar{A}}_{nm} \\ \dot{\bar{B}}_{nm} \end{array} \right\} - \frac{2n+1}{2} \left\{ \begin{array}{c} \dot{\bar{C}}_{nm} \\ \dot{\bar{S}}_{nm} \end{array} \right\} \qquad 3\text{-}9$$

$$\delta \dot{U}_N = \dot{U} - \dot{U}_N$$
$$\delta \dot{U}_g = \dot{U} - \dot{U}_g$$
<div align="right">3-10</div>

The first one is in the spectral domain while the last two are in the spatial domain.

To evaluate these models against Wahr's rule, discrepancy D_{RMS} is defined as a relative error between the uplift rate from GIA model and the prediction/estimation from geoid rate and gravity change rate respectively. This discrepancy is thus defined as:

$$D_{RMS}(k) = \frac{\dot{U}_{PDT}^{RMS}(k)}{\dot{U}_{Model}^{RMS}(k)} \times 100\%$$
<div align="right">3-11</div>

where $\dot{U}_{PDT}^{RMS}(k)$ is the root mean square (RMS) of predicted (PDT) uplift rate from geoid rate and gravity rate for k^{th} model, respectively, and $\dot{U}_{Model}^{RMS}(k)$ is the RMS of uplift rate from k^{th} GIA model.

Larger value of D_{RMS} indicates larger difference between model uplift rate and predicted uplift rate.
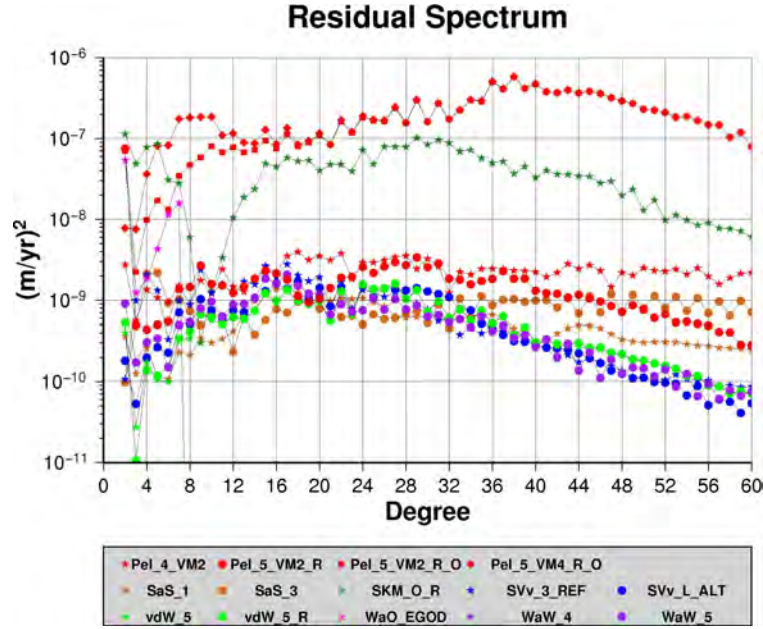

Figure 3.10 Comparison of uplift rate residual after applying the uplift-geoid approximation.

Figure 3.10 shows the misfit in the spectral domain. Figure 3.11 and Figure 3.12 show the residuals in uplift rate after applying two approximations in the spatial domain.

Table 3.2, Table 3.3 and Table 3.4 summarized the statistical information over global, ocean and land respectively.

From the comparison, we see that three models do not fit these two approximations, Pel_5_VM2_R_O, Pel_5_VM4_R_O, and SKM_O_R. For Pel_5_VM2_R_O and Pel_5_VM4_R_O, the reason maybe due to one error that was found in 2012 according to Peltier's website, and after correction the updated Pel_5_VM2_R fit the approximation

better than before. The reason why SKM_O_R does not fit these two approximations is unknown (One likely explanation is due to their different formulations in rotational feedback).
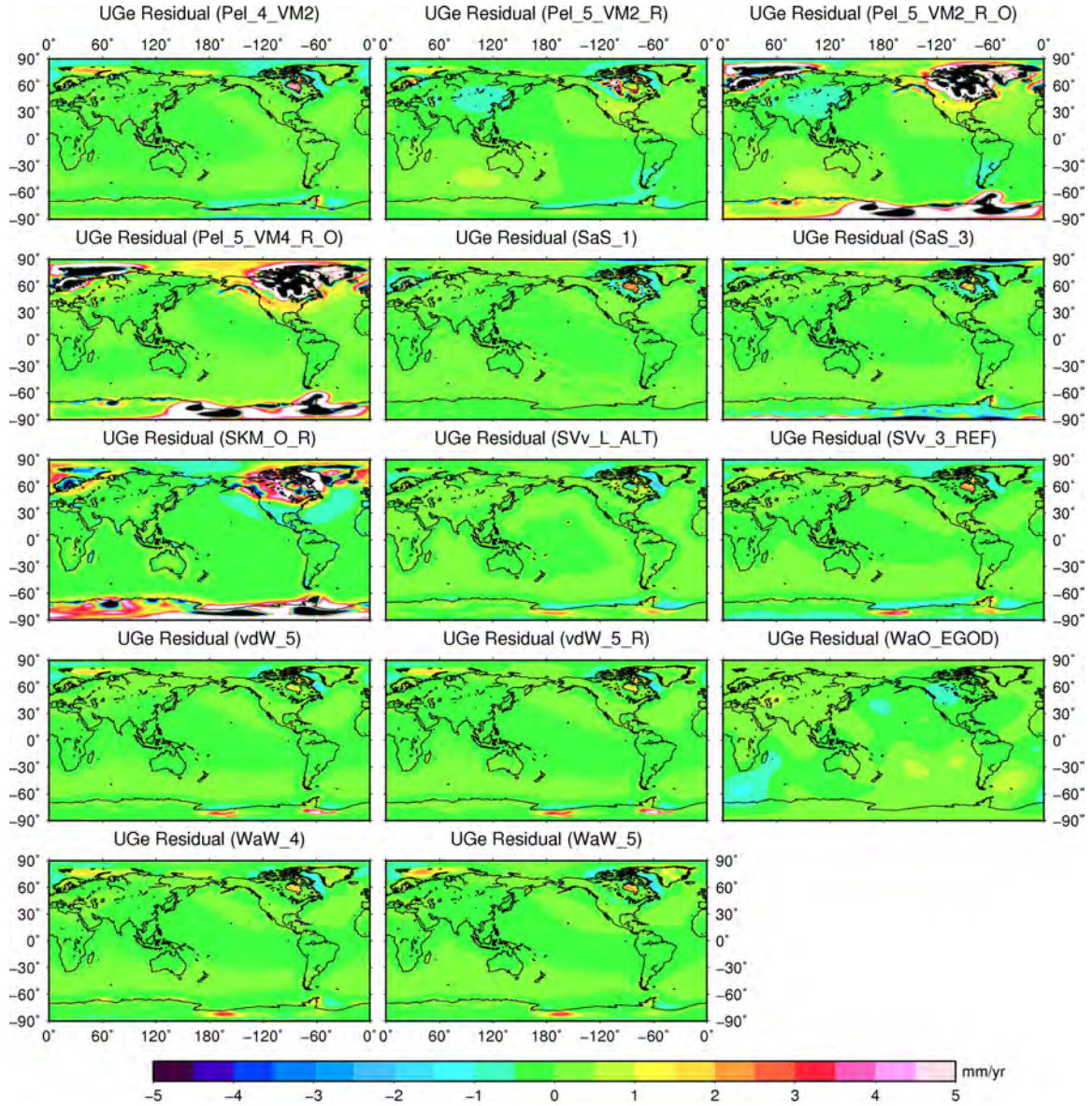

Figure 3.11 Residual rate in uplift from uplift-geoid approximation. Unit is mm/yr.
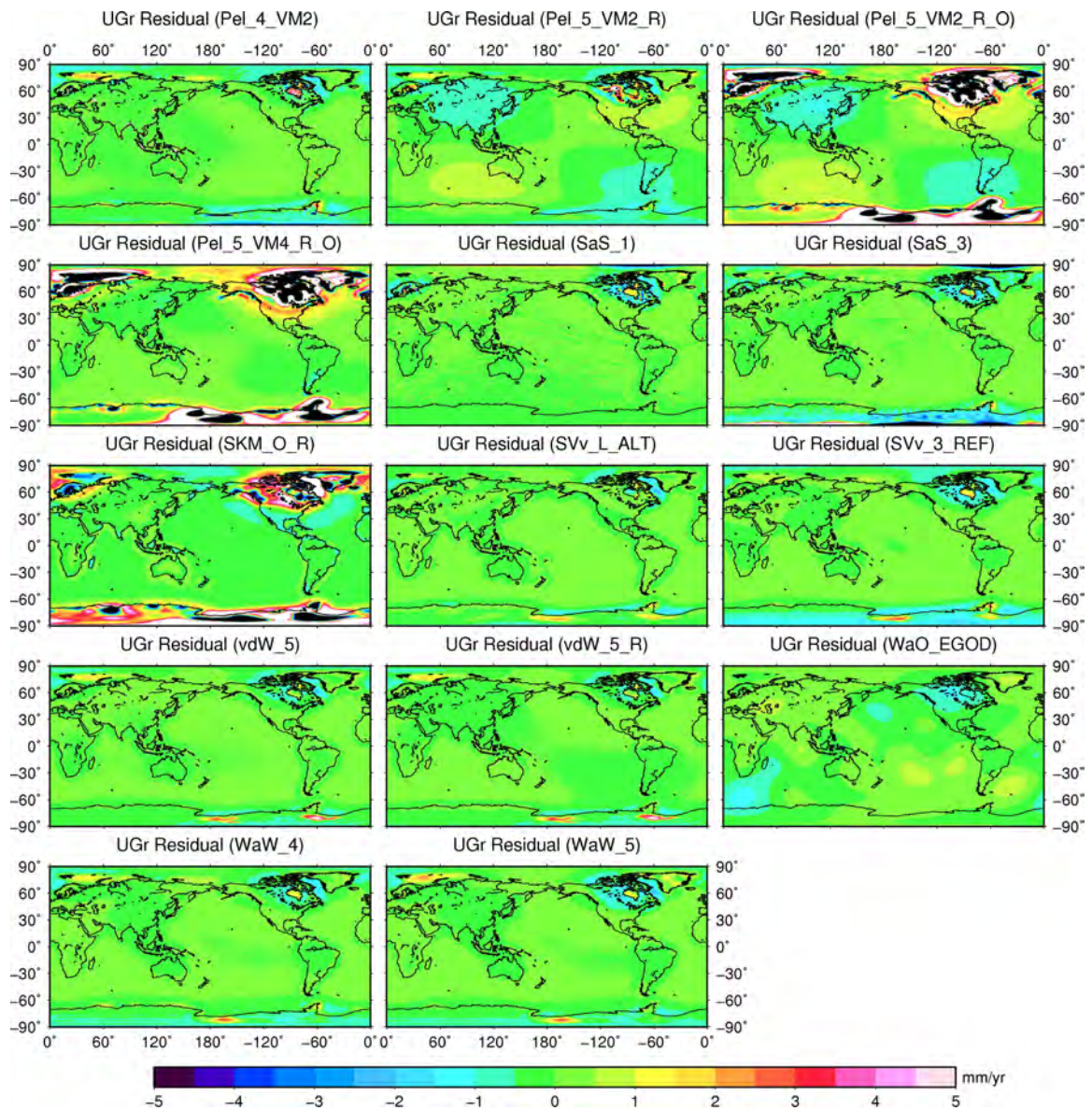
Figure 3.12 Residual rate in uplift from uplift-gravity approximation. Unit is mm/yr.

Table 3.2 Statistics against Wahr's rule (Global).

Model	$\dot{U}^{RMS}$ (mm/yr)	$\dot{U}_N^{RMS}$ (mm/yr)	$\dfrac{\dot{U}_N^{RMS}}{\dot{U}^{RMS}}$	$\dot{U}_g^{RMS}$ (mm/yr)	$\dfrac{\dot{U}_g^{RMS}}{\dot{U}^{RMS}}$
Pel_4_VM2	0.29	0.20	69.3%	0.21	70.6%
Pel_5_VM2_R	0.34	0.13	36.4%	0.15	44.7%
Pel_5_VM2_R_O	0.45	0.87	191.2%	0.90	197.8%
Pel_5_VM4_R_O	0.36	0.90	249.6%	0.93	256.6%
SaS_1	0.40	0.07	17.6%	0.07	18.4%
SaS_3	0.38	0.06	16.7%	0.08	19.7%
SKM_O_R	0.53	0.37	70.2%	0.37	70.8%
SVv_3_REF	0.40	0.05	13.1%	0.06	15.6%
SVv_L_ALT	0.27	0.04	16.7%	0.04	15.2%
vdW_5	0.31	0.04	13.6%	0.05	15.3%
vdW_5_R	0.31	0.04	13.2%	0.04	13.7%
WaO_EGOD	0.38	0.10	27.0%	0.11	29.5%
WaW_4	0.35	0.04	12.5%	0.05	13.8%
WaW_5	0.51	0.05	9.8%	0.06	12.1%

Table 3.3 Statistics against Wahr's rule (Over Ocean)

Model	$\dot{U}^{RMS}$ (mm/yr)	$\dot{U}_N^{RMS}$ (mm/yr)	$\dfrac{\dot{U}_N^{RMS}}{\dot{U}^{RMS}}$	$\dot{U}_g^{RMS}$ (mm/yr)	$\dfrac{\dot{U}_g^{RMS}}{\dot{U}^{RMS}}$
Pel_4_VM2	0.26	0.14	56.5%	0.15	57.0%
Pel_5_VM2_R	0.25	0.11	42.3%	0.14	56.4%
Pel_5_VM2_R_O	0.39	0.69	175.6%	0.72	184.1%
Pel_5_VM4_R_O	0.34	0.74	219.7%	0.77	227.1%
SaS_1	0.34	0.06	16.9%	0.05	15.4%
SaS_3	0.29	0.06	19.7%	0.06	20.6%
SKM_O_R	0.39	0.29	74.0%	0.29	74.9%
SVv_3_REF	0.28	0.06	20.0%	0.06	20.9%
SVv_L_ALT	0.18	0.05	26.4%	0.05	25.2%
vdW_5	0.20	0.04	21.1%	0.05	23.3%
vdW_5_R	0.21	0.04	19.6%	0.04	19.1%
WaO_EGOD	0.24	0.11	45.1%	0.12	47.8%
WaW_4	0.25	0.05	18.1%	0.05	18.3%
WaW_5	0.31	0.05	16.3%	0.05	16.7%

Table 3.4 Statistics against Wahr's rule (Over and)

Model	$\dot{U}^{RMS}$ (mm/yr)	$\dot{U}_N^{RMS}$ (mm/yr)	$\dfrac{\dot{U}_N^{RMS}}{\dot{U}^{RMS}}$	$\dot{U}_g^{RMS}$ (mm/yr)	$\dfrac{\dot{U}_g^{RMS}}{\dot{U}^{RMS}}$
Pel_4_VM2	0.36	0.28	80.2%	0.29	82.1%
Pel_5_VM2_R	0.48	0.16	32.8%	0.17	36.8%
Pel_5_VM2_R_O	0.55	1.14	205.1%	1.16	210.2%
Pel_5_VM4_R_O	0.40	1.15	285.2%	1.18	292.0%
SaS_1	0.50	0.09	18.1%	0.10	20.6%
SaS_3	0.52	0.08	14.6%	0.10	19.1%
SKM_O_R	0.72	0.49	67.9%	0.50	68.4%
SVv_3_REF	0.56	0.04	7.6%	0.07	12.1%
SVv_L_ALT	0.39	0.04	9.9%	0.03	7.5%
vdW_5	0.45	0.04	9.6%	0.05	11.0%
vdW_5_R	0.45	0.04	9.2%	0.05	10.6%
WaO_EGOD	0.55	0.08	15.3%	0.10	18.2%
WaW_4	0.49	0.04	8.1%	0.05	10.7%
WaW_5	0.76	0.05	6.5%	0.08	10.2%

3.4   GIA Corrections to Geodetic Observations

To compare different GIA corrections, we need to describe the GIA corrections to different geodetic observations first.

3.4.1   GIA Effect on Tide Gauge Measurement

What the tide gauge records is the local sea level change that is relative to the benchmark attached to the Earth's crust. The tide gauge observation is the change of distance between sea surface and the surface of solid Earth. The ongoing GIA process causes the glaciated region to rebound and the surrounding region to subside. Tide gauges near the glaciated region, i.e., the forebulge region at the LGM, will record a relative sea level (RSL) decrease, while the tide gauges surrounding glaciated region will capture an increasing RSL in their record. It is known that a region far away from glaciated region could also be affected [*Peltier*, 1998; *Peltier and Tushingham*, 1991].

The mass redistribution of mantle material causes the crustal uplift underneath the tide gauge that is recorded by the tide gauge. This mass redistribution also perturbs the equipotential surface that is at the sea surface. Therefore, in order to remove the GIA contribution from tide gauge records, both sea surface change and solid Earth surface change are needed. The GIA model predicted rate of relative sea level accounts both effects and is used to remove GIA contribution from tide gauge records. Some recent studies used GPS measurement at or near tide gauge benchmarks to obtain vertical land motion and used it to correct the tide gauge record to compare with altimetry results. However, this only removes part of the GIA effect [*Tamisiea*, 2011; *Tamisiea and Mitrovica*, 2011].

It is worthy to mention that tide gauge records also include the elastic contribution from present-day loading change, such as ice sheet or glacier melt, atmosphere, tidal, ocean or hydrologic loading. To study the sea-level change caused by present-day climate change, these effects must be removed from the tide gauge RSL record.

3.4.2 GIA Effect on Satellite Altimetry Measurement

Satellite altimetry measures the absolute sea level relative to a common datum. The most commonly used datum at present is the International Terrestrial Reference Frame (ITRF). In the ongoing GIA process, the mantle material redistribution changes the sea floor and also the equipotential surface on which the absolute sea level lies. In GIA modelling, an assumption is made that there is no current water exchange between land and ocean, so the averaged GIA predicted absolute sea level change over the ocean is actually the averaged changes of the sea floor.

The average of absolute sea surface from GIA model prediction over a specific region gives a correction to altimetry measured sea level trend. *Peltier* [2001] computed a global average of his GIA model prediction over 66°N to 66°S (the coverage limit of TOPEX/Poseidon satellite altimetry), and obtained an average value of –0.30 mm/yr, which is suggested to be used for the GIA correction to globally averaged altimetry measured sea-level rise.

3.4.3 GIA Effect on GRACE Measurement

GRACE measures the gravity change due to mass redistribution within the Earth system. Normally it is interpreted as the surface mass loading in terms of equivalent water thickness change on an elastic Earth [*Wahr et al.*, 1998]. GIA process is largely the redistribution of mantle mass, the density of mantle material is much higher than the density of water. If one interprets the GRACE measurement without removing the GIA effect, it would lead to significant different or even erroneous estimates. To obtain the sea-level change due to ocean mass change, the GIA effect should be removed before interpretation, the straightforward way is using GIA models. Two approaches are normally used: (1) To remove the GIA effect in the GRACE-derived spherical harmonic coefficients before converting them to equivalent water thickness; (2) To compute equivalent water thickness from GIA geopotential changes directly and remove it from the observations. In this chapter, we adopt the latter way in order to investigate how large is the uncertainty due to GIA models.

In contrast to the contribution to altimetry measurements, GIA contribution in GRACE observation is different in two aspects. The first aspect is a spatial constant value due to the different definition between GIA predicted absolute sea level and geoid. This constant is shown as the spherical harmonic degree zero in the decomposed GIA predicted absolute sea-level change. While in GRACE, the changing rate of degree zero Stokes coefficient is zero to indicate that the total mass of the Earth system is conserved. The second aspect is that the GRACE measurement is acquired in inertial reference frame, but the GIA model prediction is used for observation obtained in Earth-fixed rotating frame. The additional centrifugal potential, which results from the change in polar motion due to mass redistribution in GIA process, could affect the sea level or sea surface that is observed by altimeter, but GRACE does not sense the influence from this change of centrifugal potential. Therefore, for the GIA models with rotational feedback, if they are used to correct GRACE observation, this centrifugal potential must be removed before calculation.

In addition, it worth to mention that in both Altimetry and GRACE data processing, the effect of pole tide (including both solid Earth and ocean pole tides) computed using observed polar motion based on elastic Earth model was removed. Thus, when computing GIA correction for both Altimetry and GRACE from the GIA models with rotational feedback, the contribution from GIA caused polar drift to pole tide assuming elastic response of the solid Earth should be excluded [*Guo et al.*, 2012].

3.5   Comparison between GIA Corrections

3.5.1   Tide Gauge

For tide gauge measured relative sea level, the GIA predicted/estimated relative sea level is used for GIA correction.

It is shown in Figure 3.2 that the GIA correction for tide gauges is plotted geographically. It is obvious that the tide gauges near glaciated region (e.g., Scandinavia and North America) are most affected by this GIA process and it is vital to remove GIA effect before interpreting the tide gauge measurement in the context of climate change.

Table 3.5 summarizes statistical information about the GIA correction when the contemporary GIA models are used to correct the selected tide gauges. Information about the selected tide gauge will be presented in the next chapter. From Table. 3.5 we know that if averaged globally, GIA effect on tide gauge obtained sea-level change is around – 0.30 mm/yr. This value will surely change with the different tide gauge selection.

Table 3.5 Statistics of GIA correction for global tide gauges.

Model	1948_2011			1992_2011		
	RSL (mm/yr)	GIA (mm/yr)	After correction (mm/yr)	RSL (mm/yr)	GIA (mm/yr)	After correction (mm/yr)
Pel_4_VM2	1.75	–0.18	1.93	1.90	–0.19	2.09
Pel_5_VM2_R	1.75	–0.28	2.03	1.90	–0.28	2.18
Pel_5_VM2_R_O	1.75	–0.28	2.03	1.90	–0.29	2.19
Pel_5_VM4_R_O	1.75	–0.28	2.03	1.90	–0.29	2.19
SaS_1	1.75	–0.39	2.14	1.90	–0.41	2.31
SaS_3	1.75	–0.26	2.01	1.90	–0.27	2.17
SKM_O_R	1.75	–0.45	2.20	1.90	–0.46	2.36
SVv_3_REF	1.75	–0.28	2.03	1.90	–0.29	2.19
SVv_L_ALT	1.75	–0.15	1.90	1.90	–0.15	2.05
vdW_5	1.75	–0.24	1.99	1.90	–0.24	2.14
vdW_5_R	1.75	–0.29	2.04	1.90	–0.30	2.19
WaO_EGOD	1.75	–0.49	2.24	1.90	–0.50	2.39
WaW_4	1.75	–0.32	2.06	1.90	–0.33	2.23
WaW_5	1.75	–0.24	1.99	1.90	–0.25	2.15
Mean and STD	**1.75±0.46**	**-0.29±0.09**	**2.04±0.47**	**1.90±0.87**	**-0.30±0.09**	**2.20±0.88**

3.5.2   Radar Altimetry

Figure 3.4 is the GIA correction for radar altimetry measurement and Table 3.6 summarizes statistical information about this correction over ocean (Global ocean, ocean

between latitude 66°N and 66°S, selected region for sea-level budget study in Chapter. 6).
From Table 3.6 we know that GIA effect for radar altimetry result is around −0.30 mm/yr.

Table 3.6 Statistics of GIA correction for altimetry over ocean.

Model	Ocean between latitude 90°N to 90°S GIA correction (mm/yr)	Ocean between latitude 66°N to 66°S GIA correction (mm/yr)	Selected Sea-Level Budget Study Region GIA correction (mm/yr)
Pel_4_VM2	−0.21	−0.23	−0.24
Pel_5_VM2_R	−0.26	−0.27	−0.29
Pel_5_VM2_R_O	−0.35	−0.37	−0.39
Pel_5_VM4_R_O	−0.28	−0.30	−0.32
SaS_1	−0.13	−0.14	−0.15
SaS_3	−0.34	−0.36	−0.38
SKM_O_R	−0.24	−0.24	−0.25
SVv_3_REF	−0.34	−0.36	−0.38
SVv_L_ALT	−0.15	−0.15	−0.15
vdW_5	−0.22	−0.23	−0.24
vdW_5_R	−0.24	−0.25	−0.27
WaO_EGOD	−0.21	−0.22	−0.24
WaW_4	−0.30	−0.32	−0.34
WaW_5	−0.34	−0.36	−0.38
Mean and STD	**−0.26±0.07**	**−0.27±0.08**	**−0.29±0.08**

3.5.3 GRACE

Comparison about GRACE-type mass rate is conducted in four cases (1) Geographically Global comparison, (2) Over Ocean, (3) Over Antarctica, (4) Over Greenland.

Figure 3.5 summarizes the GRACE-type mass rate from available GIA models. The statistical information is summarized in Table 3.7.

Figure 3.13 summarizes the GRACE-type mass rate over Antarctica (Whole Antarctica, East Antarctica, West Antarctica and Antarctica Peninsula) and the statistical information is summarized in Table 3.8.

Figure 3.14 summarizes the GRACE-type mass rate over Greenland and the statistical information is summarized in Table 3.9.

It is obvious that models differ more significantly in geoid rate than in uplift rate. When applying GIA model in GRACE processing, one need to convert the geoid rate to surface density change rate (or, equivalent water height change rate after divided by density of water ρ_W) following *Wahr et al.* [1998], here one multiplier factor $\left(\rho_E(2n+1)\right)/\left(3\rho_W\left(1+k_n^{'}\right)\right)$ is applied to the geopotential spherical harmonic coefficients that comes from GIA GRACE Level-2 monthly product, where ρ_E and ρ_W are density of Earth and Water respectively, n is the degree of spherical harmonic coefficients, and $k_n^{'}$ is degree n load Love number which decreases along with increasing n (see Figure 2.1), so it is obvious that the differences between geoid rate will be amplified when converting them to surface mass density change rate or equivalent water height.

Therefore, it is vital to choose a more accurate GIA model when estimating ice mass changes over Antarctica. To better modeling the GIA model over Antarctic, or same as global, the two inputs, namely, the ice loading history and Earth model, need to be provided as accurate as possible beforehand.

Table 3.7 Statistics of GRACE-type mass rate over Ocean.

Model	Ocean between latitude 90°N to 90°S GIA correction (mm/yr)	Ocean between latitude 66°N to 66°S GIA correction (mm/yr)	Selected Sea-Level Budget Study Region GIA correction (mm/yr)
Pau_5_R	−1.29	−1.24	−1.21
Pel_4_VM2	−1.10	−1.07	−1.02
Pel_5_VM2_R	−1.32	−1.32	−1.33
Pel_5_VM2_R_O	−1.78	−1.74	−1.76
Pel_5_VM4_R_O	−1.65	−1.59	−1.60
SaS_1	−0.74	−0.66	−0.68
SaS_3	−1.80	−1.77	−1.72
SKM_O_R	−1.23	−0.95	−0.84
SVv_3_REF	−1.88	−1.83	−1.80
SVv_L_ALT	−0.57	−0.44	−0.37
vdW_5	−1.00	−0.97	−0.96
vdW_5_R	−1.10	−1.08	−1.09
WaO_EGOD	−0.94	−0.99	−1.03
WaW_4	−1.52	−1.57	−1.59
WaW_5	−1.68	−1.68	−1.69
Mean and STD	**−1.31±0.40**	**−1.26±0.43**	**−1.25±0.44**

Table 3.8 Statistics of GRACE-type mass rate over Antarctica.

Model	Entire Antarctica GIA correction (Gton/yr)	East Antarctica GIA correction (Gton/yr)	West Antarctica GIA correction (Gton/yr)	Antarctic Peninsula GIA correction (Gton/yr)
Pau_5_R	120.3	78.2	37.6	4.5
Pel_4_VM2	137.1	91.4	38.6	7.5
Pel_5_VM2_R	105.5	62.6	37.7	5.2
Pel_5_VM2_R_O	64.2	22.8	23.8	17.7
Pel_5_VM4_R_O	70.3	31.0	22.1	17.3
SaS_1	17.9	15.0	2.6	0.3
SaS_3	220.7	143.7	67.2	9.9
SKM_O_R	89.3	26.8	58.5	4.5
SVv_3_REF	240.3	160.6	72.7	7.2
SVv_L_ALT	78.0	52.2	22.9	3.4
vdW_5	101.7	68.1	30.2	3.6
vdW_5_R	98.6	62.3	32.5	4.0
WaO_EGOD	109.0	63.3	40.4	5.1
WaW_4	157.9	109.8	41.2	6.8
WaW_5	148.3	106.5	37.0	4.8
IJ05	52.7	25.4	22.8	4.7
W12a_v1_B	35.8	3.5	30.3	1.5
Mean and STD	**108.7±59.4**	**66.1±45.0**	**36.4±17.3**	**6.3±4.7**

Table 3.9 Statistics of GRACE-Type mass rate over Greenland.

Model	Greenland GIA correction (Gton/yr)
Pau_5_R	1.0
Pel_4_VM2	24.4
Pel_5_VM2_R	−3.6
Pel_5_VM2_R_O	−13.1
Pel_5_VM4_R_O	−11.1
SaS_1	2.1
SaS_3	34.3
SKM_O_R	18.9
SVv_3_REF	24.8
SVv_L_ALT	1.3
vdW_5	3.4
vdW_5_R	1.0
WaO_EGOD	−62.6
WaW_4	25.2
WaW_5	6.6
Mean and STD	**−3.5±23.1**

3.6 Chapter Summary

In this chapter, contemporary GIA models are summarized and compared in both spatial and spectral domain. In addition, two approximate inherent relations are adopted to check the GIA models.

GIA corrections for different geodetic measurements are described in detail and also compared for different research purpose. For example, the role of GIA in the sea-level rise study from measurement including tide gauge, radar altimetry and GRACE, and the role of GIA in ice mass balance study from GRACE over Antarctica and Greenland.

It is vital to choose the most appropriate GIA model in GRACE study, especially for the ice sheets mass balance study. One question is still open, that is, which GIA model is the best one?

Using the two relations, we could approximately know the misfits between the models and prediction from the relations, but that is not supposed to be used to rank the GIA models.

The other measurements, such as GPS, could be used to check the GIA model predicted vertical deformation, but limitations still exist, for example, it is difficult to separate the signal from present-day elastic loading from the GIA signal in the total measurement of GPS.

The accuracy of GIA models depends on not only the accuracy of chosen Earth model that is used to describe the structure of the Earth and its rheological parameters that used to calculate the Earth's response to its surface load, but also the Ice loading history that is as the input to the GIA modeling. Besides these, the modeling theory is also required to update to include 3-D Earth structure and also the sea-level equation is required to be refined.
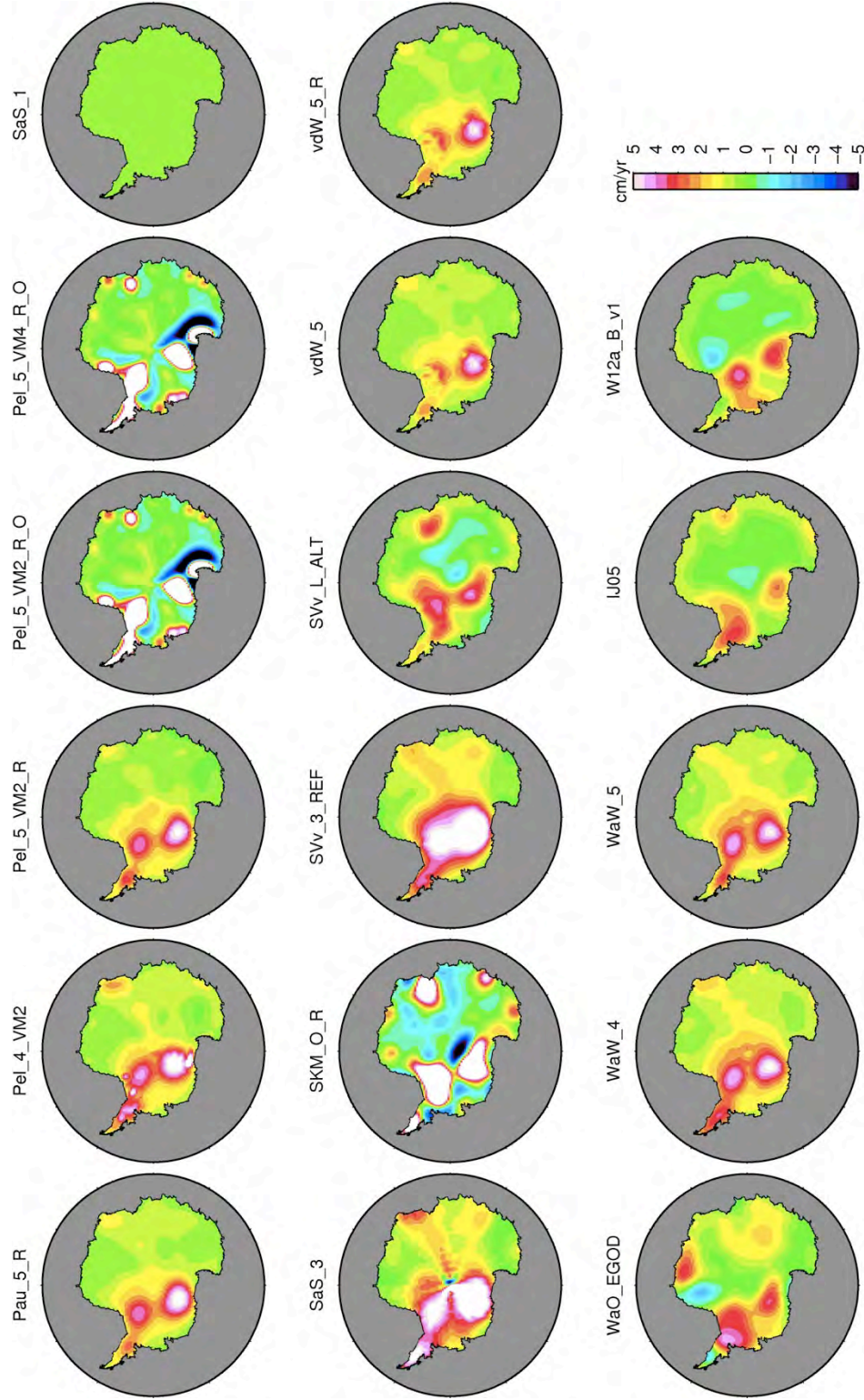
Figure 3.13 GRACE-type mass rate over Antarctica from 17 GIA models. Unit is cm/yr.
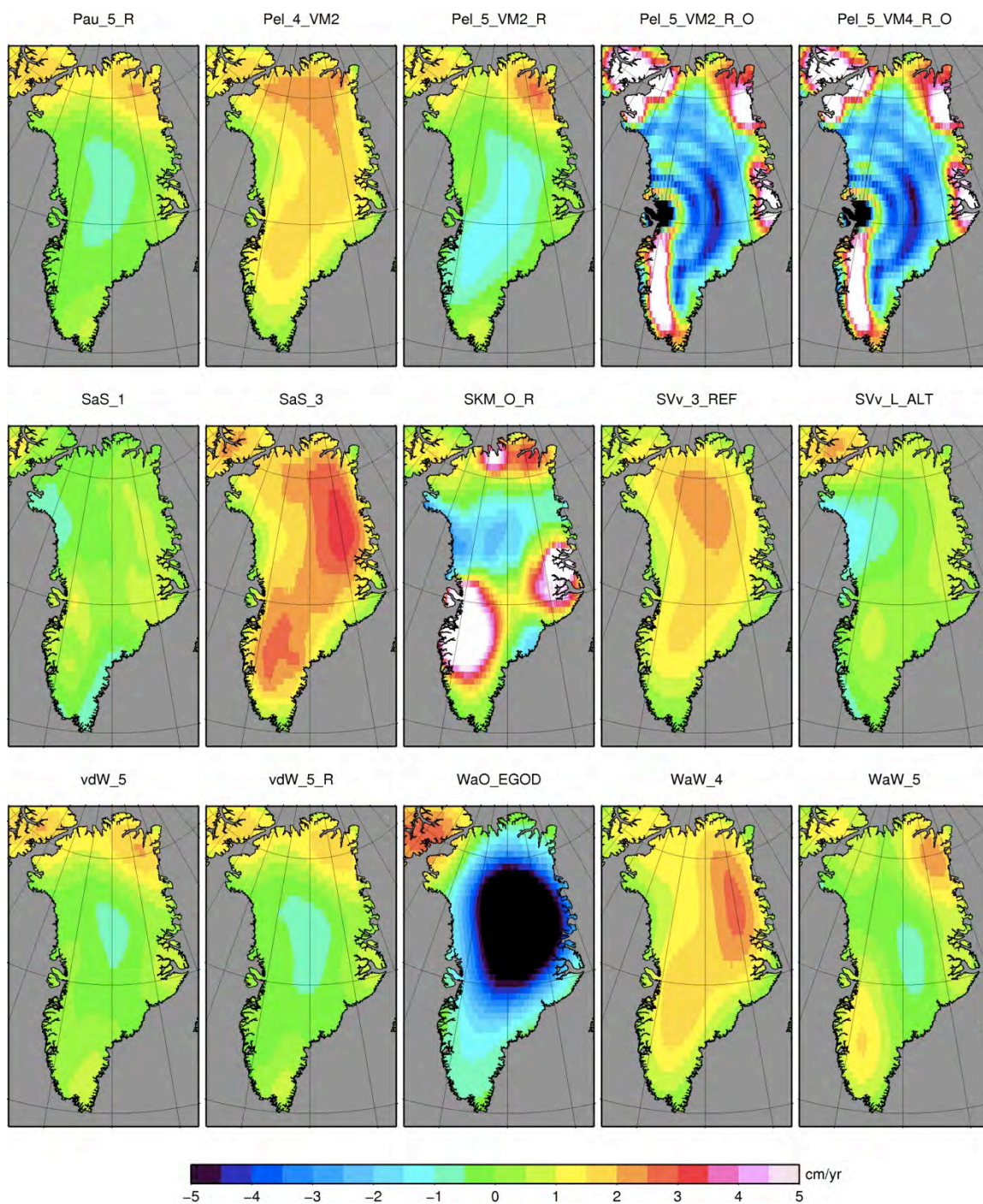
Figure 3.14 GRACE-type mass rate over Greenland from 15 GIA models. Unit is cm/yr.

Chapter 4   Geodetic Observations

This chapter describes the geodetic observations obtained from tide gauge, radar altimetry and Gravity Recovery And Climate Experiment (GRACE) satellite gravity mission.

These observations will be used later to study the sea level change after GIA correction. For each geodetic observation, the measurement principle is concisely described below.

4.1   Tide Gauge

Tide gauges measures the height of the water relative to a geodetic benchmark (local datum). The recorded sea-level is relative sea-level that is relative to the Earth's crust. Figure 4.1 illustrates how a tide gauge works.

Prior to 1990s, tide gauge is the primary measurement of sea-level change. Now there are more than 2000 tide gauges worldwide, most of which are established since 1950 [*Woodworth and Player*, 2003].

Two organizations are collecting and preserving tide gauge records around the world now. One is the Global Sea Level Observing System, which is a network of 290 tide gauges worldwide, the other is Permanent Service for Mean Sea Level (PSMSL), which consists of more than 2000 tide gauges around the world. In this study, the tide gauge records from PSMSL are extracted on July 18, 2012.

Long-term tide gauge records provided by the Permanent Service for Mean Sea Level (PSMSL) are used in this study. Figure 4.3 presents the basic statistics of the sites used in this study. In the total number of 1208 selected tide gauge stations, 1013 of them are located in the North hemisphere (See Figure 4.2 for the geographical plot).

All the monthly averaged Revised Local Reference (RLR) records available are used to extract secular mean sea-level trend. An Inverted Barometer (IB) correction is applied to the tide gauge records to take into account the static response of the ocean to the atmospheric pressure. The trend is extracted using a 6 parameters least square adjustments.

One of the limitations of tide gauge measurement comes from its sparse spatial distribution (spatial coverage). They are located only on the continental margin or the ocean islands (See Figure 4.2 for the spatial distribution), so the result could not be used to represent the global ocean. Another limitation is that due to the measurement is made relative to the Earth's crust, which can move vertically and create apparent sea level change that is not related to climate change. GIA is one of the causes of vertical displacement. In this study, we will focus on the relative sea-level contamination from GIA and provide the range this effect due to different GIA models.

44

A data set including selected 329 tide gauge stations are used, the criteria of selection is that the data length is larger than 15 years with the data completeness larger than 80 percent, and also the data span till year 2011. Figure 4.4 shows the geographically plot of the selected tide gauges stations. Most of the selected tide gauges (299 of 329) are located in the North hemisphere, such as North America, European and East Asia. This sparse and non-uniform distribution are the major limitations when using tide gauge record to study global sea-level change.
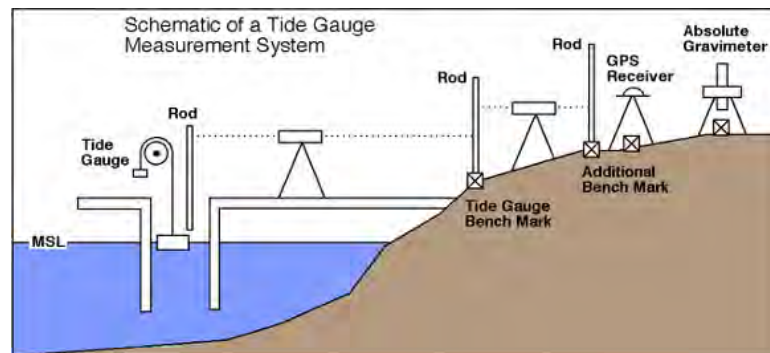
Figure 4.1: Scheme plot of how tide gauge works. [Courtesy: http://sealevel.colorado.edu/content/tide-gauge-sea-level]
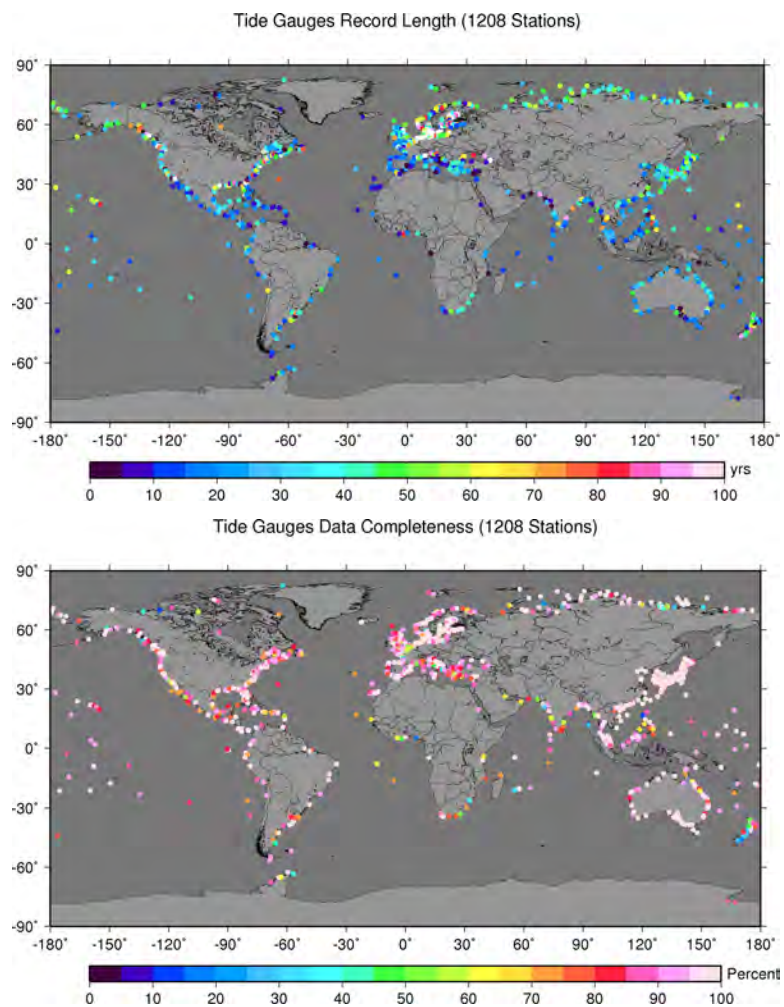
Figure 4.2: Length and completeness of tide gauges records from PSMSL 1208 stations. Data are extracted from PSMSL on July 18th, 2012. Top: Length of tide gauges record (unit: year). Bottom: Completeness of tide gauges.

46
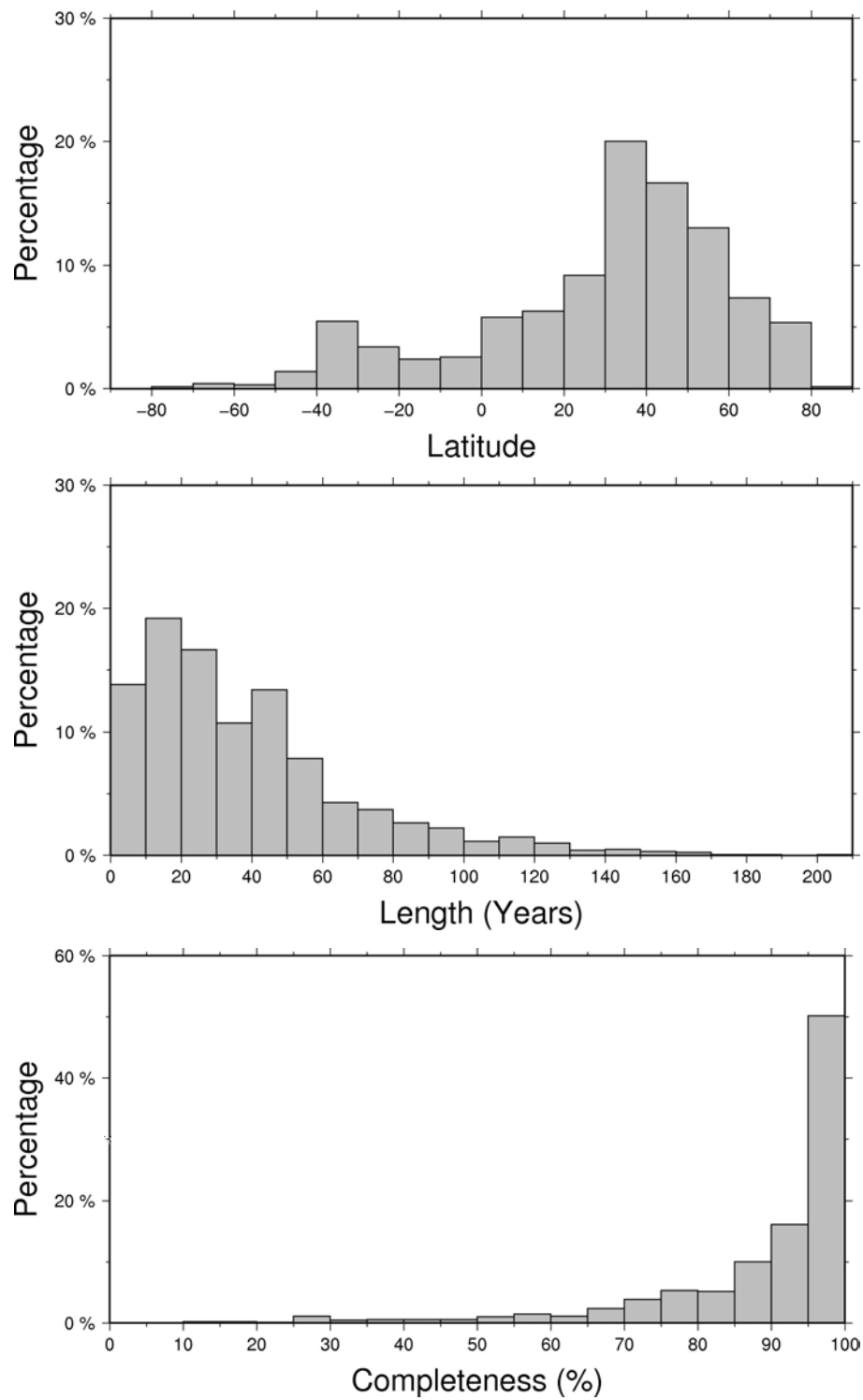
Figure 4.3: Top: Histogram of tide gauge distribution along latitude. Middle: Histogram of gide gauge record length (Unit: Years). Bottom: Histogram of tide gauge record completeness.

Selected Tide Gauge Sites (326 Stations, 1948–2011)

Selected Tide Gauge Sites (321 Stations, 1992–2011)
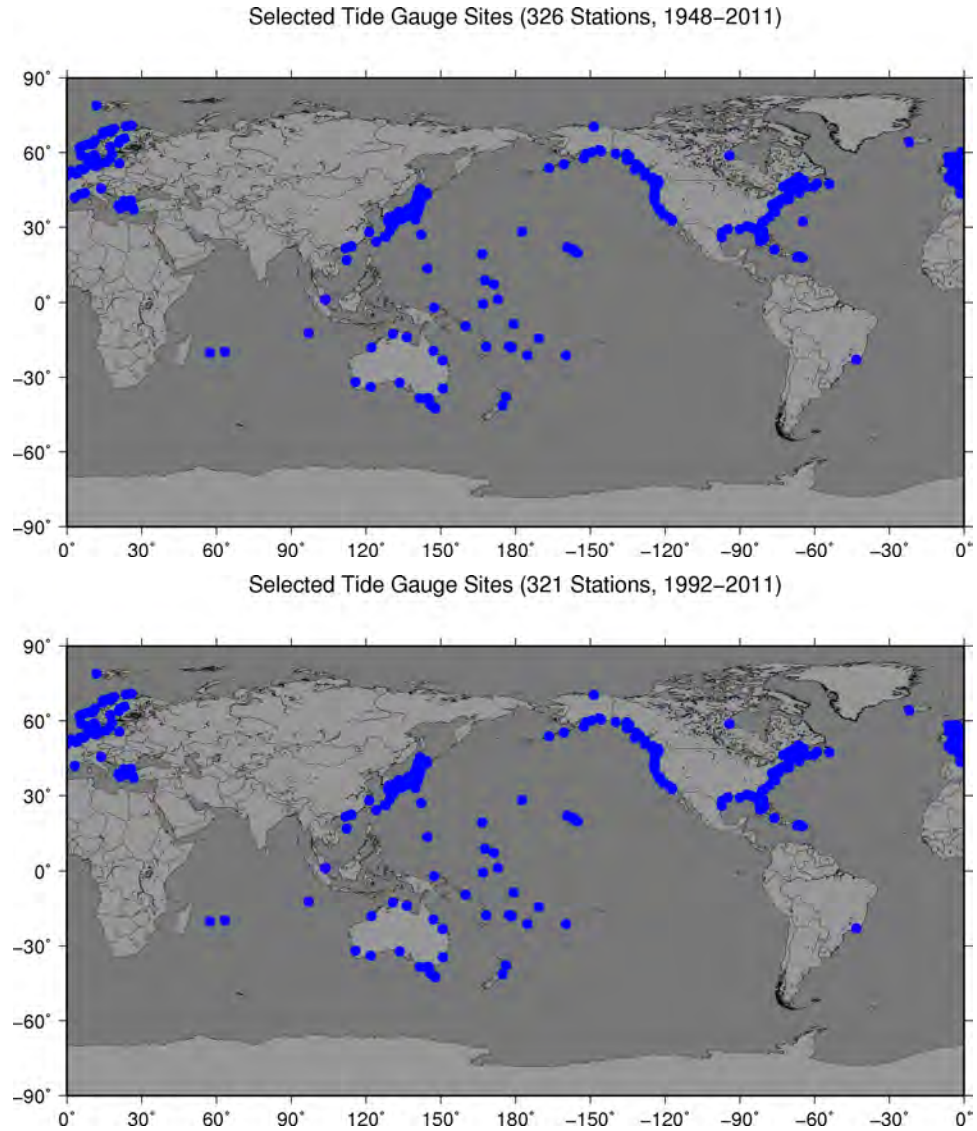
Figure 4.4: Top: Geographical plot of selected 326 tide gauge stations (1948–2011). Bottom: Selected 321 tide gauge stations (1992–2011).

4.2 Radar Altimetry

The first altimeter mission to observe the global ocean is Seasat that is launched in 1978, after that the routine measurement of sea-level starts from the launch of TOPEX/Poseidon (1992–2006) and ERS-1 (1991–2000), continued with ERS-2 (1996–2011), Geosat Follow-on (1998–2001), Jason-1 (2001–present), Envisat (2002–2012) Jason-2 (2008–present) and Cryosat-2 (2010–present). Satellite altimetry measures the range between satellite and the sea surface. The principle of Radar Altimetry is schemed in Figure 4.5. For the spatial coverage, TOPEX and Jason series measure the global ocean between 66° N and 66°S, Geosat and Geosat-Follow on covers latitude between 71° N and 71°S; ERS-1 and -2 and Envisat covers the latitude between 81.5° N and 81.5°S; Cryosat-2 covers the latitudes between 88° N and 88°S. For the repeated measurement, it

48

is 10 days for TOPEX and JASON series, 17 days for Geosat and Geosat Follow-on, 35 days for ERS-1 and -2 and Envisat, and 365 days with 30 days sub-cycles for Cryosat-2.

The orbit of satellite is determined using tracking data from Satellite Laser Ranging network, the Doppler Orbitography and Radio-positioning Integrated by Satellite (DORIS) land-based beacons, and the Global Navigation Satellite System (GNSS).

To study the global sea-level change from radar altimetry measurement, corrections such as atmospheric (ionosphere, dry and wet troposphere) delays, ocean, solid Earth and polar tides, sea state bias and inverted barometer correction are required to be applied before interpreting the results.

The measurement includes the large-scale ocean basin deformation, which is caused by GIA, and it must to be removed from the signal in order to study the sea-level rise.

In this study, Multi-mission satellite radar altimetry observations are obtained from the AVISO DUACS V3.0 data product (Data Unification & Altimeter Combination System, http://www.aviso.oceanobs.com). A gridded secular sea-level trend is extracted by using weekly product data from 1992 to 2011. Corrections such as atmospheric refraction, tides, sea-state bias and inverted barometer correction are applied during processing.

Figure 4.6 shows the data coverage of the satellite derived sea-level change, and Figure 4.7 shows the geographical plot of the extracted mean sea-level trend, the time series are shown in Figure 4.8.
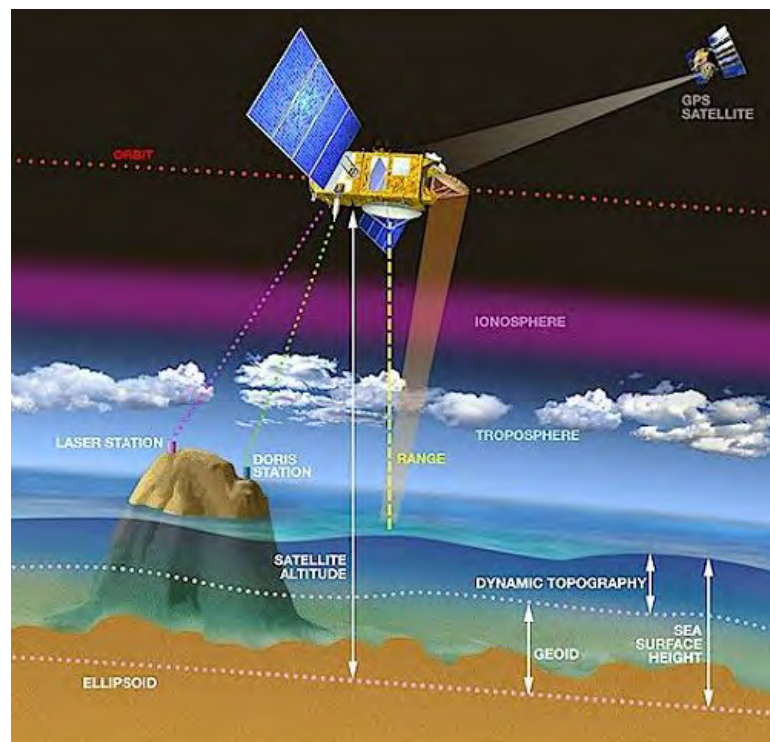
Figure 4.5: Scheme plot of Altimetry. [Courtesy: http://www.aviso.oceanobs.com/en/altimetry/principle/basic-principle.html]
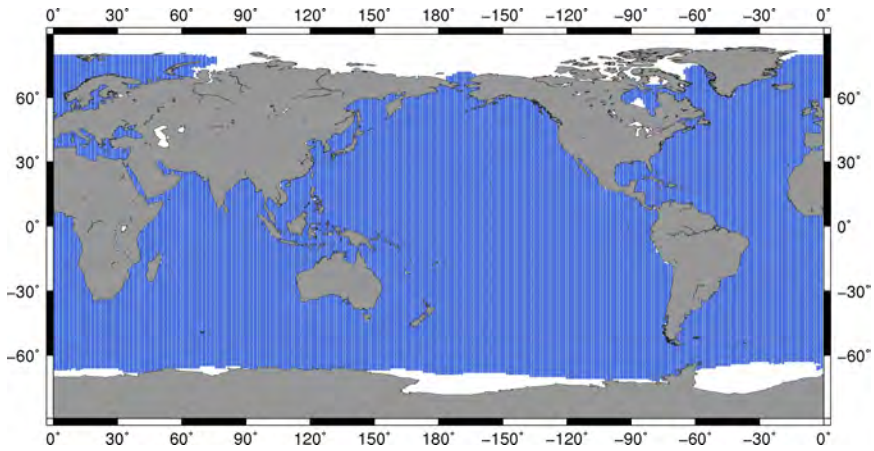
Figure 4.6 Data coverage of multi-satellite measurement (1993–2011). Blue area denotes the data coverage.
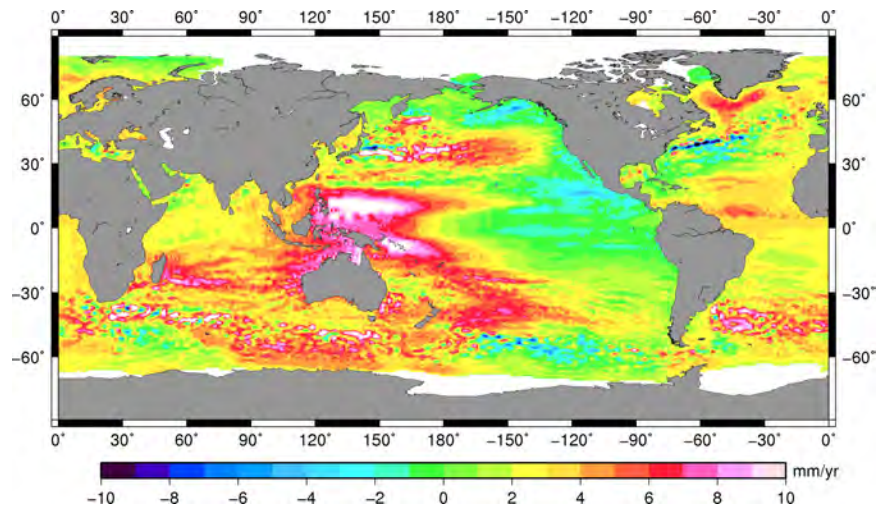

Figure 4.7 Geographical plot of measured sea-level change (1993–2011).
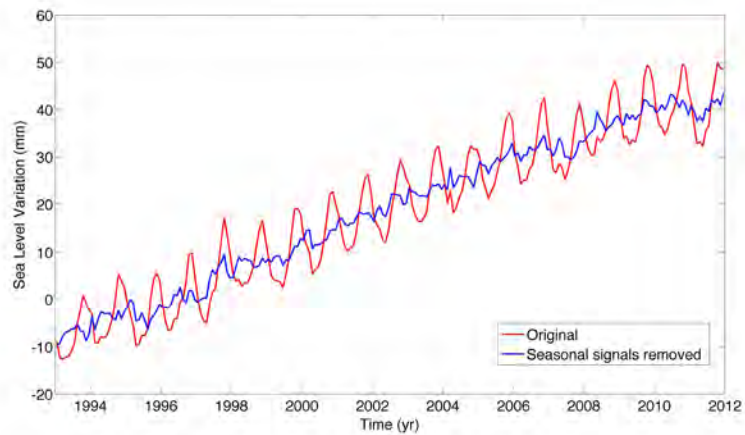

Figure 4.8 Time series of sea-level change computed from multi-satellite measurement (1993.01~2011.12). Red line denotes the time series with seasonal signals included; blue line indicates the time series after removing seasonal signals.

50

4.3 GRACE Data and Comparison

Launched by 2002, Gravity Recovery and Climate Experiment (GRACE) provide the global gravity field of the Earth in monthly temporal resolution and in hundred kilometers spatial resolution [*Tapley et al.*, 2004]. Principle of GRACE measurement is illustrated in Figure 4.9. Low-to-low satellite tracking provides the more information in along track than sidetrack, and also 89.5 degree inclination makes it more sensitive along latitude than longitude.
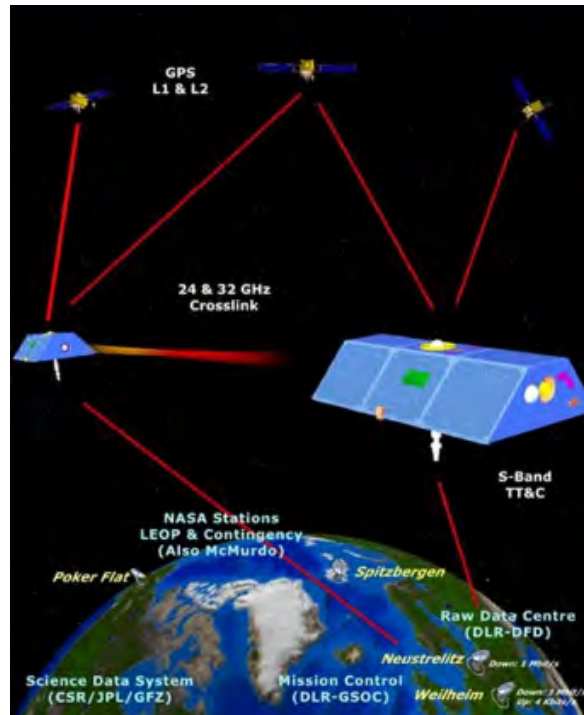
Figure 4.9: Scheme of GRACE. [Courtesy: http://www.csr.utexas.edu/grace/]

In this study, GRACE Level-2 RL05 monthly data product from three official data centers (CSR, GFZ and JPL) are used from each data center, three types of their products (GSM, GAC and GAD) are used.

According to GRACE Level-2 user handbook, 'G' here denotes 'geopotential coefficients', 'S' denotes 'estimate made from only GRACE data', 'A' denotes 'average of any background model over a time period', 'M' denotes the 'estimates of the static field', 'C' denotes the 'Combination of non-tidal atmosphere and ocean', 'D' denotes 'bottom-pressure over oceans, zero over land'. Thus, 'GSM' indicates the geopotential coefficients of static field that are estimated from only GRACE data. 'GAC' indicates the geopotential coefficients of the combination of non-tidal atmosphere and ocean that are averaged from background model over a certain time period. 'GAD' indicates that the geopotential coefficients of ocean bottom-pressure that are averaged over a certain time period. Over ocean, GAC and GAD product can be considered identical.

There are 4 months missing in GSM product due to insufficient good observation in the computation, the missing months are: June 2003, January 2011, June 2011, May 2012.

In this study, the missing months are linearly interpolated using two months before and two months after.

Spherical harmonic coefficients along with the spherical function can be used to describe the gravity field (or any other functions on the sphere). Degree denotes different spherical function, or can be understood as signal decomposing. The maximum degree limits the spatial resolution. An approximately half-wavelength resolution can be computed as

$$\Delta\theta = \frac{180^\circ}{N_{max}}$$

4-1

In this study, GRACE Level-2 RL05 monthly product provides up to 60, so the half-wavelength resolution is $\approx 333\ km$.

Mass change trend is estimated from data spanning from 2003.01 to 2011.12.

4.3.1 Data Processing

The relationships between those potential coefficients and different geophysical phenomena, such as spherical harmonic coefficient relative to geoid change, free-air gravity disturbance change, surface mass density (or equivalent water height) are provided in Chapter 2 under the thin-layer approximation using elastic loading theory. Here only the necessary equations were shown.

To make it easy, spherical harmonic expansion is given on Earth surface. According to *Chao et al.* [1987], the geoid *N* could be described as:

$$N(\theta,\lambda) = a\sum_{n=0}^{\infty}\sum_{m=0}^{n}\left\{\bar{C}_{nm}\cos m\lambda + \bar{S}_{nm}\sin m\lambda\right\}\bar{P}_{nm}(\cos\theta)$$

4-2

where a is the mean radius of the Earth, (θ,λ) denotes the co-latitude and longitude respectively, n and m are the degree and order. $\bar{C}_{nm}$ and $\bar{S}_{nm}$ are the (fully-normalized) spherical harmonic coefficients (SHCs). $\bar{P}_{nm}$ is the normalized associated Legendre function.

For GRACE monthly solutions, when a reference filed or averaged filed is subtracted, the time dependent geoid change relative to the reference filed or averaged filed can be obtained as:

$$\Delta N(\theta,\lambda) = a\sum_{n=0}^{\infty}\sum_{m=0}^{n}\left\{\Delta\bar{C}_{nm}\cos m\lambda + \Delta\bar{S}_{nm}\sin m\lambda\right\}\bar{P}_{nm}(\cos\theta)$$

4-3

Spherical harmonic expansion of changes in surface density is shown as:

$$\Delta\sigma(\theta,\lambda) = a\rho_W\sum_{n=0}^{\infty}\sum_{m=0}^{n}\left\{\Delta\hat{C}_{nm}\cos m\lambda + \Delta\hat{S}_{nm}\sin m\lambda\right\}\bar{P}_{nm}(\cos\theta)$$

4-4

where ρ_W denotes the density of water.

If the geoid change was caused by a thin layer mass density change near the Earth surface, by using the elastic loading theory, we could have the relationship between spherical harmonic coefficients and surface mass density with a thin layer assumption as:

$$\begin{Bmatrix} \Delta \hat{C}_{nm} \\ \Delta \hat{S}_{nm} \end{Bmatrix} = \frac{\rho_E}{3\rho_W} \frac{2n+1}{1+k_n^{'}} \begin{Bmatrix} \Delta \bar{C}_{nm} \\ \Delta \bar{S}_{nm} \end{Bmatrix} \qquad \text{4-5}$$

where $k_n^{'}$ degree n load Love number and ρ_E is the average density of the Earth.

Substitute (4-5) into (4-4), yields to:

$$\Delta \sigma (\theta, \lambda) = \frac{a\rho_E}{3} \sum_{n=0}^{\infty} \left(\frac{2n+1}{1+k_n^{'}} \right) \sum_{m=0}^{n} \left\{ \Delta \bar{C}_{nm} \cos m\lambda + \Delta \bar{S}_{nm} \sin m\lambda \right\} \bar{P}_{nm} (\cos \theta) \qquad \text{4-6}$$

This is the formula that is used to compute the surface mass density from GRACE measurement. *Wahr et al.* [1998] provides the relationship between spherical harmonic coefficient and surface mass density with a thin layer assumption, makes GRACE a extremely useful technique to monitor the hydrology signals, as well as polar ice melting. In order to fully explore GRACE measurement, it is convenient to convert the geopotential spherical harmonic coefficients into gravity change instead of the surface density change because we are interested more than the hydrology signals.

From changes in spherical harmonic coefficients of geoid to changes in gravity change:

$$\Delta g (\theta, \lambda) = \frac{GM_E}{a^2} \sum_{n=0}^{\infty} (n+1) \sum_{m=0}^{n} \left\{ \Delta \bar{C}_{nm} \cos m\lambda + \Delta \bar{S}_{nm} \sin m\lambda \right\} \bar{P}_{nm} (\cos \theta) \qquad \text{4-7}$$

The time-variable gravity is the sum of the gravitational signals originating from all geophysical sources. Sorting out different geophysical signals in the data is a challenge, but in principle can be facilitated by recognizing the different temporal and spatial characteristics of different geophysical phenomena.

According to *Swenson and Wahr* [2006], high degree of spatial correlation exists in GRACE errors and behaves as the long south-north linear features (see Figure 4.10 for example) which is called 'stripes'. In order to reduce these errors, de-correlation procedure is conducted according to *Duan et al.* [2009].

Besides the 'stripe' error, high degree spherical harmonic coefficients still include large errors, thus smoothing is still needed [*Guo et al.*, 2010; *Jekeli*, 1981]. Leakage reduction is also performed to reduce the leakage error according to *Guo et al.* [2010].

4.3.2 Comparison between Results from Three Data Centers

Without any post processing, the gravity trends extracted from three data centers with truncation to specific degree are plotted in Figure 4.10, Figure 4.11 and Figure 4.12. It is shown that three data centers provide almost the same result.

The degree variances from the raw data are plotted in Figure 4.13 and Figure 4.14 after subtracting the mean gravity field averaged from all months product.

Figure 4.15 shows the degree variances of the extracted trend from GRACE GSM product and GAC product with comparison to two GIA models (Pau_5_R and

Pel_5_VM2_R). GRACE solutions from three data centers are similar from degree 3 to 40, and differ from each other after degree 40.
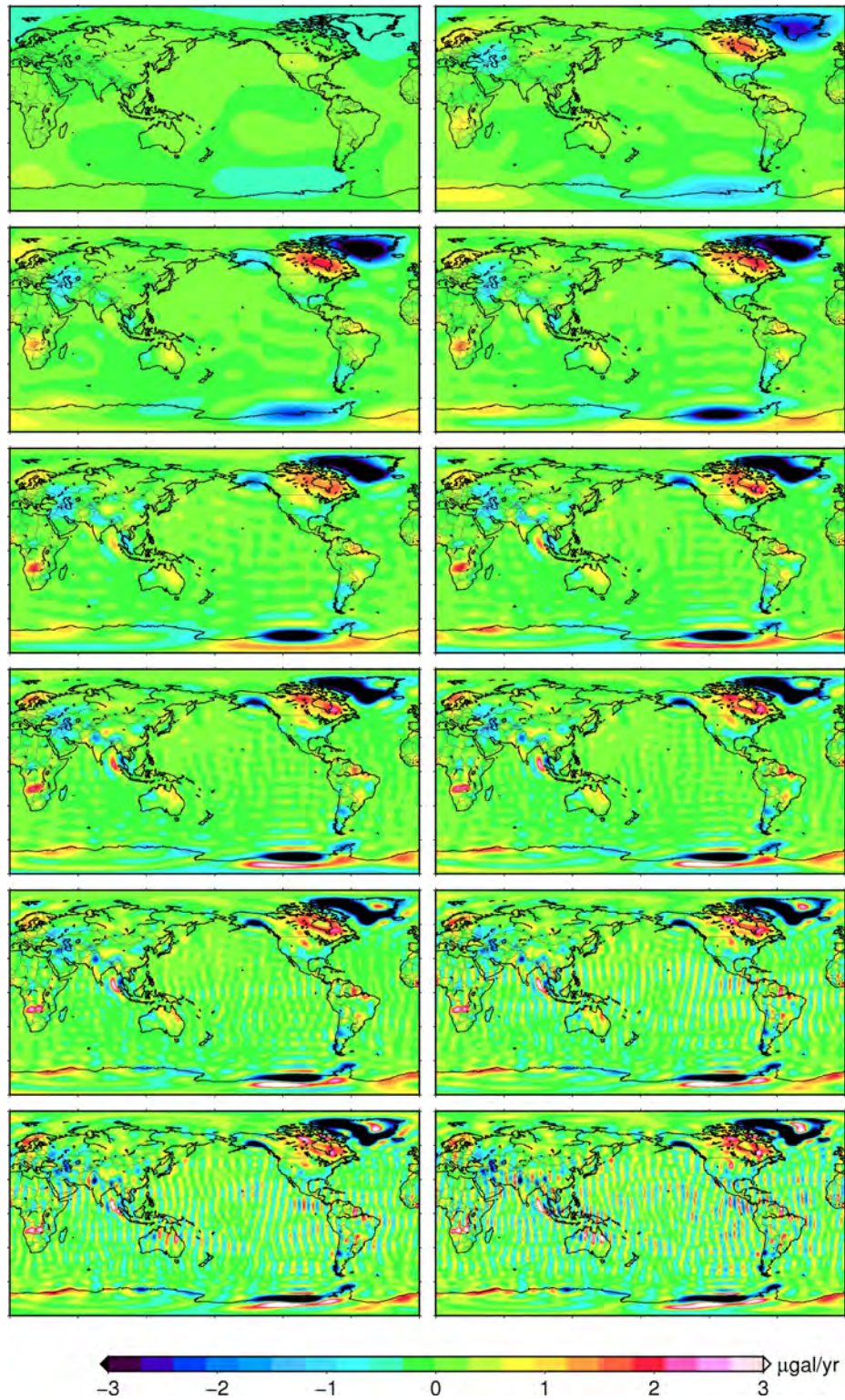
Figure 4.10 Trend of gravity change derived from CSR RL05 monthly solution against to different truncate degree. From top left to bottom right: 5, 10, 15, 20, 25, 30, 35, 40, 45, 50, 55, 60
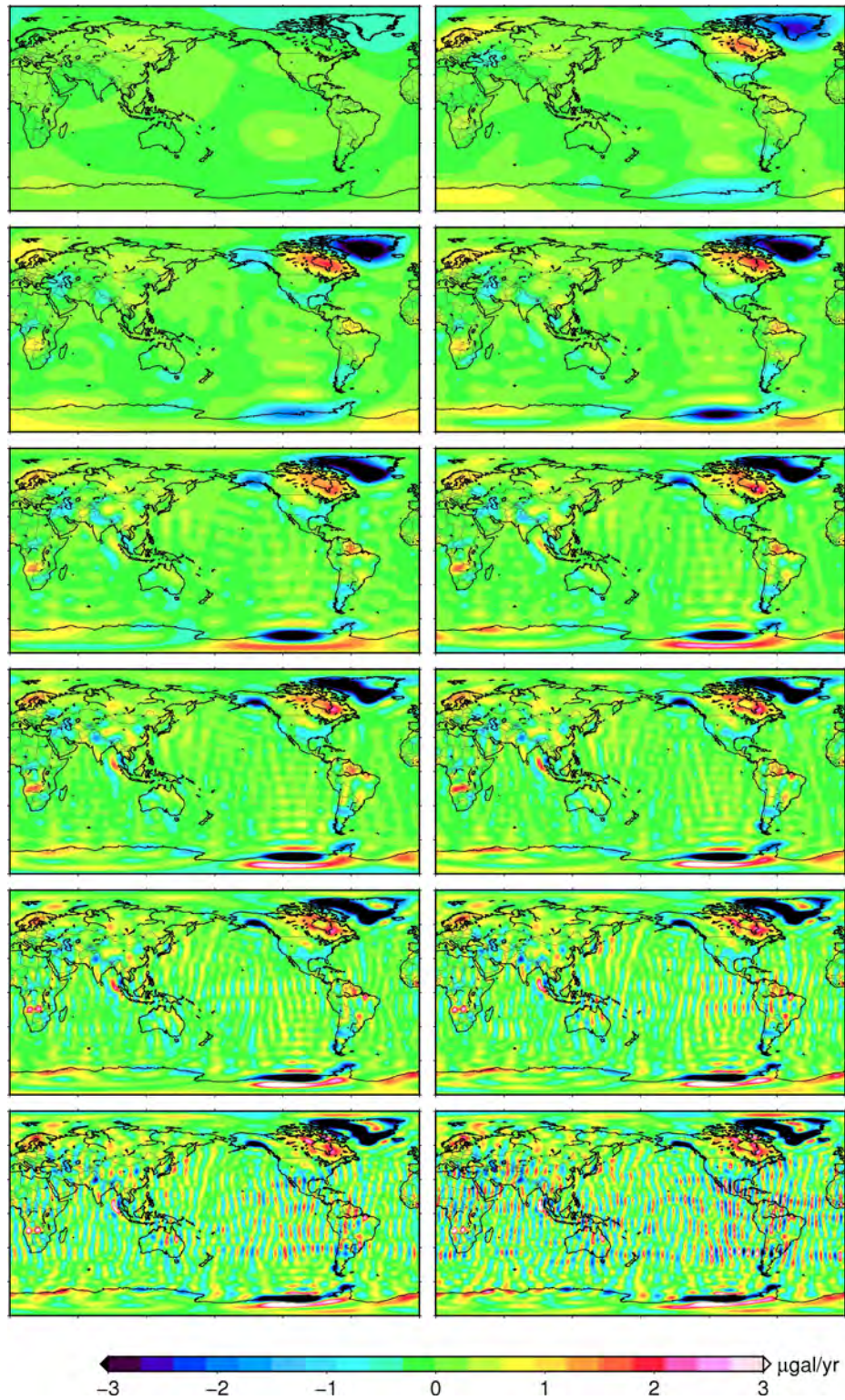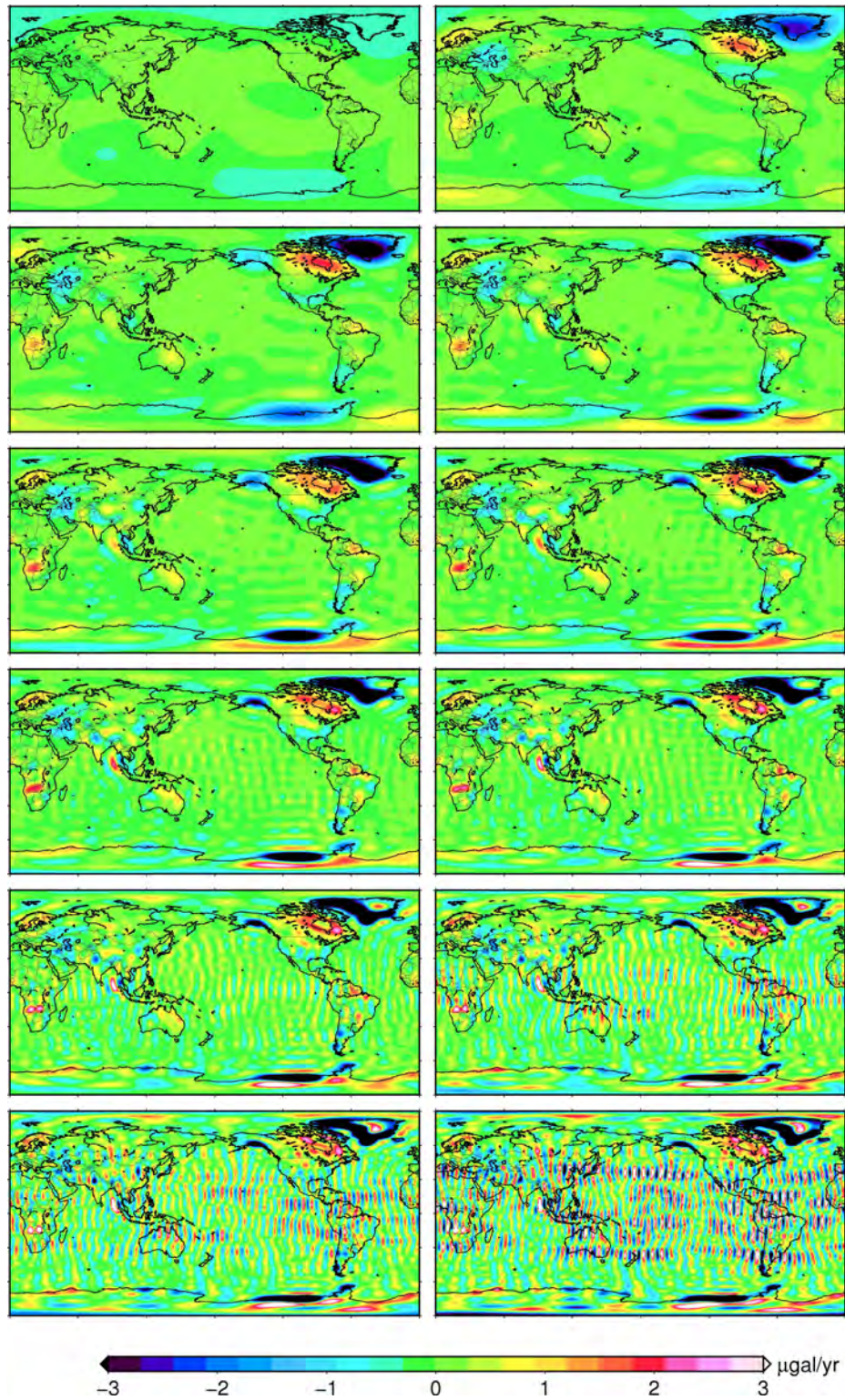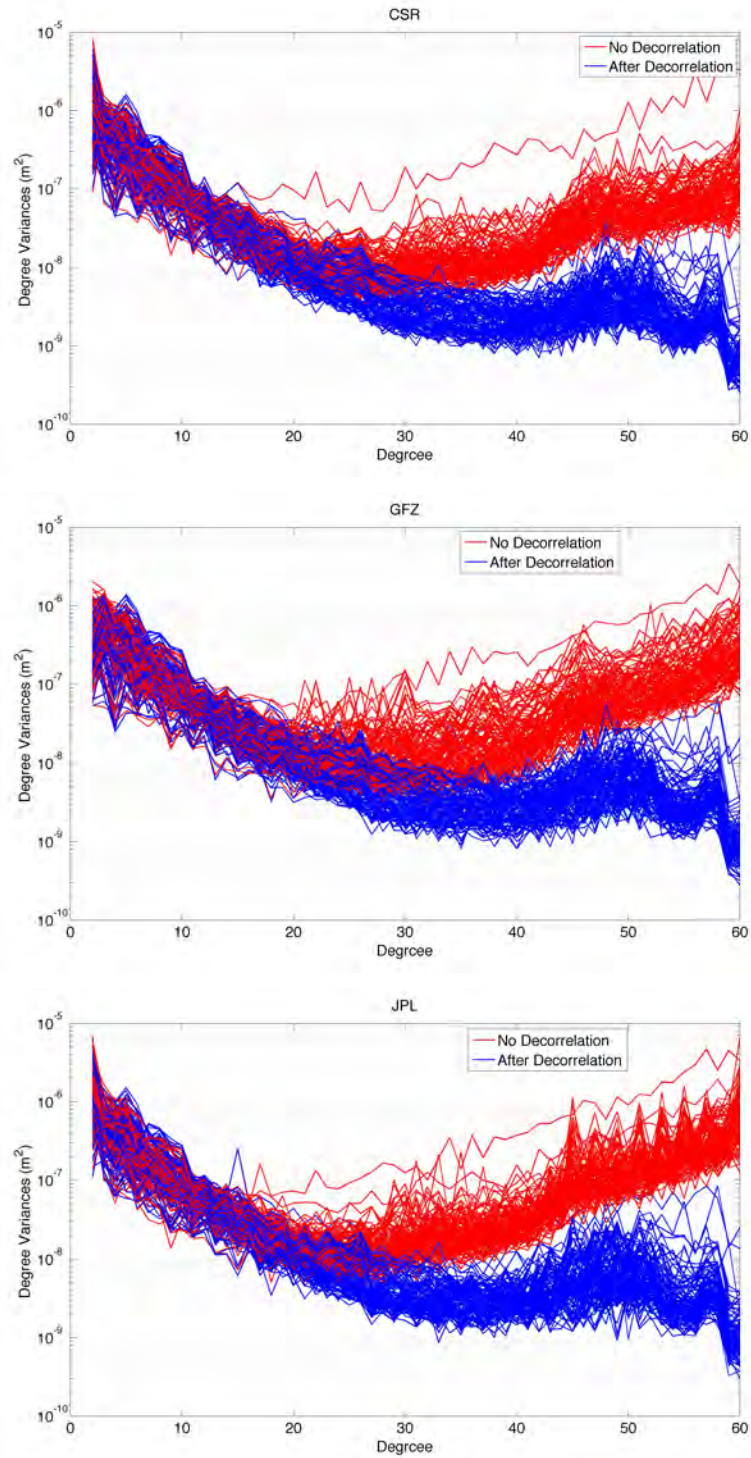
Figure 4.11 Trend of gravity change derived from GFZ RL05 monthly solution against to different truncate degree. From top left to bottom right: 5, 10, 15, 20, 25, 30, 35, 40, 45, 50, 55, 60

Figure 4.12 Trend of gravity change derived from JPL RL05 monthly solution against to different truncate degree. From top left to bottom right: 5, 10, 15, 20, 25, 30, 35, 40, 45, 50, 55, 60

Figure 4.13 Degree variances extracted from GRACE RL05 monthly solution with mean field removed. Top: CSR; Middle: GFZ; Bottom: JPL.

58
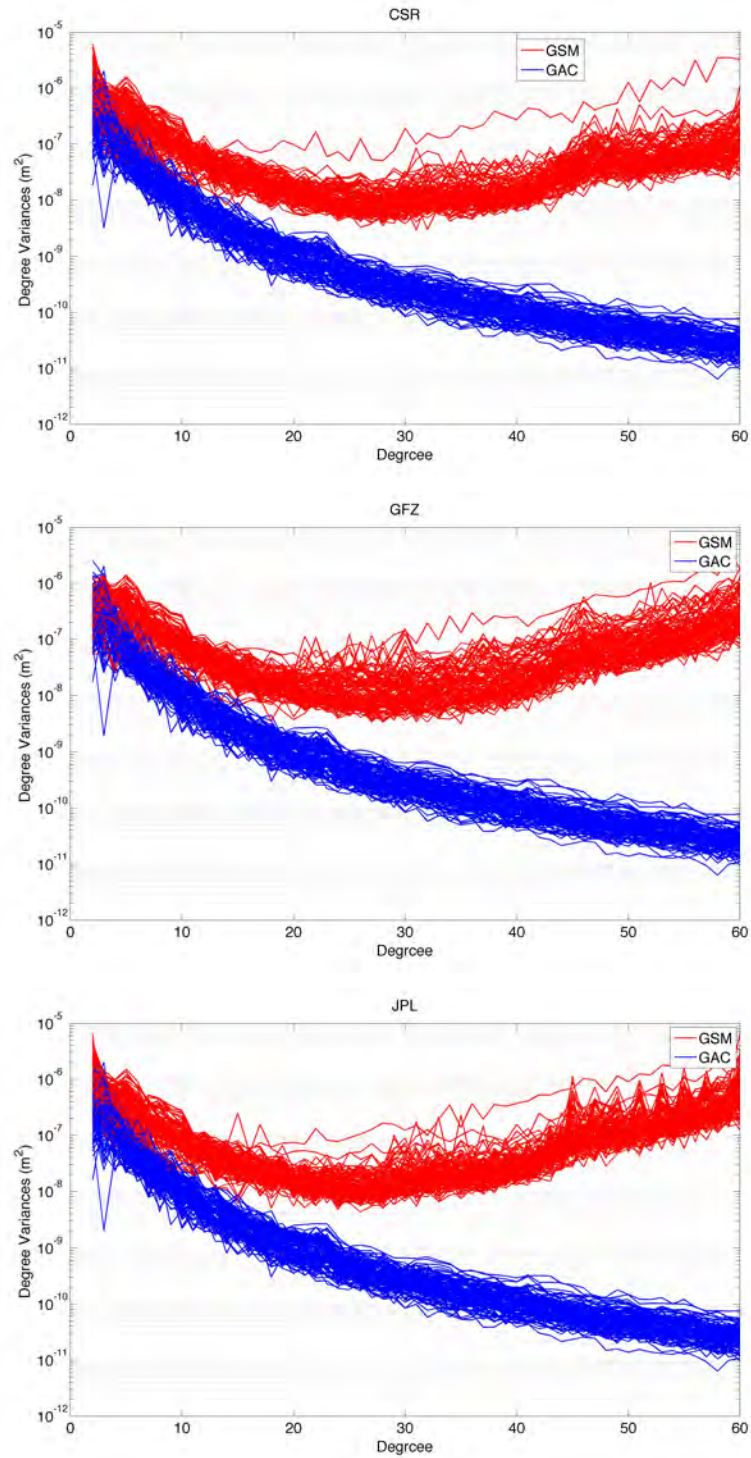
Figure 4.14 Degree variances extracted from GRACE RL05 monthly solution with mean field removed. GSM outlier (top red): January 2003; GAC outlier (peaks): April 2007. Top: CSR; Middle: GFZ; Bottom: JPL.
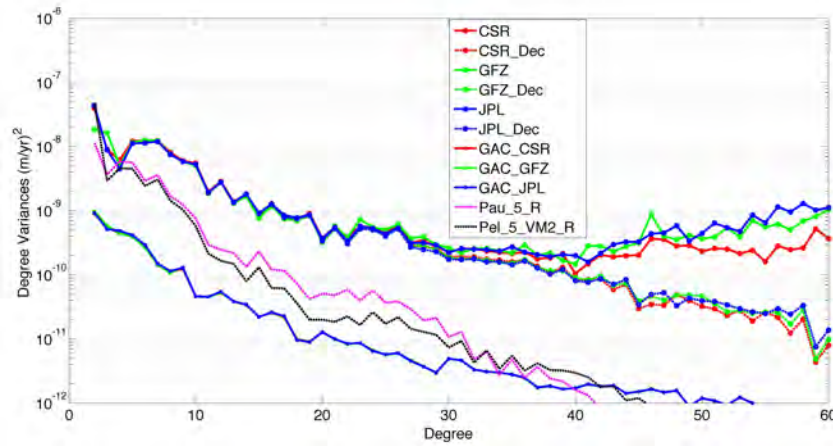
Figure 4.15 Degree variances extracted trend from three data centers and also two GIA models. GRACE solutions from three data centers are similar from degree 3 to 40, and differ from each other after degree 40.

4.4   Chapter Summary

In this chapter, three geodetic observations about sea-level study that are used in this dissertation have been introduced. The data processing is also described in general.

For tide gauge, a statistical analysis is made to show the advantage and disadvantage of tide gauges in the sea-level study.

For radar altimetry, the time span and coverage of the data used are provided.

For GRACE data, comparison is made within three data centers (CSR, GFZ and JPL). Comparison result shows that post-processing is needed for GRACE RL05 in order to obtain better estimation of surface mass redistribution such as polar ice melting and land hydrology.

Chapter 5   Recent Earth's Oblateness Change Interpretation from Polar Ice Melting using Sea-level Fingerprint Method

5.1   Introduction

The Earth's dynamic oblateness, represented by J_2 gravitational parameter, is used to describe Earth's ellipsoidal shape, that is, the radius of the equator is about 21km larger than the polar radius. Most of the oblateness come from Earth's rotation that makes mass accumulated around the equator.

Start from Lageos-1, Satellite Laser Ranging (SLR) technique is used to precisely determine the low-degree spherical harmonic components of Earth's gravity field and also their temporal variations [*Cheng and Tapley*, 2004; *Yoder et al.*, 1983]. In the observed J_2 time series, the dominant signatures are (1) Secular decrease, (2) Seasonal variations, and (3) Inter-annual variations (Figure 5.1).

Many attempts are made in order to explain the observed variations of J_2. It is widely accepted that the secular decrease is caused by ongoing Glacial Isostatic Adjustment (GIA) [*Mitrovica and Peltier*, 1993; *Rubincam*, 1984; *Yoder et al.*, 1983], Figure 5.2 shows the long-term J_2 time series after removing GIA effect that predicted from GIA forward modeling. Based on this assumption, the observed decrease of J_2 could be used to infer the Earth rheology parameter, for example, the viscosity of the upper mantle and lithosphere thickness [*Devoti et al.*, 2001]; and the viscosity of the Lower mantle [*Rubincam*, 1984].

In addition, the water movement among atmosphere, oceans, and cryosphere causes the J_2 changes with time. Start from mid-1990s, the departure from secular decrease in the time series of J_2 indicates that something had been fundamentally changed [*Cox and Chao*, 2002]. Several explanations are proposed to address this issue, including mountain glacier melting [*Dickey et al.*, 2002; *Marcus et al.*, 2009], departures of the 18.6 year tide from its elastic plus equilibrium ocean value [*Benjamin et al.*, 2006], El Niño–Southern Oscillation (ENSO) [*Cheng and Tapley*, 2004; *Marcus et al.*, 2009], Greenland and Antarctic ice mass loss [*Nerem and Wahr*, 2011].

Launched by 2002, the Gravity Recovery and Climate Experiment (GRACE) twin-satellite gravity mission, has been providing the measurements of the Earth's gravity field with monthly temporal resolution, and a few hundred kilometers in spatial resolution [*Wahr et al.*, 2004].

Nerem and Wahr [2011] studied the recent changes in Earth's oblateness using SLR and GRACE data, and concluded that recent mass loss from Antarctica and Greenland are the dominant contributor to the current GIA-corrected J_2 trend. *Cheng et al.* [2013] used over three decades SLR observations to do a comprehensive analysis and claimed that the change in Earth's oblateness is decelerating.

In this study, we extend the study from *Nerem and Wahr* [2011] and check the other contributions from different glaciers using sea-level fingerprint method. This study will focus on the surface mass load change contributes to recent changes in Earth's dynamic oblateness. First, sensitive test is made for Antarctic and Greenland ice sheets and also several glaciers including Alaska, Patagonia, Canadian Arctic Archipelago, Asian High Mountain, Svalbard Island and Iceland. Second, mass changes extracted from GRACE are used to study contributions to J_2 variations from these regions respectively. In the end, comparison is made with the SLR derived J_2 time series. In the comparison, the effect of GIA will also be discussed.
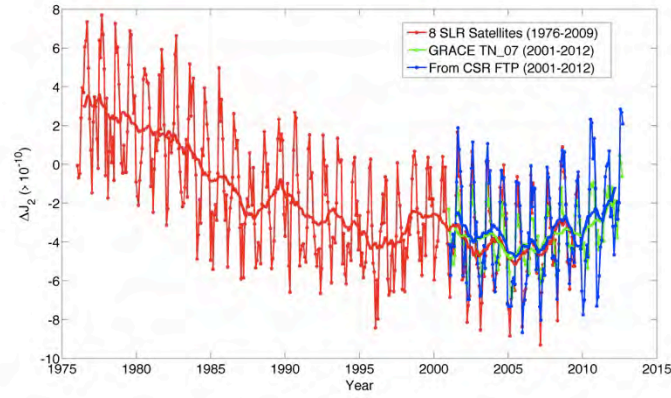
Figure 5.1 Variations of J_2 from satellite laser ranging. Red: Long term estimation according to *Cheng and Tapley* [2004]. Green: GRACE TN-07, AOD1B added back. Blue: Downloaded from CSR FTP. Annual smoothing is applied and shown as the solid lines.
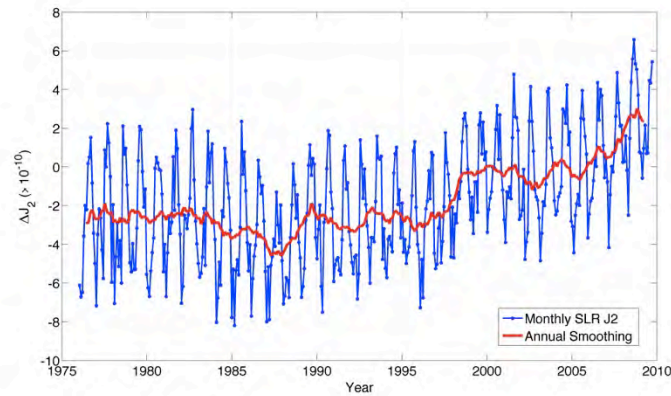

Figure 5.2 Variations of J_2 from satellite laser ranging after removing Paulson GIA model (–3.6E-11 yr^{-1}).

5.2 Relation between Changes in Earth's Oblateness and Large-Scale Surface Mass Redistribution

5.2.1 Surface Mass Load

Earth's dynamic oblateness is proportional to normalized geopotential spherical harmonic of degree 2, order 0, given as,

$$J_2 = -\sqrt{5} \times \bar{C}_{20} \qquad\qquad 5\text{-}1$$

The physical relationship between the change in surface mass load and the change in the Earth's gravitational field is given as *Chao and Gross* [1987]

$$\Delta\{\bar{C}_{nm}, \bar{S}_{nm}\} = \frac{(1+k_n')a^2}{(2n+1)M_E} \int_\Omega \Delta\sigma(\theta,\lambda)\bar{P}_{nm}(\cos\theta) \times \{\cos m\lambda, \sin m\lambda\} d\Omega \qquad 5\text{-}2$$

where a is the mean radius of the Earth, M_E is the mass of the Earth, (θ,λ) are the co-latitude and east longitude respectively, k_n' is the load Love number of degree n, $\Delta\sigma(\theta,\lambda)$ is the distribution of surface mass load, $\bar{P}_{nm}$ is the normalized associated Legendre function, $d\Omega = \sin\theta d\theta d\lambda$.

From (5-1) and (5-2), we have

$$\Delta J_2 = -\frac{(1+k_2')a^2}{\sqrt{5}M_E} \int_\Omega \Delta\sigma(\theta,\lambda)\bar{P}_2(\cos\theta) d\Omega \qquad\qquad 5\text{-}3$$

This is the equation we could use to compute the contribution to J_2 and rate of J_2 from the given surface mass load and its change respectively. Contrary to

5.2.2 Sea-Level Fingerprint

In order to evaluate the contribution of mass loss from a specific region to J_2 change, we need to take into account of the pattern of mass redistribution. Assumption is made that the water from melted glacier or ice sheets will fill into the ocean. The water will not be uniformly distributed over the ocean, and the pattern of this redistribution of water could be obtained using sea-level fingerprint method that described in Chapter 2.

Figure 5.3 shows that the sea-level fingerprint calculated from melted glaciers and ice sheets from Greenland. The areas near the mass loss will meet a sea-level fall due to the loss of gravitational force generated by the existed mass, and the far-field of the ocean have a sea-level rise more than the average.

Through this sea-level fingerprint approach, we have obtained the unique pattern of the mass redistribution due to mass changes from each specific region. In order to obtain its contribution to J_2, spherical harmonic decomposition is needed.

5.2.3 Sensitivity Kernel

In the sensitivity kernel test of surface water redistribution, we assume 1 Gigaton/yr mass loss from each region in a uniform distribution, and using the sea-level fingerprint method to calculate the pattern of the water distribution over ocean. Thus, we have the surface density distribution as the input of equation (5-3), then the spherical harmonic decomposition is conducted, in the end we have the sensitivity test of the contribution to J_2 from each potential mass loss region.
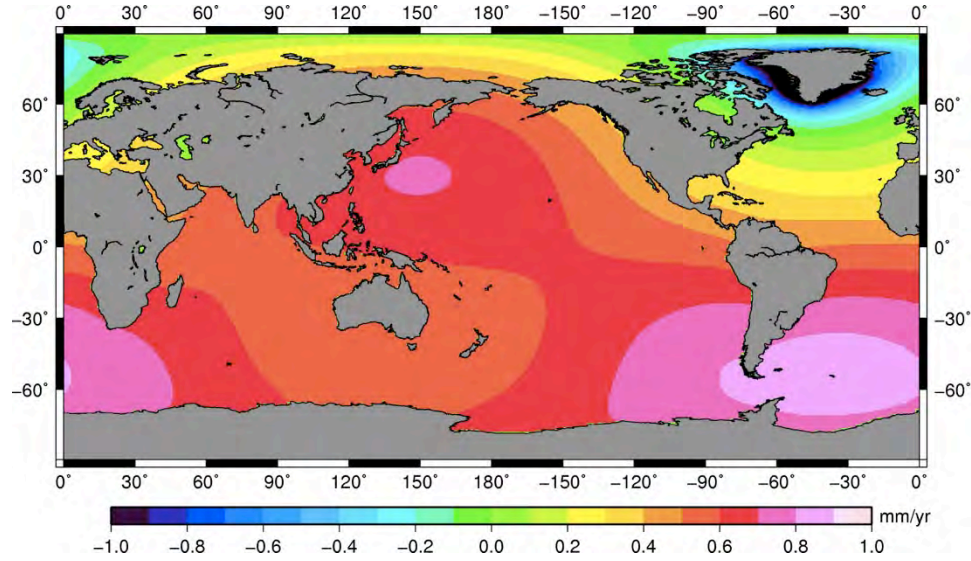
Figure 5.3 Sea level fingerpirnt from Greenland ice melting.

5.3 Data Analysis

5.3.1 SLR-derived J_2

Two types of SLR-derived J_2 time series are used in this study. The first one is long-term monthly estimate (January 1976 to December 2009) that is publicly available, each estimate and its variation is relative to TEG4 reference value (1.082626270618E-3) and determined from laser ranging observation up to 8 satellites: Starlette, Ajisai, Stella, LAGEOS 1 and 2, Etalon-1 and -2, and Beacon Explore-C (BE-C). The processing details can be found in *Cheng and Tapley* [2004].

The second one is provided as the **TN-07-C20-SLR** product updated with GRACE monthly solution, and it is suggested to use them to replace the C_{20} terms in GRACE monthly gravity field. These estimates use the consistent background models with GRACE Level-2 data product including the same Atmosphere-Ocean De-aliasing product, and are obtained from the analysis of SLR data from 5 geodetic satellites: LAGEOS-1 and 2, Starlette, Stella and Ajisai.

The power spectrums are plotted in Figure 5.4 and Figure 5.5. It was shown that in the spectral domain, GFZ ΔJ_2 are more similar with SLR-derived ΔJ_2 than that from CSR and JPL. From the power spectrum of long-term time series, it is obvious that annual signal is dominant.

In the GRACE RL04 data product, C_{20} time series show a significant 161-day aliasing signal from the S_2 tides errors [*Knudsen*, 2003], but in the GRACE RL05 data product, this problem is reduced along with more accurate background model.
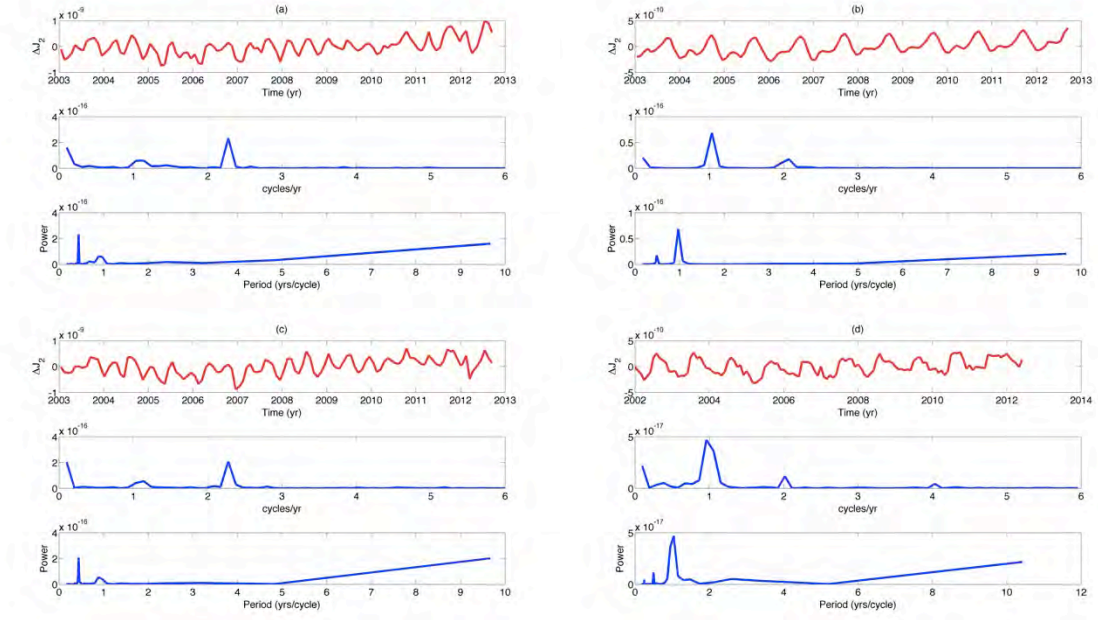
64

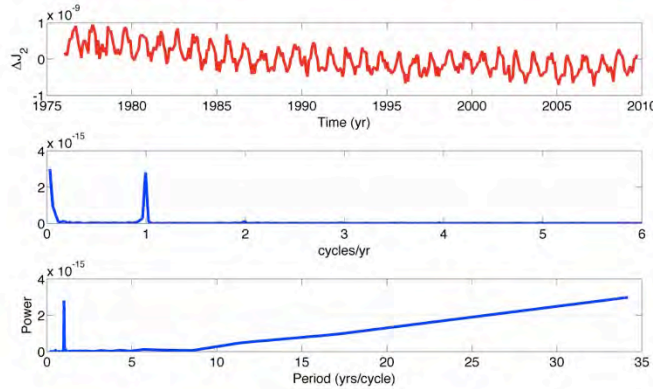Figure 5.4 Power spectrum of ΔJ_2 extracted from GRACE and SLR. (a) CSR; (b) GFZ; (c) JPL, (d) SLR.

Figure 5.5 Power spectrum of ΔJ_2 extracted from long term SLR records.

5.3.2 GRACE

In this study, GRACE Level-2 RL05 data products from three data centers (CSR, GFZ and JPL) spanning from January 2003 to December 2011 are used to estimate the time series of surface mass change and also its trend following the procedure of *Wahr et al.* [1998]. An averaged model from all the monthly solution as the referenced field is subtracted from each monthly filed. Then GIA correction is applied to the residual coefficients. Thus, the residual coefficients are converted to the surface mass change assuming the surface mass changes happening in a thin layer of the Earth surface. De-correlation procedure according to *Duan et al.* [2009] is also applied to reduce the 'stripe' effect. Smoothing and leakage reduction are then applied according to *Guo et al.* [2010].

5.4 Result and Interpretation

65

5.4.1 Comparison between SLR-derived J_2 and GRACE Observed J_2

Figure 5.6 shows the comparison between SLR-derived C_{20} and that extracted from the GRACE monthly data product. Time series of C_{20} from CSR and JPL are similar to each other; time series of C_{20} from GFZ is similar to SLR-derived values. Figure 5.7 shows the comparison between SLR-derived J_2 and that extracted from GRACE monthly product.
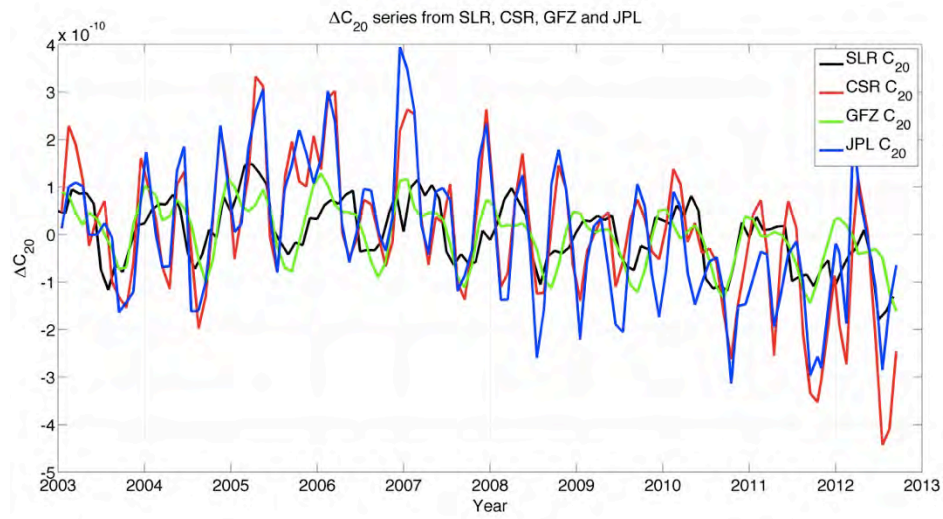

Figure 5.6 Comparison of time series of ΔC_{20} between SLR (TN-07), CSR (RL05), GFZ (RL05) and JPL (RL05).
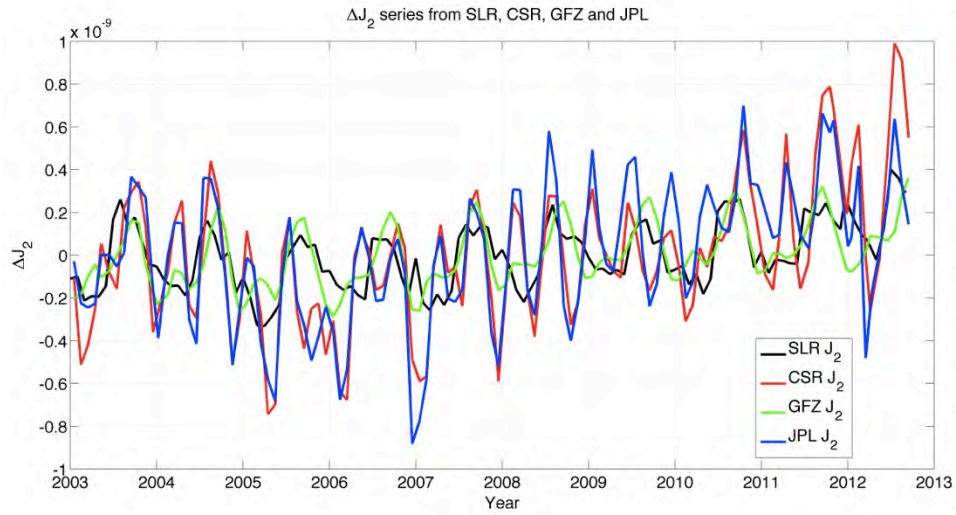

Figure 5.7 Comparison of time series of ΔJ_2 between SLR (TN-07), CSR (RL05), GFZ (RL05) and JPL (RL05).

66

Table 5.1 Sensitivity test of geocenter motion and J_2 change induced by 1 Gton/yr mass change from different regions.

Area	ΔZ (mm/yr)	ΔX(mm/yr)	ΔY(mm/yr)	ΔJ_2 (yr^{-1})
Alaska	0.0013	−0.0003	−0.0003	−7.20E-14
Antarctica	−0.0013	0.0002	0.0002	−1.18E-13
Canadian Arctic Archipelago	0.0014	0.0003	−0.0002	−1.03E-13
Greenland	0.0016	0.0005	−0.0002	−1.14E-13
Asian High Mountain	0.0010	0.0003	0.0012	−7.99E-15
Iceland	0.0016	0.0008	−0.0001	−1.01E-13
Patagonia	−0.0010	0.0005	−0.0009	−4.81E-14
Svalbard	0.0016	0.0004	0.0001	−1.24E-13

5.4.2 Sensitivity Test

The sensitivity test was conducted for several large land ice regions including Antarctic, Greenland, Alaska, Patagonia, Asian High Mountain, Canadian Arctic Archipelago, Svalbard Island and Iceland.

It consists of the major ice sheets and also the largest mountain glaciers and ice caps. Figure 5.8 provides the data coverage of global mountain glaciers/ice caps, and ice sheets used in this sensitivity test.

Table 5.1 summarizes the result of this sensitivity test. The sensitivity test shows that the higher latitude and larger area makes the more sensitive contribution of the surface mass change to J_2. It is more sensitive of mass loss from ice sources located at more extreme latitudes, including Antarctica, Greenland, Canadian Arctic Archipelago, Svalbard Island, Iceland than for example, the mass loss from Asian High Mountain glacier systems. That is because J_2 is proportional to degree 2 Legendre functions. Figure 5.9 shows the degree 2 Legendre functions, the nodal lines of J_2 are $\pm 35.3°$ latitude. In addition to J_2, we have shows the mass changes contributions to degree 1 terms (geocenter motion, see Equation (6-5) for the relations)

Previous study commonly assumes the uniform melting scenario from each region and also the water will be uniformly distributed over ocean [*Cheng et al.*, 2013; *Nerem and Wahr*, 2011]. We have also tested the effect of melting pattern from each region, namely, the uniform pattern or the pattern inferred from GRACE. From our study, uniform melting assumption, which is commonly adopted by previous studies does not cause much difference for regions like Antarctica and Greenland (less than 4%), but for regions like Alaska and Canadian Arctic Archipelago, it causes differences up to 15%. In addition, we have also tested the spatial variation of the water distributed over the ocean (uniform and pattern computed using sea-level fingerprint method). Results show that the difference is up to 8% for those regions. In the sensitivity test here, we just simply adopt the uniform melting assumption but using the sea-level fingerprint method to calculate the pattern of water redistribution over the ocean. In the final result, we use the melting pattern that is inferred from GRACE as input and the sea-level fingerprint method to

calculate the water redistribution. Together with the land ice mass loss and the resulting water redistribution over the ocean, we derived and interpreted the changes in the Earth's oblateness due to different combinations of polar ice sheet and mountain glacier melt. Here the GIA component of J_2 is assumed known from model prediction.
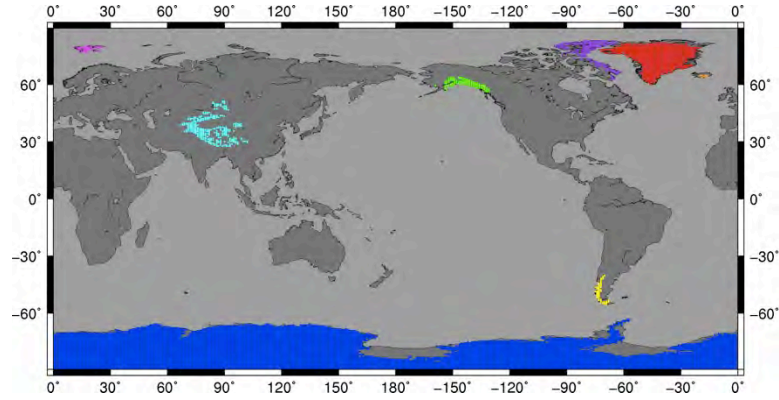

Figure 5.8 Coverage of the selected mountain glacier system and ice caps (Alaska, Patagonia, Asian High Mountain, Canadian Arctic Archipelago, Svalbard Island, Iceland) and Antarctic and Greenland ice sheets.
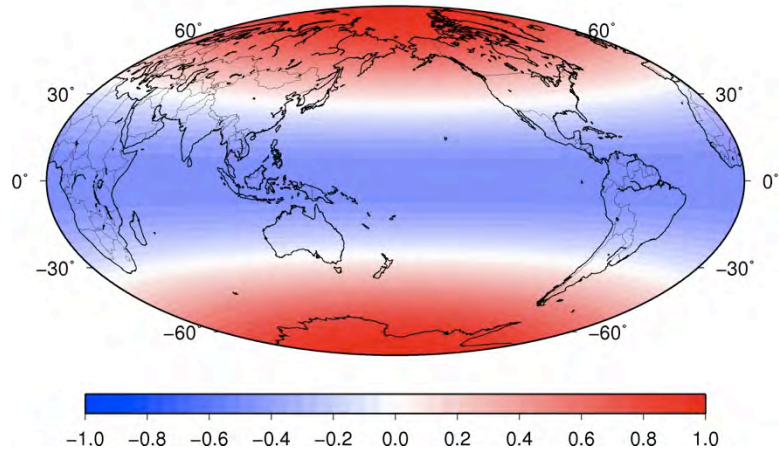
Figure 5.9 Degree 2 Legendre functions projected to the real Earth. The maximum value is 1.0 happening in the South and North Pole, and the minimum value is –0.5 in the equator.
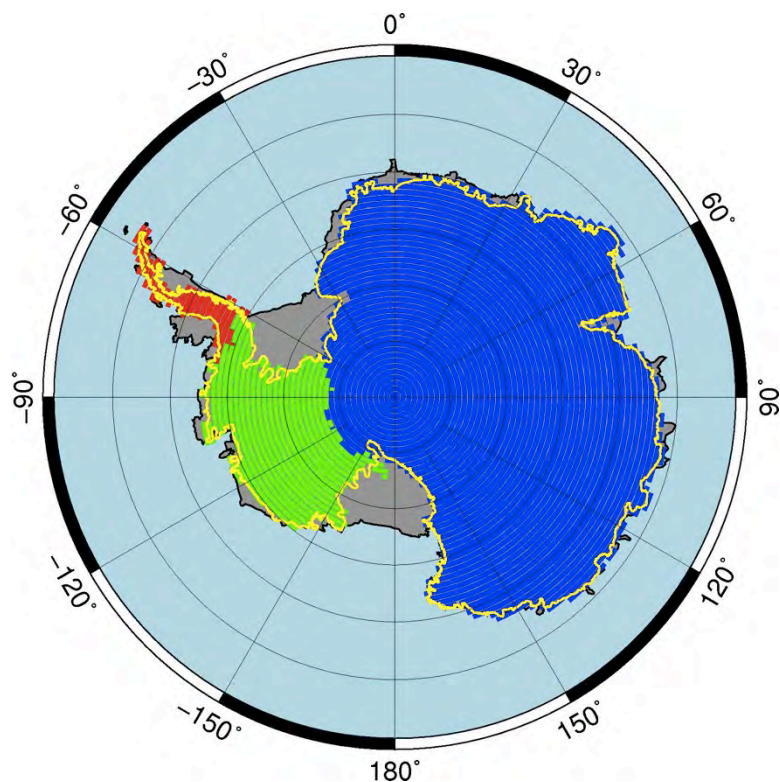
Figure 5.10 Red: Antarctica Peninsula; Green: West Antarctica; Blue: East Antarctica; Yellow: ground line. (Data: [*Zwally et al.*, 2012])
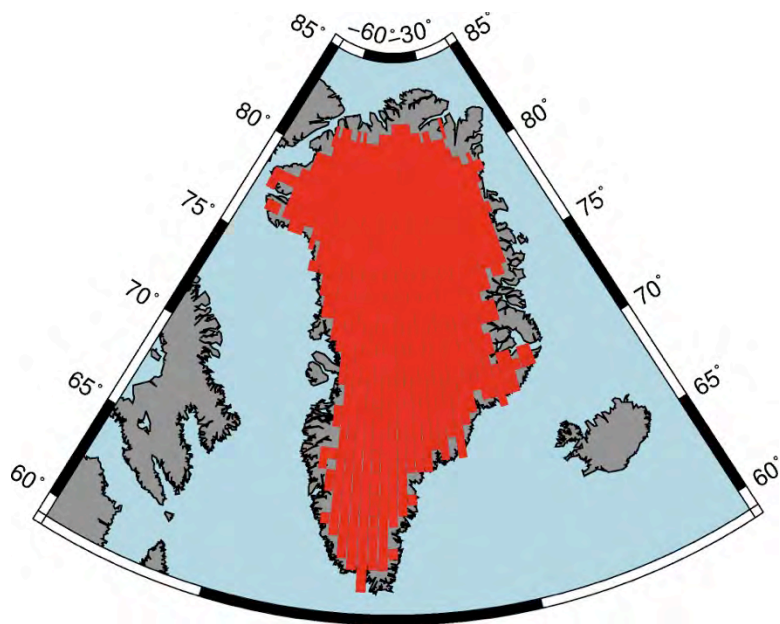

Figure 5.11 Red: Greenland mask. (Data: [*Zwally et al.*, 2012])

5.4.3 Contribution to J_2 from Surface Mass Change

Figure 5.12 shows the surface mass change trend extracted from 108 months GRACE Level-2 RL05 gravity field (January 2003 to December 2011) for CSR, GFZ and JPL respectively.

From the geographical plot, it is obvious that the present-day mass change happens in high latitude region, such as Antarctica, Greenland, Canadian Arctic Archipelago, Alaska and Patagonia. From the sensitivity test, changes in Earth's oblateness are more sensitive to the mass redistribution from high latitude regions.

From Table 5.2 to Table 5.4 the results of the contribution to J_2 and geocenter motion due to the ice mass loss from Earth's ice reservoirs estimated using GRACE data products from CSR, GFZ, and JPL are summarized respectively. It is obvious that mass loss from Antarctica and Greenland are the major contributors to J_2 and geocenter changes. Contribution of mass loss from Canadian Arctic Archipelago is larger than that from Alaska glaciers, but smaller than that from Antarctica and Greenland ice sheets. The estimate is similar to the results the published by *Jacob et al.* [2012] that is shown in Table 5.5. In previous studies, regions like Alaska and Canadian Arctic Archipelago have been neglected [*Cheng et al.*, 2013; *Nerem and Wahr*, 2011]. However, this study shows that these regions should not be neglected, and one should take these two regions into account when interpreting the changes in the Earth's oblateness induced by the recent ice mass changes. It is noted that the GIA model used in GRACE data processing is the Paulson model (Table 5.2 to Table 5.5).

Table 5.6 presents an updated estimate of GRACE observed ice reservoirs and the corresponding contributions to J_2 and geocenter motion trends. CSR RL05 data product is used. In particular, the GIA model used for GRACE data is the Paulson model, except Antarctica, which the Whitehouse GIA model [*Whitehouse et al.*, 2012] is used, resulting in a significant different Antarctic mass balance estimate [*King et al.*, 2012] from the estimates presented in Table 5.2 and Table 5.5. We also use an updated estimate for the Asian High Mountain glacier system by Jianbin Duan [*Pers. Comm.*], which is almost 8 times larger than the estimate published by *Jacob et al.* [2012]. However, as indicated before, because of the locations of Antarctica and the Asian High Mountain glaciers, only Antarctica provides a change in the predicted J_2 and degree one terms changes.
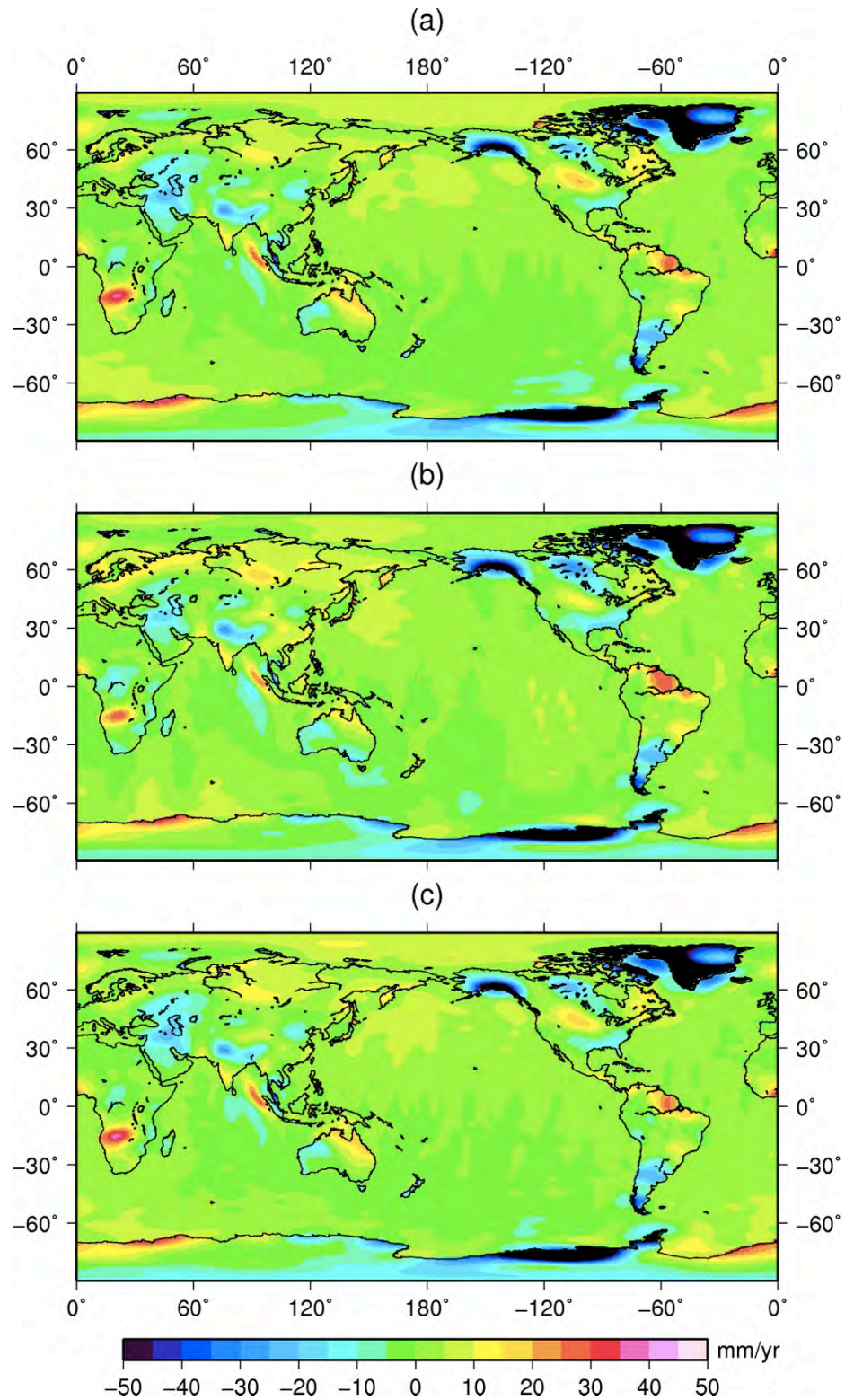
Figure 5.12 Surface mass density trend from 108 GRACE RL05 monthly solutions (January 2003 to December 2011). (a) CSR; (b) GFZ; (c) JPL.

Table 5.2 Contribution to J_2 and also geocenter motion due to mass loss from Earth's ice reservoirs. Paulson GIA model used. The mass loss estimates are computed from GRACE CSR RL05.

	Mass change (Gton/yr)	ΔZ (mm/yr)	ΔX (mm/yr)	ΔY (mm/yr)	ΔJ_2 (yr^{-1})	ΔJ_2 Percentage
Alaska	−20	−0.03	0.01	0.01	1.44E-12	3.65%
Antarctica	−137	0.18	−0.02	−0.03	1.62E-11	41.16%
Canadian Arctic Archipelago	−28	−0.04	−0.01	0.01	2.88E-12	7.33%
Greenland	−158	−0.25	−0.08	0.04	1.80E-11	45.71%
Asian High Mountain	−6	−0.01	0.00	−0.01	4.41E-14	0.11%
Iceland	−2	0.00	0.00	0.00	2.21E-13	0.56%
Patagonia	−7	0.01	0.00	0.01	3.31E-13	0.84%
Svalbard	−2	0.00	0.00	0.00	2.45E-13	0.62%
Total	**−359**	**−0.14**	**−0.11**	**0.02**	**3.93E-11**	**100.00%**

Table 5.3 Contribution to J_2 and also geocenter motion due to mass loss from Earth's ice reservoirs. The mass loss estimates are computed from GRACE GFZ RL05.

	Mass change (Gton/yr)	ΔZ (mm/yr)	ΔX (mm/yr)	ΔY (mm/yr)	ΔJ_2 (yr^{-1})	ΔJ_2 Percentage
Alaska	−23	−0.03	0.01	0.01	1.64E-12	4.22%
Antarctica	−131	0.17	−0.02	−0.03	1.55E-11	39.73%
Canadian Arctic Archipelago	−28	−0.04	−0.01	0.01	2.95E-12	7.56%
Greenland	−159	−0.25	−0.08	0.04	1.81E-11	46.49%
Asian High Mountain	−5	0.00	0.00	−0.01	4.02E-14	0.10%
Iceland	−2	0.00	0.00	0.00	1.80E-13	0.46%
Patagonia	−7	0.01	0.00	0.01	3.27E-13	0.84%
Svalbard	−2	0.00	0.00	0.00	2.31E-13	0.59%
Total	**−357**	**−0.16**	**−0.11**	**0.02**	**3.90E-11**	**100.00%**

Table 5.4 Contribution to J_2 and also geocenter motion due to mass loss from Earth's ice reservoirs. The mass loss estimates are computed from GRACE JPL RL05.

	Mass change (Gton/yr)	ΔZ (mm/yr)	ΔX (mm/yr)	ΔY (mm/yr)	ΔJ_2 (yr^{-1})	ΔJ_2 Percentage
Alaska	−20	−0.03	0.01	0.01	1.45E-12	3.62%
Antarctica	−145	0.19	−0.03	−0.03	1.71E-11	42.82%
Canadian Arctic Archipelago	−27	−0.04	−0.01	0.01	2.78E-12	6.95%
Greenland	−156	−0.25	−0.08	0.03	1.77E-11	44.28%
Asian High Mountain	−3	0.00	0.00	0.00	2.64E-14	0.07%
Iceland	−2	0.00	0.00	0.00	1.97E-13	0.49%
Patagonia	−6	0.01	0.00	0.01	2.99E-13	0.75%
Svalbard	−3	−0.01	0.00	0.00	4.09E-13	1.02%
Total	**−363**	**−0.13**	**−0.11**	**0.02**	**4.00E-11**	**100.00%**

Table 5.5 Contribution to J_2 and also geocenter motion due to mass loss from Earth's ice reservoirs. Paulson GIA model used. The mass loss estimates are from *Jacob et al.* [2012].

	Mass change (Gton/yr)	ΔZ (mm/yr)	ΔX (mm/yr)	ΔY (mm/yr)	ΔJ_2 (yr^{-1})	ΔJ_2 Percentage
Alaska	−46	−0.06	0.02	0.01	3.31E-12	5.8%
Antarctica	−165	0.21	−0.03	−0.04	1.95E-11	34.0%
Canadian Arctic Archipelago	−67	−0.10	−0.02	0.02	6.93E-12	12.1%
Greenland	−222	−0.35	−0.11	0.05	2.53E-11	44.1%
Asian High Mountain	−4	0.00	0.00	0.00	3.20E-14	0.1%
Iceland	−11	−0.02	−0.01	0.00	1.11E-12	1.9%
Patagonia	−23	0.02	−0.01	0.02	1.11E-12	1.9%
Svalbard	−3	0.00	0.00	0.00	3.72E-13	0.7%
Total	**−541**	**−0.29**	**−0.16**	**0.06**	**5.72E-11**	**100.0%**

Table 5.6 Contribution to J_2 and also geocenter motion due to mass loss from Earth's ice reservoirs. Paulson GIA model used except for Antarctica[*], which used the Whitehouse GIA model [*Whitehouse et al.*, 2012]. [**]Revised estimate for Asian High Mountain glaciers [*Jianbin Duan, Person. Com.*]. The mass loss estimates are computed from GRACE CSR RL05.

	Mass change (Gton/yr)	ΔZ (mm/yr)	ΔX (mm/yr)	ΔY (mm/yr)	ΔJ_2 (yr^{-1})	ΔJ_2 Percentage
Alaska	−20	−0.03	0.01	0.01	1.44E-12	4.72%
Antarctica[*]	−60	0.08	−0.01	−0.01	7.08E-12	23.29%
Canadian Arctic Archipelago	−28	−0.04	−0.01	0.01	2.88E-12	9.48%
Greenland	−158	−0.25	−0.08	0.04	1.80E-11	59.07%
Asian High Mountain	−31	−0.03	−0.01	−0.04	2.48E-13	0.81%
Iceland	−2	0.00	0.00	0.00	2.21E-13	0.73%
Patagonia	−7	0.01	0.00	0.01	3.31E-13	1.09%
Svalbard	−2	0.00	0.00	0.00	2.45E-13	0.81%
Total	**−308**	**−0.27**	**−0.10**	**0.00**	**3.04E-11**	**100.00%**

5.4.4   Latitude Average

In order to identify the contributions to J_2, we compute the latitude averaged contribution to J_2 and plot it along with time. Four cases are provided here (1) No GIA correction, No C_{20} replacement; (2) No GIA correction, C_{20} replaced by SLR-derived value; (3) Paulson GIA model applied, no C_{20} replacement; (4) Paulson GIA model applied, C_{20} replaced by SLR-derived values.

Figure 5.13 to Figure 5.15 show the latitude average mass changes that extracted from GRACE monthly solution relative to a reference field (in this case, the reference field is chosen to be the average of all the monthly solutions, the time epoch is half of 2007). It provides the time evolution of surface mass changes in latitude-time perspective. From the plots, one could easily tell that mass change happens in high latitude, this is consistent with the trend map shown as Figure 5.12.

Figure 5.16 to Figure 5.18 show the contributions to J_2 from the surface mass changes. One also could easily tell that the major contribution to the increase in J_2 comes from the mass redistribution from higher latitude to the lower latitude.

To make this more clearly, the profiles of the mass changes and also their contributions to J_2 are plotted along the latitude. These plots are shown from Figure 5.19 and Figure 5.20. Same conclusions can be made from these plots. In addition, the dominant effect of GIA in the estimated mass changes from Antarctica become more obvious.
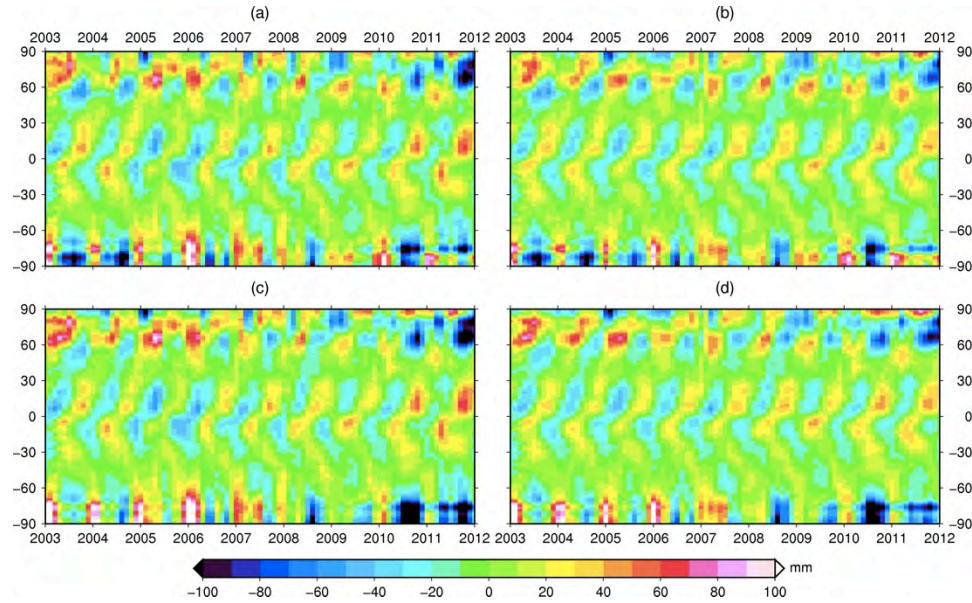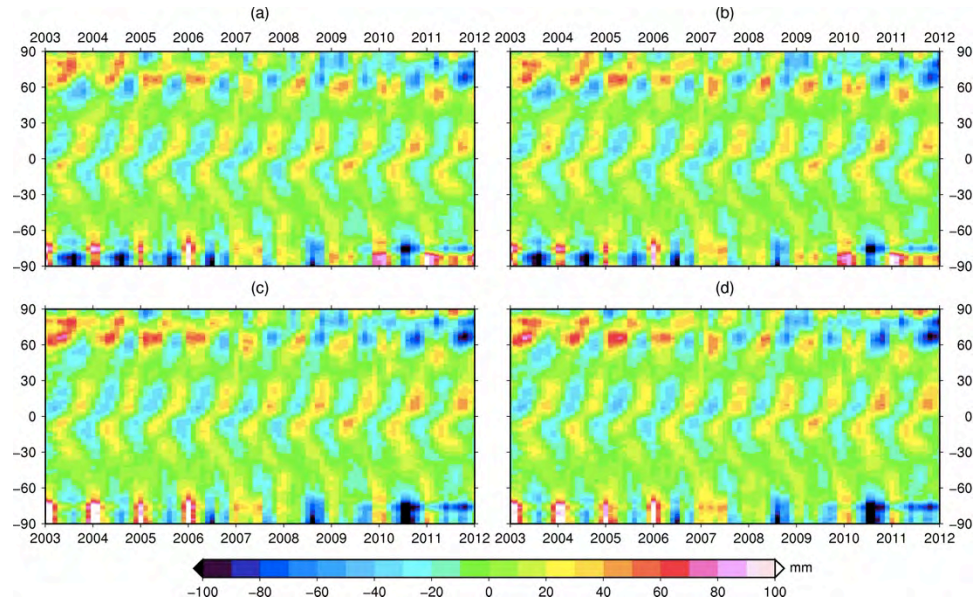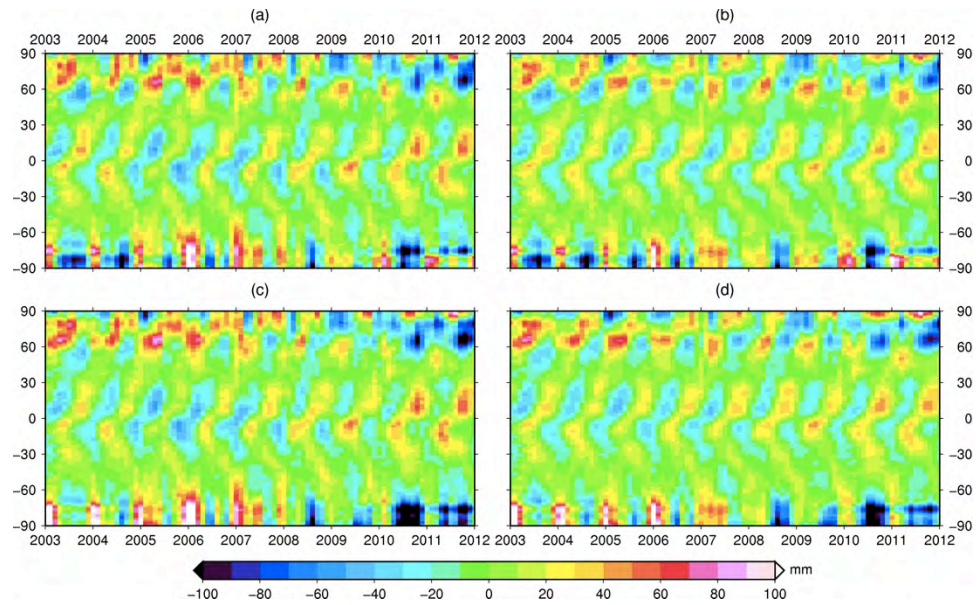

Figure 5.13 Latitude average of mass change computed from CSR RL05. Decorrelation and 350 km Gaussian smoothing is applied. (a) No GIA correction, No C_{20} replacement; (b) No GIA correction, C_{20} replaced by SLR-derived value; (c) Paulson GIA model applied, no C_{20} replacement; (d) Paulson GIA model applied, C_{20} replaced by SLR-derived values.
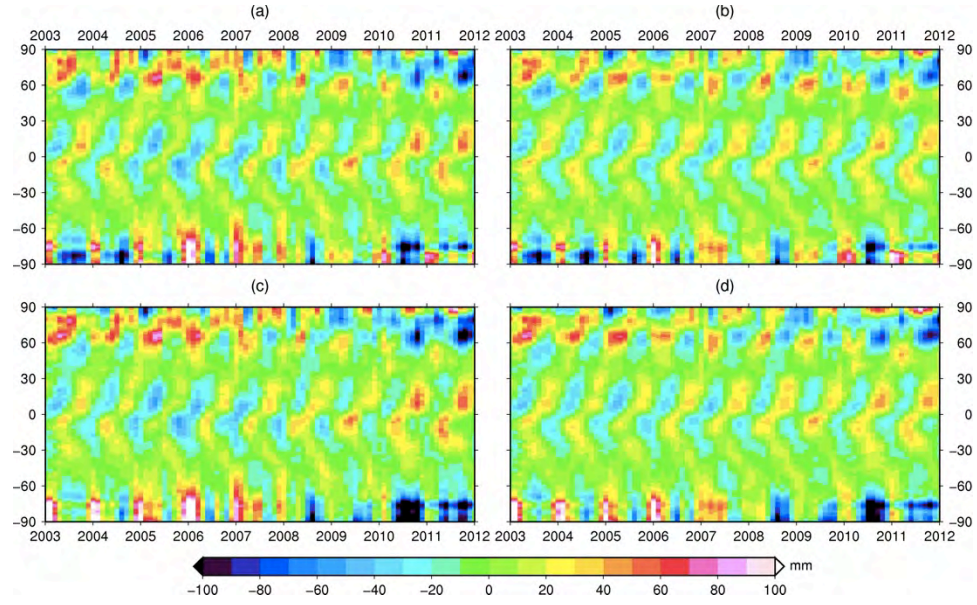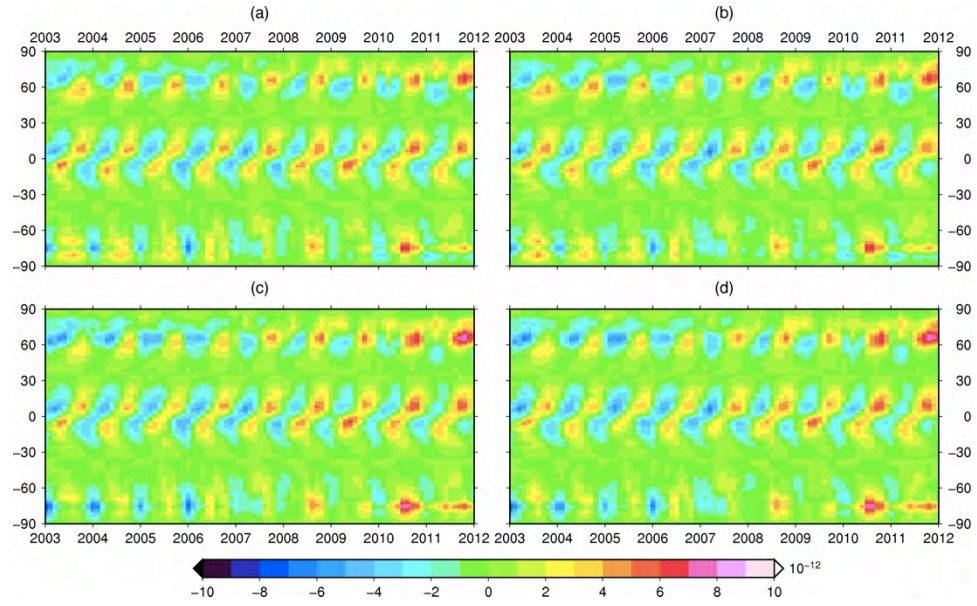
Figure 5.14 Latitude average of mass change computed from GFZ RL05 Decorrelation and 350 km Gaussian smoothing is applied. (a) No GIA correction, No C_{20} replacement; (b) No GIA correction, C_{20} replaced by SLR-derived value; (c) Paulson GIA model applied, no C_{20} replacement; (d) Paulson GIA model applied, C_{20} replaced by SLR-derived values.
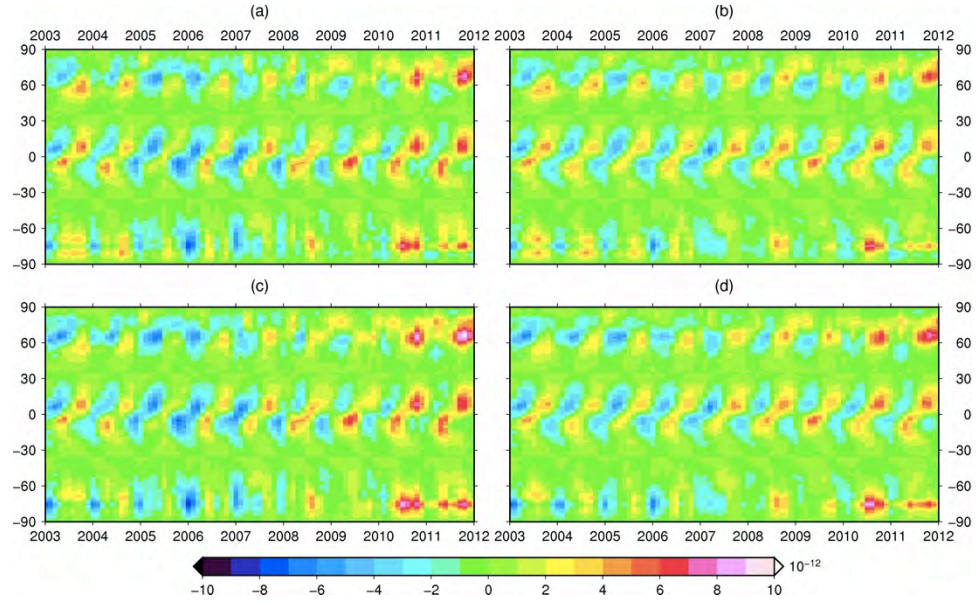

Figure 5.15 Latitude average of mass change computed from JPL RL05 Decorrelation and 350 km Gaussian smoothing is applied. (a) No GIA correction, No C_{20} replacement; (b) No GIA correction, C_{20} replaced by SLR-derived value; (c) Paulson GIA model applied, no C_{20} replacement; (d) Paulson GIA model applied, C_{20} replaced by SLR-derived values.

75

Figure 5.16 Latitude average of mass change contribution to J_2 change from CSR RL05 Decorrelation and 350 km Gaussian smoothing is applied. (a) No GIA correction, No C_{20} replacement; (b) No GIA correction, C_{20} replaced by SLR-derived value; (c) Paulson GIA model applied, no C_{20} replacement; (d) Paulson GIA model applied, C_{20} replaced by SLR-derived values.
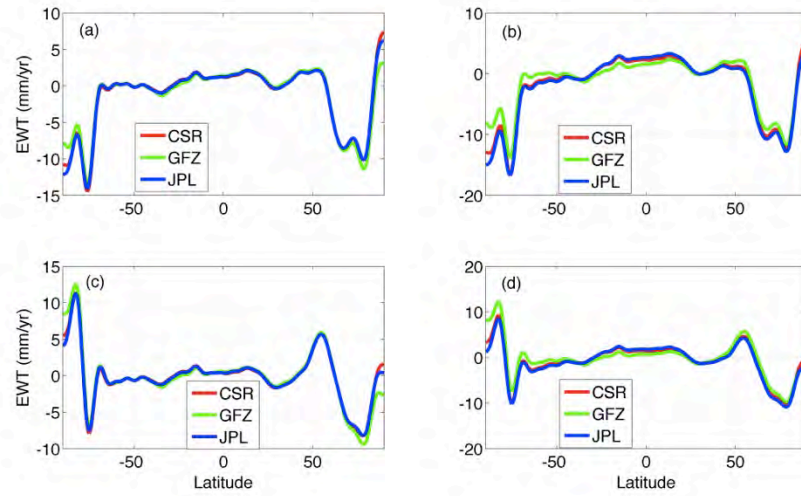

Figure 5.17 Latitude average of mass change contribution to J_2 change from GFZ RL05 Decorrelation and 350 km Gaussian smoothing is applied. (a) No GIA correction, No C_{20} replacement; (b) No GIA correction, C_{20} replaced by SLR-derived value; (c) Paulson GIA model applied, no C_{20} replacement; (d) Paulson GIA model applied, C_{20} replaced by SLR-derived values.
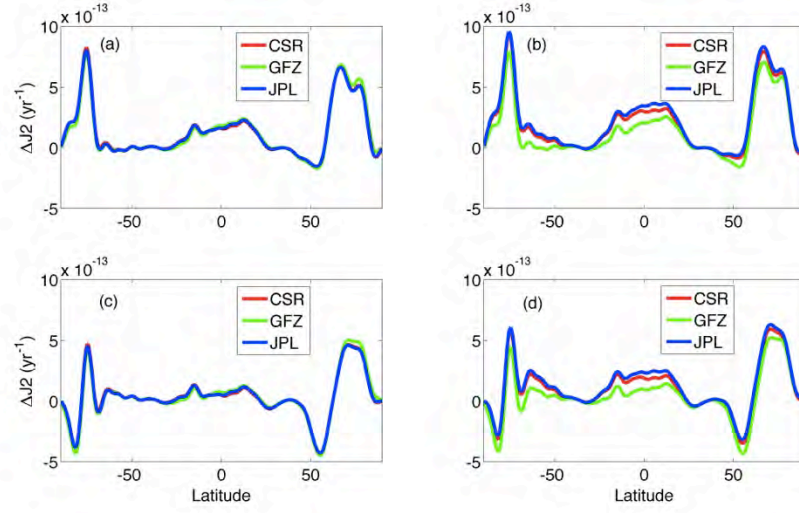
Figure 5.18 Latitude average of mass change contribution to J_2 change from JPL RL05. Decorrelation and 350 km Gaussian smoothing is applied. (a) No GIA correction, No C_{20} replacement; (b) No GIA correction, C_{20} replaced by SLR-derived value; (c) Paulson GIA model applied, no C_{20} replacement; (d) Paulson GIA model applied, C_{20} replaced by SLR-derived values.

Figure 5.19 Latitude average profile of mass change extracted from GRACE RL05 (Red: CSR; Green: GFZ; Blue: JPL). Decorrelation and 350 km Gaussian smoothing is applied. (a) No GIA correction, No C_{20} replacement; (b) No GIA correction, C_{20} replaced by SLR-derived value; (c) Paulson GIA model applied, no C_{20} replacement; (d) Paulson GIA model applied, C_{20} replaced by SLR-derived values.

Figure 5.20 Latitude average profile of mass change contribution to J_2 change from GRACE RL05 (Red: CSR; Green: GFZ; Blue: JPL). Decorrelation and 350 km Gaussian smoothing is applied. (a) No GIA correction, No C_{20} replacement; (b) No GIA correction, C_{20} replaced by SLR-derived value; (c) Paulson GIA model applied, no C_{20} replacement; (d) Paulson GIA model applied, C_{20} replaced by SLR-derived values.

5.4.5　Time Series of J_2

Figure 5.21 shows the time series of J_2 derived from SLR and extracted from GRACE. Left column are those without removing GIA contribution, the right column are those with Paulson GIA model J_2 (−3.6E-11) removed. From the four time series, red line indicates the annual smoothing form the monthly values that in blue color. It seems one turning point exists around the late 2005. It could also be seen in the long-term time series of J_2 as in Figure 5.1.

In order to explain the causes of this turning point, the time series of J_2 extracted from GAC product and also the GAC+GSM are plotted in Figure 5.22 and Figure 5.23.
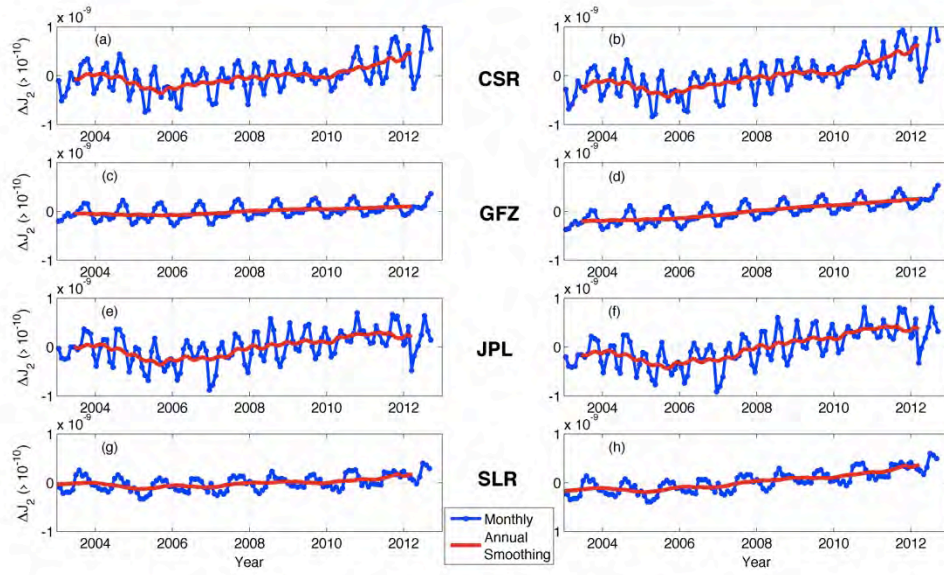
Figure 5.21 Time series of ΔJ_2 extracted from GRACE RL05 and SLR. Left: Before GIA correction; Right: After removing Paulson GIA model. From top to bottom: CSR, GFZ, JPL and SLR.
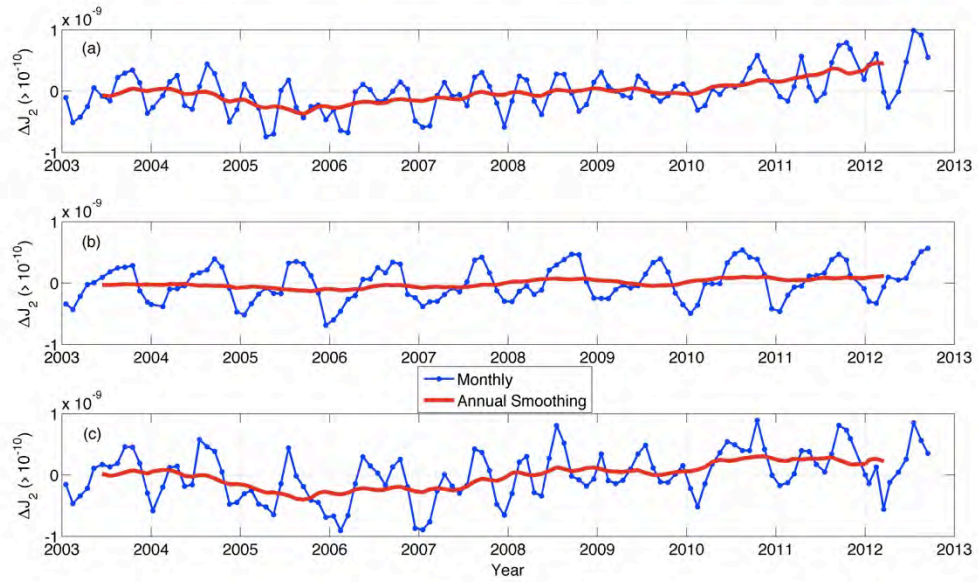

Figure 5.22 Time series of ΔJ_2 extracted from GRACE RL05 (GAC only). (a) CSR; (b) GFZ; (c) JPL.
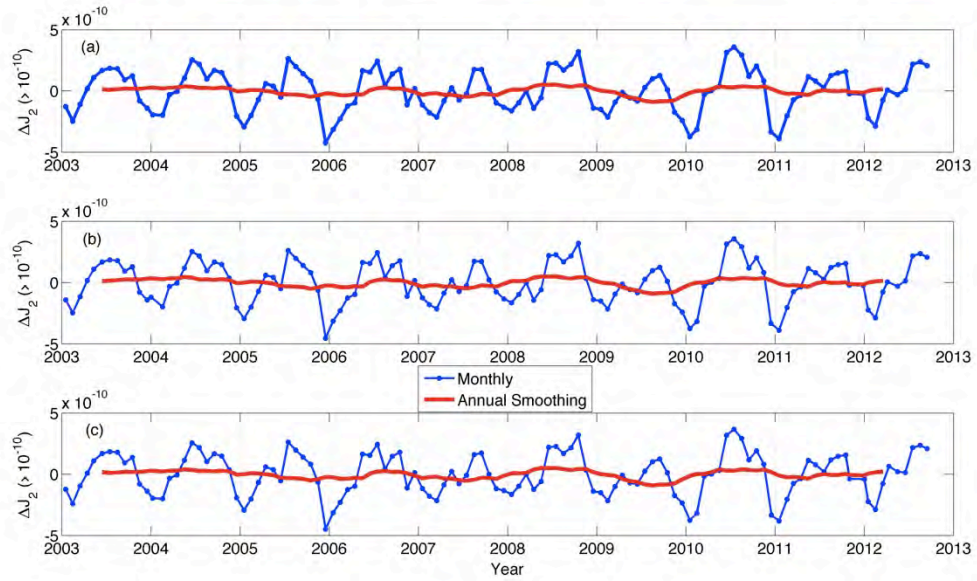
Figure 5.23 Time series of ΔJ_2 extracted from GRACE RL05 (GSM + GAC). (a) CSR; (b) GFZ; (c) JPL.

5.4.6 GIA Effect

From Chapter 3, we have already known that the choice of GIA model to be used in the GRACE processing may cause significant difference in the result. Here, we only applied the Paulson et al. [2007] GIA model, which is updated by Geruo A in 2011, provided by John Wahr (*Pers. Com.*). For the specific region, such as Antarctica, Paulson model may not be the best choice [Table 5.6], the Whitehouse model (W12A) published by *Whitehouse et al.* [2012] has shown to produce significant difference in the Antarctica mass balance estimates [*King et al.*, 2012]. However, our conclusion about J_2 will not change along with different GIA models. Thus, in here, we only choose one model for this purpose. To study the effect of different choice of GIA model, Table 5.7 summarizes different J_2 rate from different GIA models.

5.4.7 Tuning Point

From J_2 time series, one could see that a turning point exists at late 2005 or early 2006.

From the sensitive kernel test, we choose four regions: (1) Antarctica, (2) Greenland, (3) Canadian Arctic Archipelago, and (4) Alaska. Mass changes from those four regions are sensitive to the changes in Earth's oblateness. The estimated mass changes are plotted in time series in Figure 5.24 to Figure 5.27. The averaging areas are plotted in Figure 5.8, Figure 5.10 and Figure 5.11.

Table 5.7 ΔJ_2 from different GIA models.

Model	GIA ΔJ_2 (yr^{-1})
Pau_5_R	–3.6E-11
Pel_4_VM2	–4.2E-11
Pel_5_VM2_R	–3.4E-11
Pel_5_VM2_R_O	–4.0E-11
Pel_5_VM4_R_O	–4.0E-11
SaS_1	–2.2E-11
SaS_3	–5.5E-11
SKM_O_R	–1.5E-11
SVv_3_REF	–5.5E-11
SVv_L_ALT	–1.0E-11
vdW_5	–3.3E-11
vdW_5_R	–3.2E-11
WaO_EGOD	–3.5E-11
WaW_4	–5.2E-11
WaW_5	–5.4E-11
Mean and STD	**–3.7±1.4E-11**
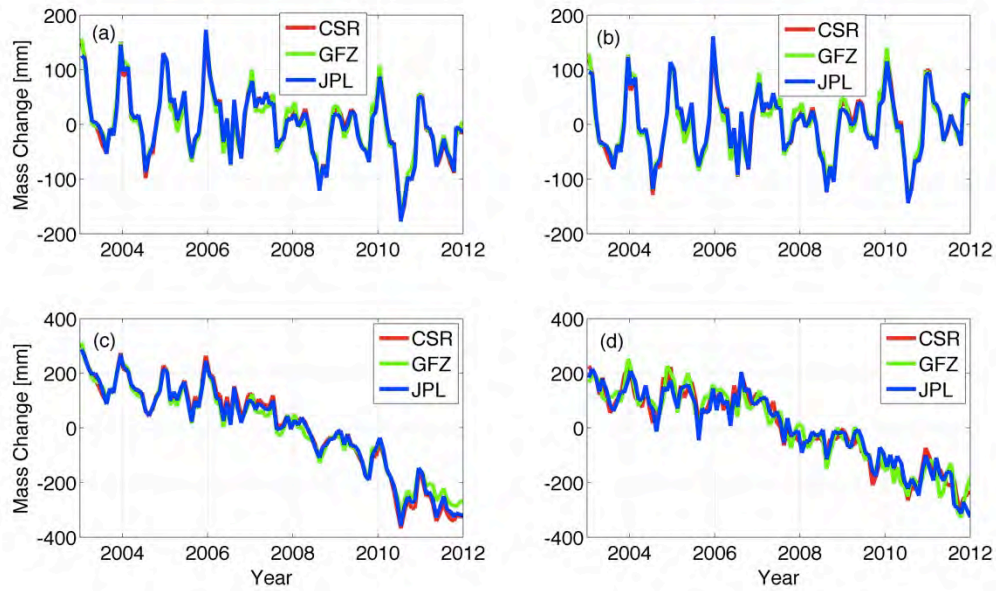
Figure 5.24 Mass change over Antarctica from three data center (SLR C_{20} replaced for CSR and JPL, Paulson GIA applied, 350km Gaussian smoothing. (a) Entire Antarctica; (b) East Antarctica; (c) West Antarctica; (d) Antarctic Peninsula. Red: CSR; Green: GFZ; Blue: JPL.
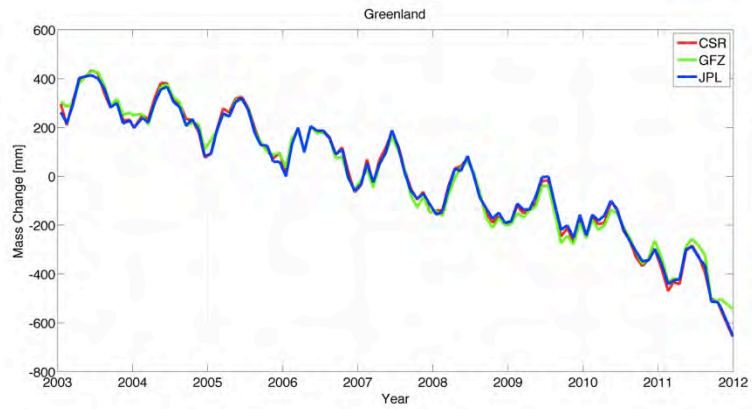
Figure 5.25 Mass change from Greenland from three data center (SLR C_{20} replaced for CSR and JPL, Paulson GIA applied, 350km Gaussian smoothing). Red: CSR; Green: GFZ; Blue: JPL.
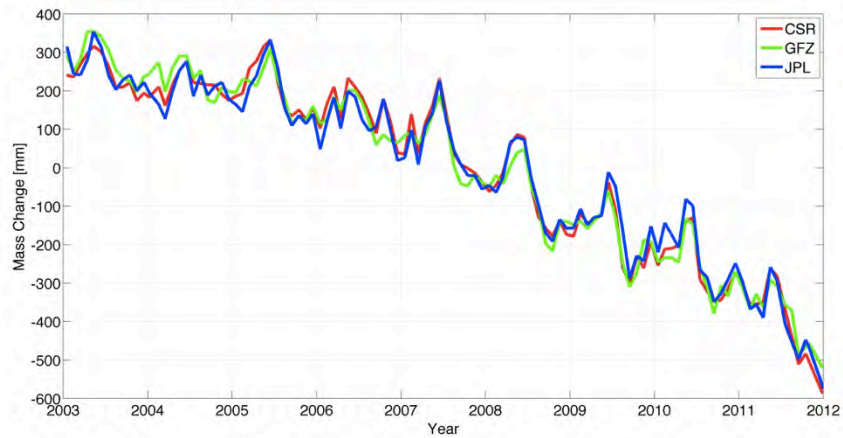

Figure 5.26 Mass change from Canadian Arctic Archipelago from three data center (SLR C_{20} replaced for CSR and JPL, Paulson GIA applied, 350km Gaussian smoothing). Red: CSR; Green: GFZ; Blue: JPL.
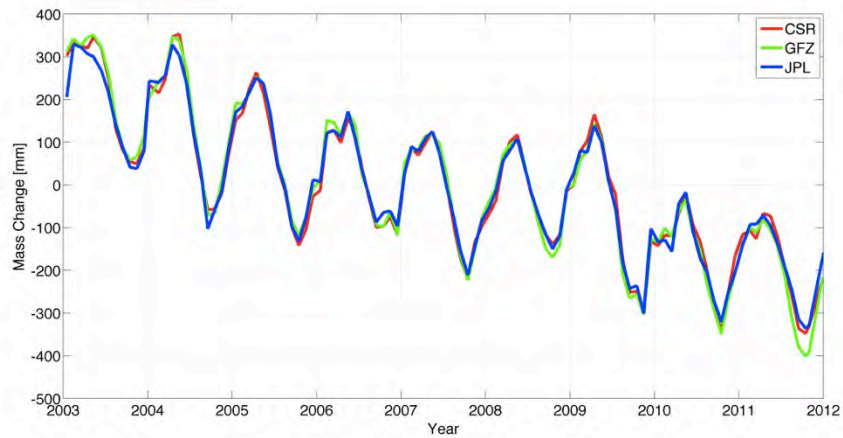

Figure 5.27 Mass change from Alaska from three data center (SLR C_{20} replaced for CSR and JPL, Paulson GIA applied, 350km Gaussian smoothing). Red: CSR; Green: GFZ; Blue: JPL.
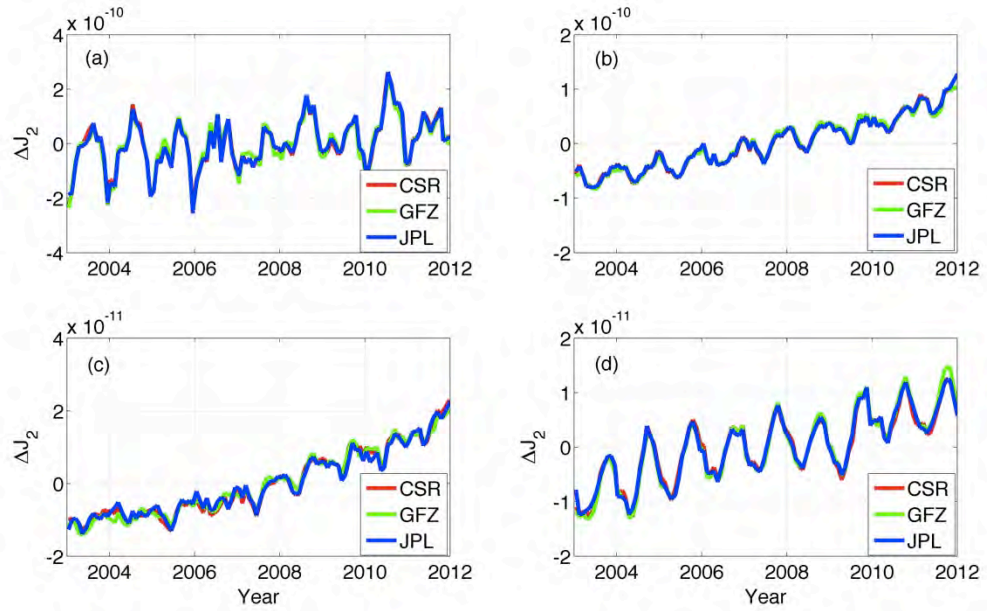
Figure 5.28 Contribution to ΔJ_2 from (a) Antarctica, (b) Greenland, (c) Canadian Arctic Archipelago, and (d) Alaska using data from three data center (SLR C_{20} replaced for CSR and JPL, Paulson GIA applied, 350km Gaussian smoothing). Red: CSR; Green: GFZ; Blue: JPL.
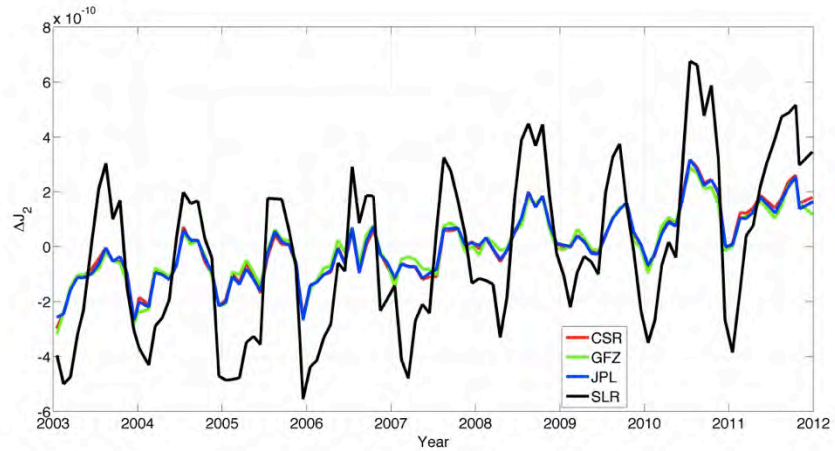

Figure 5.29 Time series of ΔJ_2 extracted from SLR and sum of contributions from four regions (Antarctica, Greenland, Canadian Arctic Archipelago and Alaska), atmosphere is added back. Black: SLR; Red: CSR; Green: GFZ; Blue: JPL.
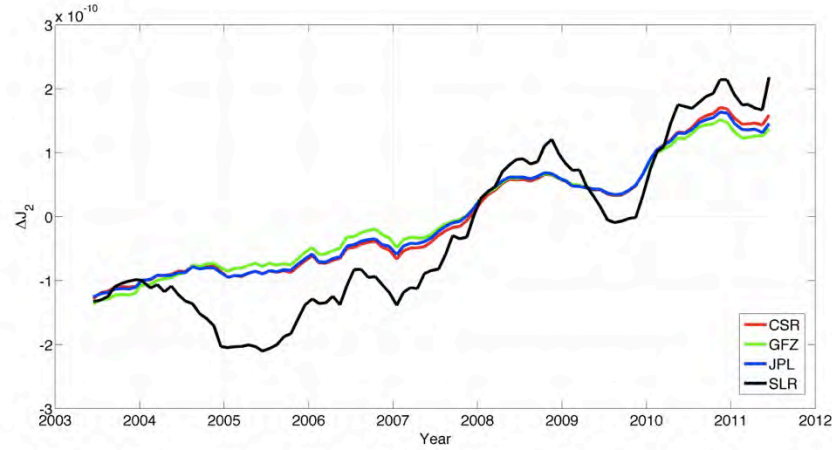
Figure 5.30 Time series of ΔJ_2 extracted from SLR and sum of contributions from four regions (Antarctica, Greenland, Canadian Arctic Archipelago and Alaska), atmosphere is added back. Annual smoothing is applied. Black: SLR; Red: CSR; Green: GFZ; Blue: JPL.

Figure 5.29 and Figure 5.30 show the comparison between the SLR-derived J_2 time series and the contributions of mass loss from four regions (Antarctica, Greenland, Canadian Arctic Archipelago and Alaska) after remove GIA (here Paulson GIA model is applied). It also shows that turning point exists around 2006, which indicates that something changed at that time.

In Figure 5.29, the seasonal signals in SLR-derived J_2 have larger amplitude than the contribution from four study regions. When taking annual smoothing, one could see in Figure 5.30 that long wavelength signal in SLR-derived J_2 could be explained by using the contributions from these four regions. Inter-annual signals (2005 and 2010) are likely due to the land hydrology.

Another evidence is from steric-corrected sea-level change from radar altimetry. After applying the same process to these sea-level rise observations, we obtain the time series of J_2 results from steric-corrected sea-level change and also the latitude-time plot shown in Figure 5.31 and Figure 5.32. Start around 2006, obvious sea-level rise could be seen around equatorial ocean and its contribution to J_2 is significant that is shown in the bottom figure of Figure 5.32.
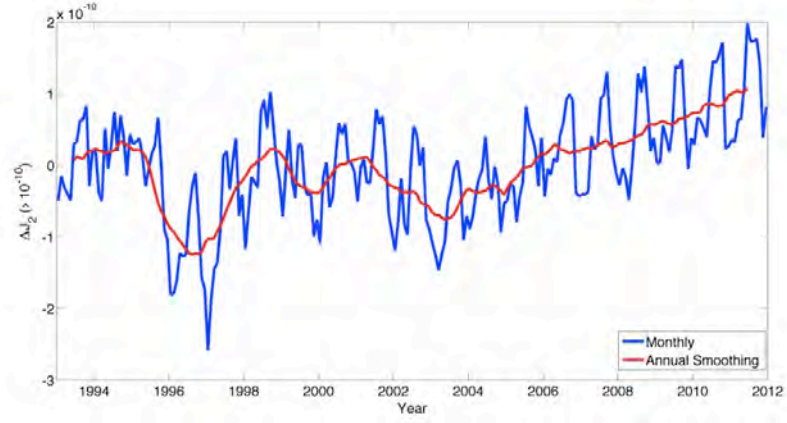
84

Figure 5.31 Time series of J_2 computed from steric-corrected altimetry result.
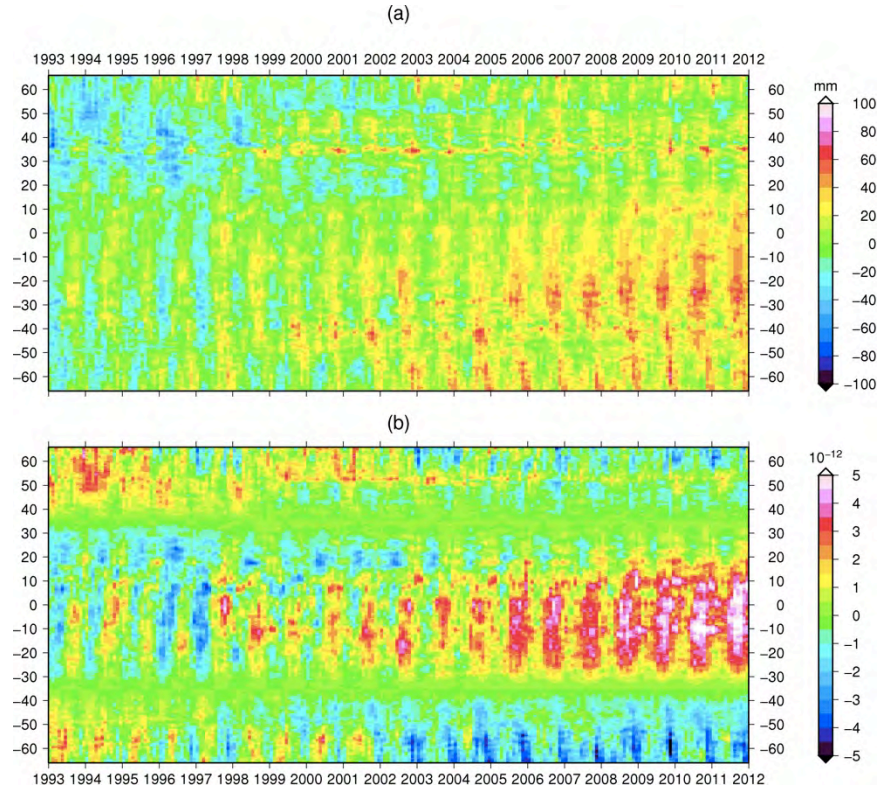

Figure 5.32 Latitude average of (a) steric-corrected sea-level change and (b) its contribution to J_2 (AVISO–Ishii, 0–1500m).

5.5 Chapter Summary

In this chapter, sea-level fingerprint approach is used to investigate the contributions of Earth's ice mass loss to changes of Earth's oblateness. Sensitive kernel test indicates that mass loss from four ice reservoirs are most sensitive to the changes of Earth's oblateness, they are Antarctica, Greenland, Canadian Arctic Archipelago and Alaska. Using mass variation estimated from GRACE, contribution from Antarctica and Greenland are shown to be the dominant. However, this study shows that the mass losses from the Canadian Arctic Archipelago and Alaska glacier/ice caps also contributed to the recent changes of J_2, and they are not negligible.

Latitude average of the mass changes and also its contribution to J_2 are presented. The latitude-time plot shows that polar region mass loss and the resulting melt water redistributed to equatorial part of the ocean are likely the major contribution to recent changes in Earth's oblateness.

One turning point in the J_2 time series exists around 2006. In this study, mass changes from above mentioned four ice reservoirs extracted from GRACE are used to study this turning point. In addition, steric-corrected sea-level change from radar altimetry is also used here to support the GRACE result.

Due to the short time span in this study, the inter-annual signals or longer period signals may still in the extracted trend. Further study is needed when more observations become available.

Chapter 6   Sea-level Rise Study

This chapter presents the results of the sea-level rise study. It includes two parts: (1) Sea-level budget closure study with focus on ocean mass component. (2) Ocean GIA separation from sea-level change observation.

6.1   Introduction

Over a longer time scale, global mean sea level change results from two major processes that cause the change of ocean volume, in addition to the change of seafloor due to GIA, tectonics and other geodynamic processes. The first one is density (or steric) change resulting from the changes in salinity and heat content. The second one is the ocean mass variation that comes from exchanges between the oceans and other reservoirs (e.g., glaciers, ice caps, ice sheets, hydrologic basins, aquifers, and man-make reservoirs).

Here, our objective is to study if the mass component of the sea-level budget is in closure if independent measurements of the ocean mass variations agree, i.e., sea-level observed by GRACE and by steric-corrected satellite altimetry.

Sea-level budget is closed if the following relationship is fulfilled.

$$SL_{Total} = SL_{Steric} + SL_{Mass} \qquad\qquad 6\text{-}1$$

where SL_{Total} is the total sea level, SL_{Steric} is the steric component, SL_{Mass} is the mass component.

With the advances in observation technique, especially the satellite measurement, it is possible to observe these changes in global coverage. For example, right now the total global mean sea level change could be determined precisely using observation from satellite radar altimeter measurement. The ocean mass component and also the water exchange between the ocean and land could be determined using time-variable gravity data from GRACE. The steric component of global mean sea level change could be determined using the *in situ* measurements such as eXpendable BathyThermographs (XBT), Mechanical BathyThermographs (MBTs), and Argo floats.

Besides the steric change and mass change, over a longer time scale, the mantle mass redistribution along with the ongoing viscoelastic response of the solid Earth to the deglaciation since the Last Glacier Maximum, or the GIA process, has been causing ocean floor deformation and the associated gravity change, resulting in global mean sea-level change. Thus, it is necessary to correct this GIA effect from both satellite radar altimeter measurement and satellite gravity measurement to isolate the true sea-level rise signal.

Recent efforts to study sea level budget closure are summarized in Table 6.1. Different GIA models (not consistent for removing its contribution from altimeter or GRACE sea-level data) were used in some studies [*Leuliette and Miller*, 2009; *Leuliette and Willis*, 2011; *Willis et al.*, 2008]. In this study, we use an ensemble of 15 GIA models to quantify the error in GIA correction in the sea-level budget closure exercise. In

addition, other large-scale contributions, such as geocenter motion and C_{20}, are also discussed.

A preliminary study based on an innovative method to assess the feasibility towards the separation of GIA from the present-day ocean mass changes is conducted using steric-corrected altimeter and GRACE data.

Table 6.1 Recent Sea-level budget study

Source	Data Span	GIA model predicted ocean mass trend (mm/yr)	GRACE ocean bottom pressure trend after removing GIA (mm/yr)	Steric or thermal sea level trend from Argo (mm/yr)	Altimetry sea-level trend after removing GIA effect (mm/yr)	Discrepancy (altimetry–GRACE, mm/yr)
[Willis et al., 2008] (Paulson/ICE5G(VM2) model)	2003.07–2007.06	–1.0	0.8±0.8	-0.5±0.5	3.6±0.8	3.3
[Cazenave et al., 2009] (ICE5G(VM2) model)	2003.01–2007.12	–2.0	1.9±0.1	0.37±0.1	2.5±0.4	0.2
[Leuliette and Miller, 2009] (Paulson/ICE5G(VM2) model)	2004.01–2007.12	–1.0	0.8±0.5	0.8±0.8	2.4±1.1	0.8
[Peltier, 2009] ICE5G(VM2) model	2002.08–2007.01	–1.8	2.17±0.37	0.37±0.15	2.50±0.40	–0.04
[Leuliette and Willis, 2011] (Paulson/ICE5G(VM2) model)	2005.01–2010.09	–1.0	1.1±0.6	0.5±0.85	1.5±0.9	–0.1
This study	2004.01–2011.12	–0.73 to –1.64	0.38 to 1.29 (RL05)	0.48±0.05	2.13 to 2.28	0.49 to 1.27

89

6.2   Data Analysis

All the trends mentioned in this study are extracted by using a 6-parameter least squares fit approach. Assume the time series can be decomposed as:

$$data(t) = a + bt + c\sin(2\pi t) + d\cos(2\pi t) + e\sin(4\pi t) + f\cos(4\pi t)$$ 6-2

where t is the time epoch, $data(t)$ could be the steric-corrected sea-level time series or GRACE derived ocean mass component, a is the constant term, and b is the trend term, c, d, e, and f are amplitude of annual terms and semi-annual terms respectively.

6.2.1   Radar Altimetry

Multi-satellite observation from AVISO[2] (Archiving, Validation and Interpretation of Satellite Oceanographic data) is used in this study. The data period is spanning from January 1993 to December 2011. For the ocean mass budget study, however, the period is chosen from January 2004 to December 2011 to ensure the same data span for all data types.

Figure 6.1 shows the global mean sea level time series determined from multi-satellite measurements.
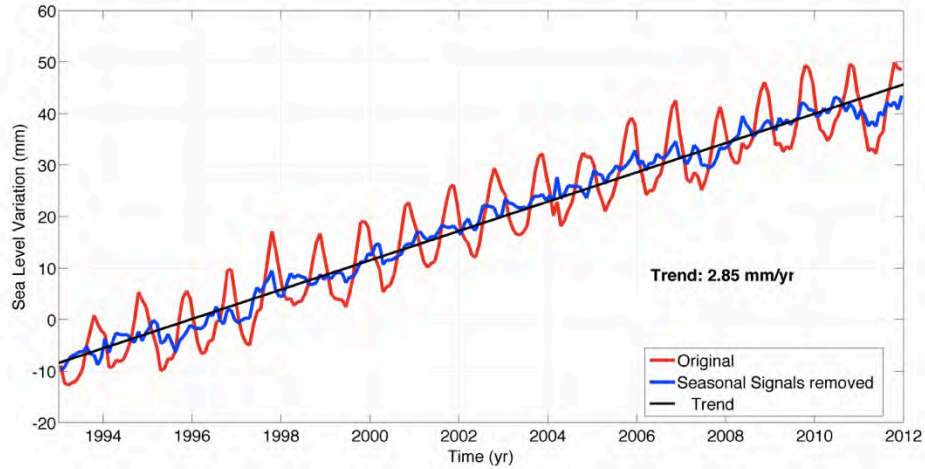

Figure 6.1 Time series of sea-level change from multi-satellite altimeter data (AVISO) (1993.01~2011.12). Red line denotes the time series with seasonal signals included; blue line indicates the time series after removing seasonal signals. GIA contribution to ocean deepening is not removed, taking account for this GIA contribution will cause a 0.3 mm/yr increase in the total trend [*Douglas and Peltier*, 2002].

Figure 6.2 shows that the coverage of data that were used in the study from radar altimetry measurements (bottom), and also shows that two geographical mean sea-level trends extracted by using two different time span observations (top: 1993.01~2011.12; middle: 2004.01~2011.12). In this study, we will only use the latter time span

---

[2] The altimeter products were produced by Ssalto/Duacs and distributed by Aviso, with support from Cnes (http://www.aviso.oceanobs.com/duacs/)

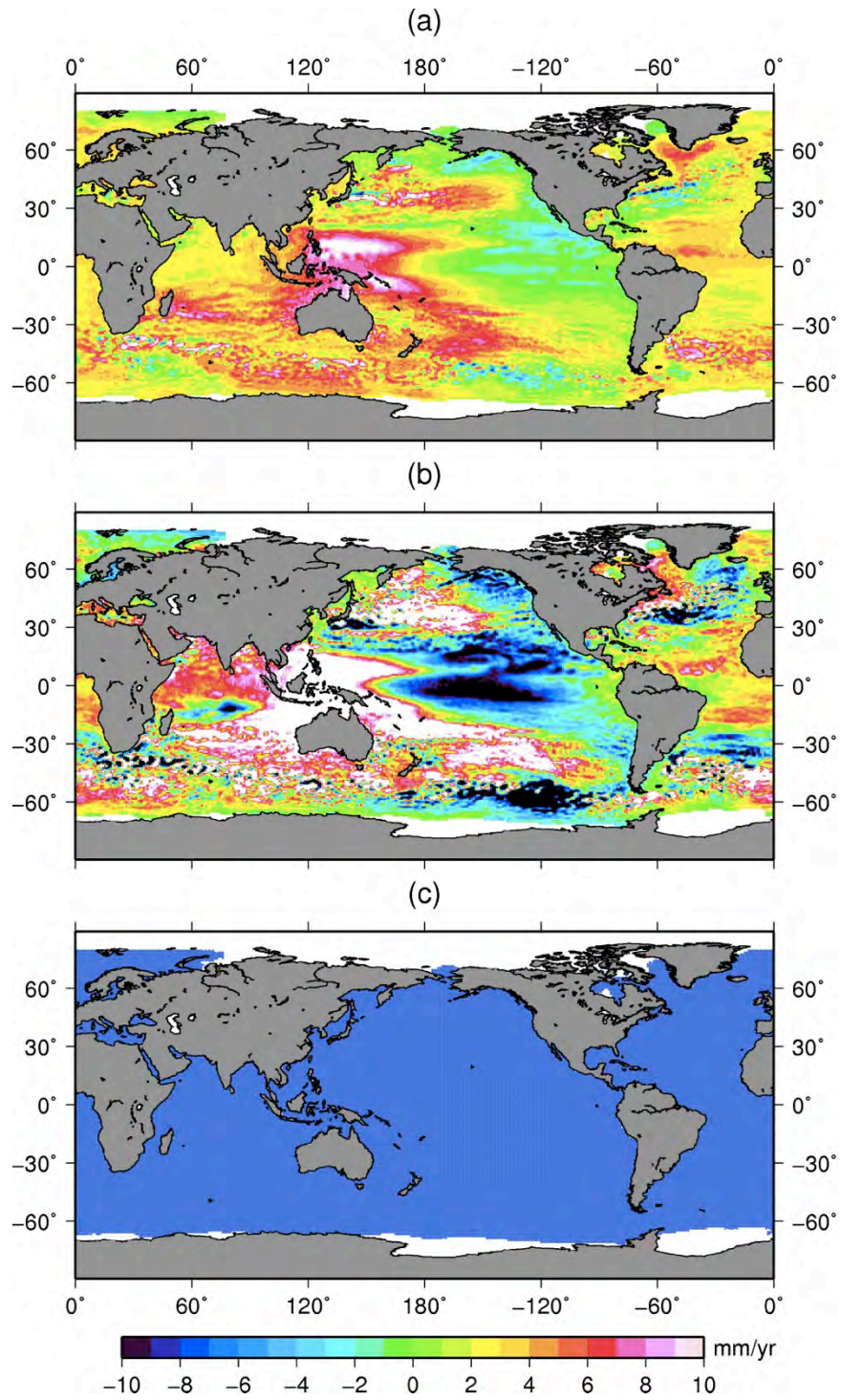(2004.01~2011.12) in order to make sure that all types of the observations cover the same time period.

Figure 6.2 (a): Geographical plot of AVISO measured sea-level change and data coverage (1993.01~2011.12); (b): Geographical plot of AVISO measured sea-level change (2004.01~2011.12); (c): Data coverage (blue dots).

92

Table 6.2 Sea-level variations from multi-satellite altimeter data (AVISO) (unit: mm/yr). First case is the average using all available data. Second case (2004.01~2011.12) is the average over the study region.

Data	Trend (mm/yr)
AVISO (1993.01–2011.12)	2.85
AVISO (2004.01–2011.12)	1.89

6.2.2 Steric/thermal Sea-Level Change

For the steric/thermal component of sea level measurement, three types of data set are used in this study and summarized as follows. The steric/thermal results are based on the grid data, which was processed and kindly provided by Chung-Yen Kuo and Wenhao Lan, National Cheng Kung University, Taiwan [*Pers. Comm.*].

Table 6.3 Steric and thermal data used in this study.

	Data Source	Period	Depth	Reference
Ishii	XBT, MBT, Argo	1993.01~2011.12	0–700m, 0–1500m	[*Ishii and Kimoto*, 2009]
JAMSTEC	Argo	2001.01~2011.12	0–2000m	[*Hosoda et al.*, 2008]
SIO	Argo	2004.01~2010.12	0–2000m	[*Roemmich and Gilson*, 2009]

The time series of steric/thermal component of global mean sea level from the above data sets are shown in Figure 6.3, Figure 6.4 and Figure 6.5. Taking Ishii data set presented in Figure 6.3 as an example, the differences between steric and thermal are smaller than the differences between different depths. The differences are also shown geographically in Figure 6.6, most of the differences exist in the location of Southern Ocean, southern part of Atlantic Ocean (around 40°S) and northern part of Atlantic Ocean (near Greenland). In addition, the abyss parts of the ocean are lack of observations, and we rarely know the steric or thermal effects due to this part of the ocean to the present sea-level rise. One should take the depth into account when trying to interpret different steric (or thermal) result.

Geographical plots for each data set are shown in Figure 6.6, Figure 6.8, and Figure 6.9. Differences between them are mainly due to different time span chosen to fit the trend. One may notice that the data coverage is also different for these three data sets. In the following study of ocean mass component of the sea-level budget closure, common area from all three data sets (Figure 6.21) are chosen to make the comparison more robust.

For the same time span, the extracted steric/thermal component of mean sea-level change are plotted geographically and compared as shown in Figure 6.10 and Figure 6.11. Major differences exist in the Southern Ocean for JAMSTEC data, it shows larger positive signal than the others in both steric and thermal component of sea-level change.
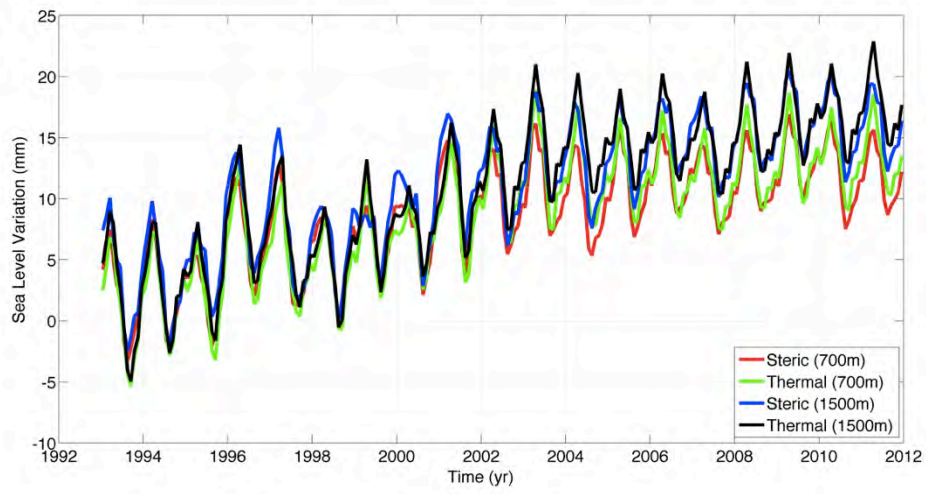
Figure 6.3 Time series of sea-level variation extracted from Ishii steric (Red: 0–700m; Blue: 0–1500m) and thermal (Green: 0–700m; Black: 0–1500m) products (2001.01~2011.12).
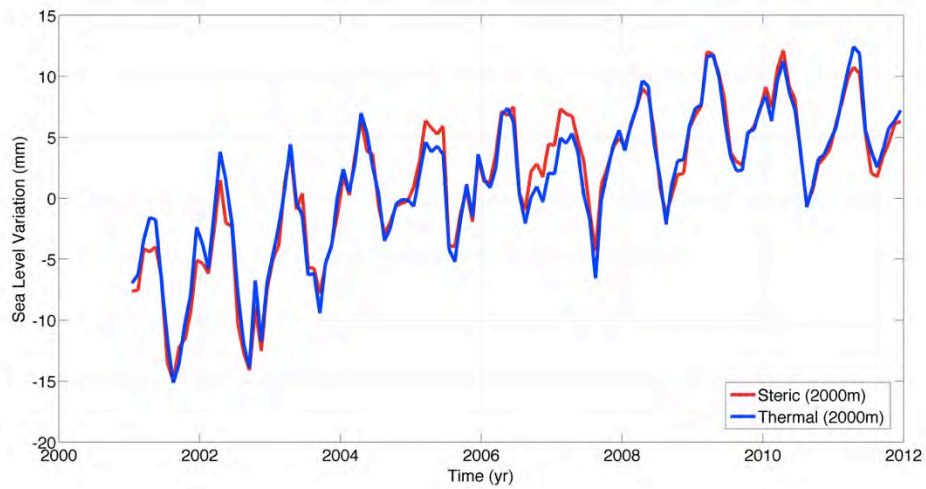

Figure 6.4 Time series of sea-level variation extracted from JAMSTEC steric (Red) and thermal (blue) products (2001.01~2011.12).
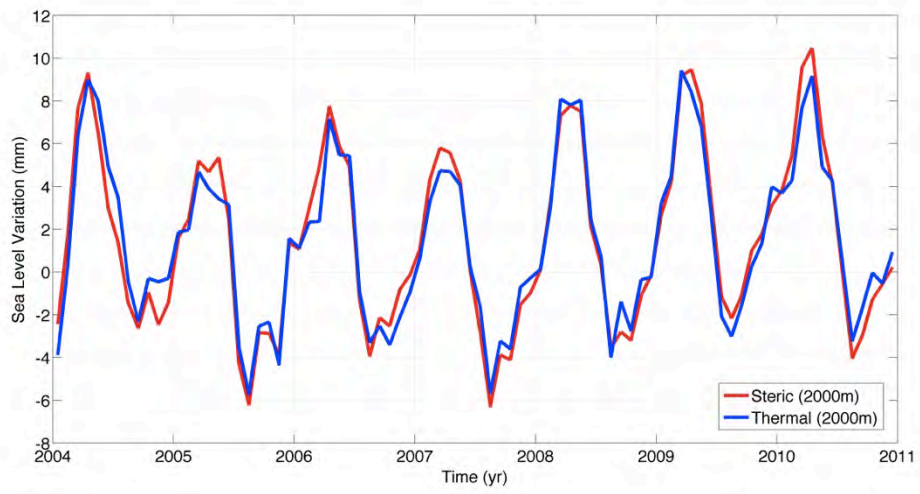
Figure 6.5 Time series of sea-level variation that extracted from SIO steric (red) and thermal (blue) product (2004.01~2010.12).
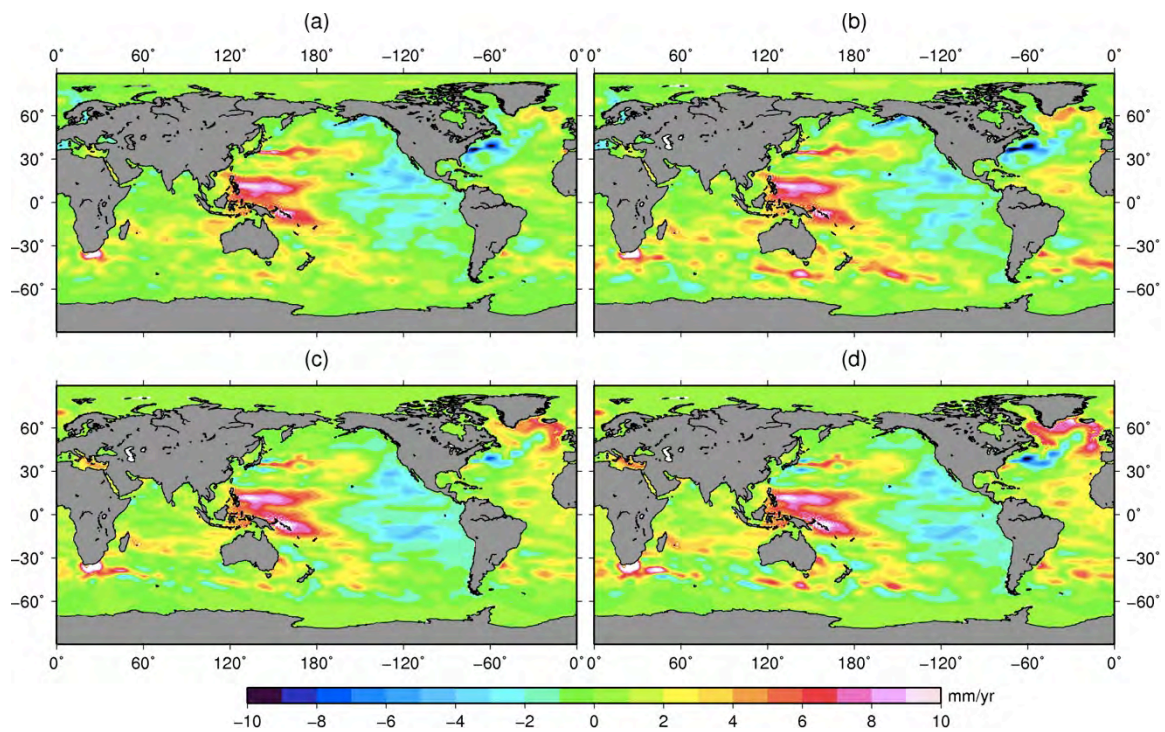
Figure 6.6 Extracted steric and thermal component of sea-level change from Ishii data (1993.01~2011.12). (a) Steric (0–700m); (b) Steric (0–1500m); (c) Thermal (0–700m); (d) Thermal (0–1500m).
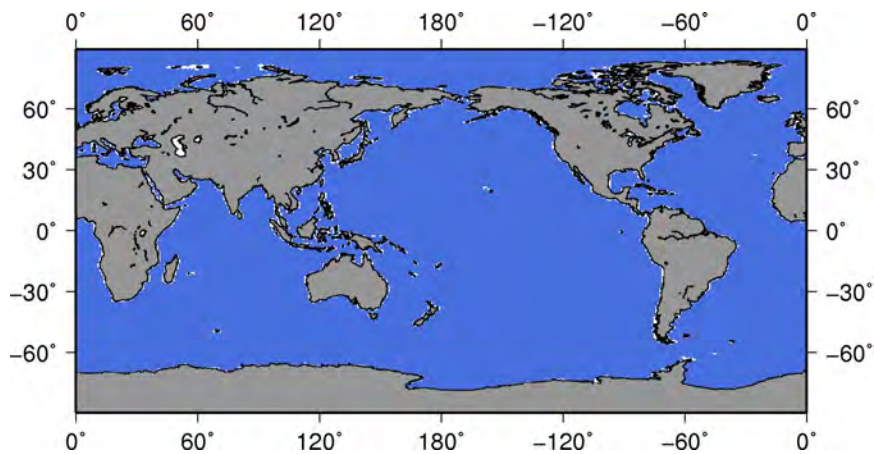

Figure 6.7 Data coverage of Ishii steric/thermal in-situ observations.

Figure 6.8 Extracted steric component (a) and thermal component (b) of sea-level change using JAMSTEC (0-2000m) data (2001.01~2011.12). (c): Data coverage. The white area indicates that no data available beyond latitude 66°N and 60°S.
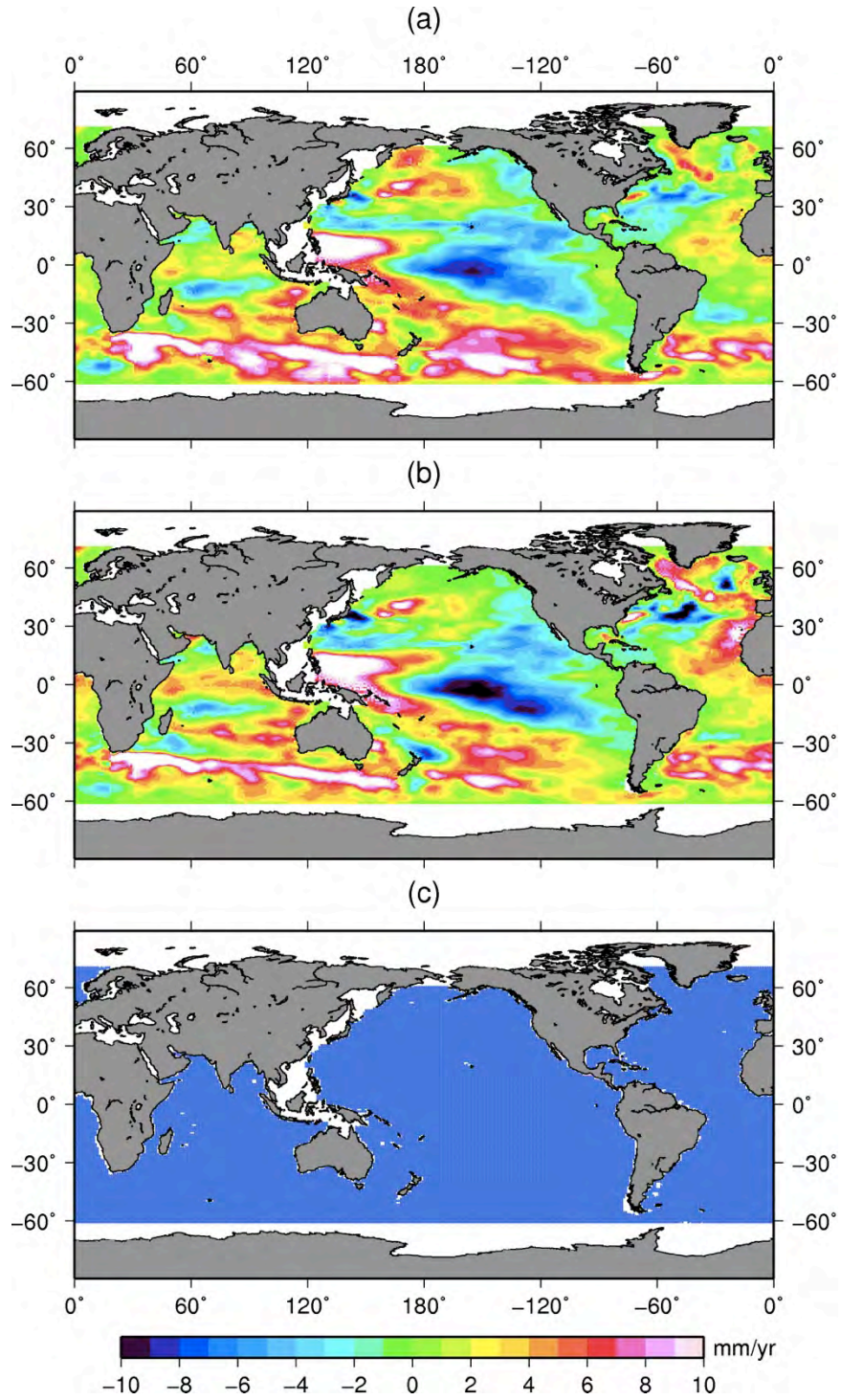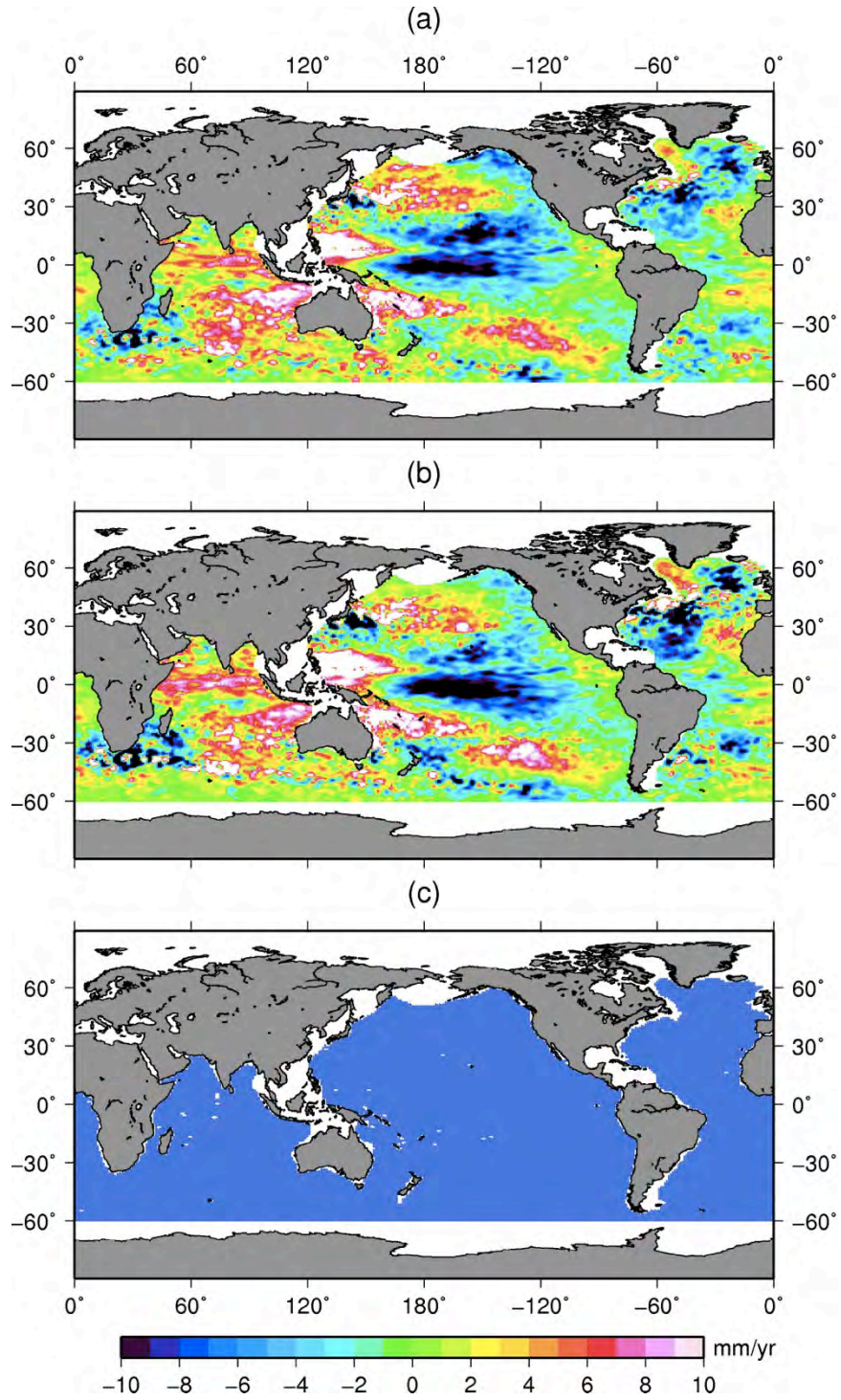
Figure 6.9 Extracted steric component (a) and thermal component (b) of sea-level change using SIO (0–2000m) data (2004.01~2010.12). (c): Data coverage. The white area indicates that no data available beyond latitude 66°N and 60°S.

98
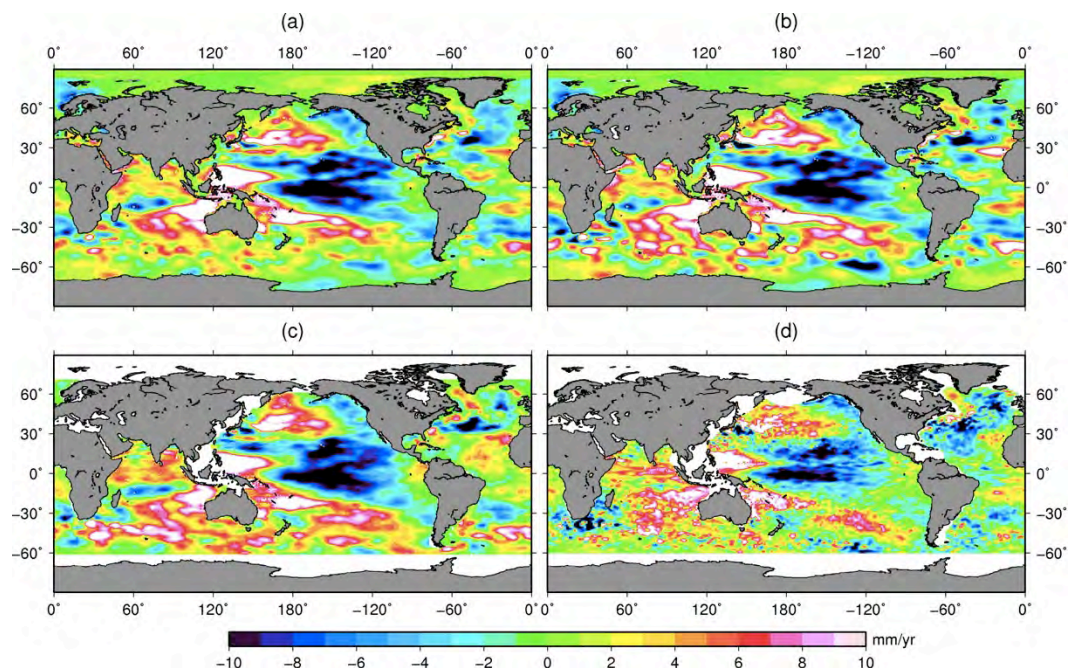
Figure 6.10 Extracted steric component of global mean sea level change (Ishii and JAMSTEC: 2004.01~2011.12; SIO: 2004.01~2010.12). (a) Ishii (0–700m); (b) Ishii (0–1500m); (c) JAMSTEC (0–2000m); (d) SIO (0–2000m).

Figure 6.11 Extracted thermal component of global mean sea level change (Ishii and JAMSTEC: 2004.01~2011.12; SIO: 2004.01~2010.12). (a) Ishii (0–700m); (b) Ishii (0–1500m); (c) JAMSTEC (0–2000m); (d) SIO (0–2000m).
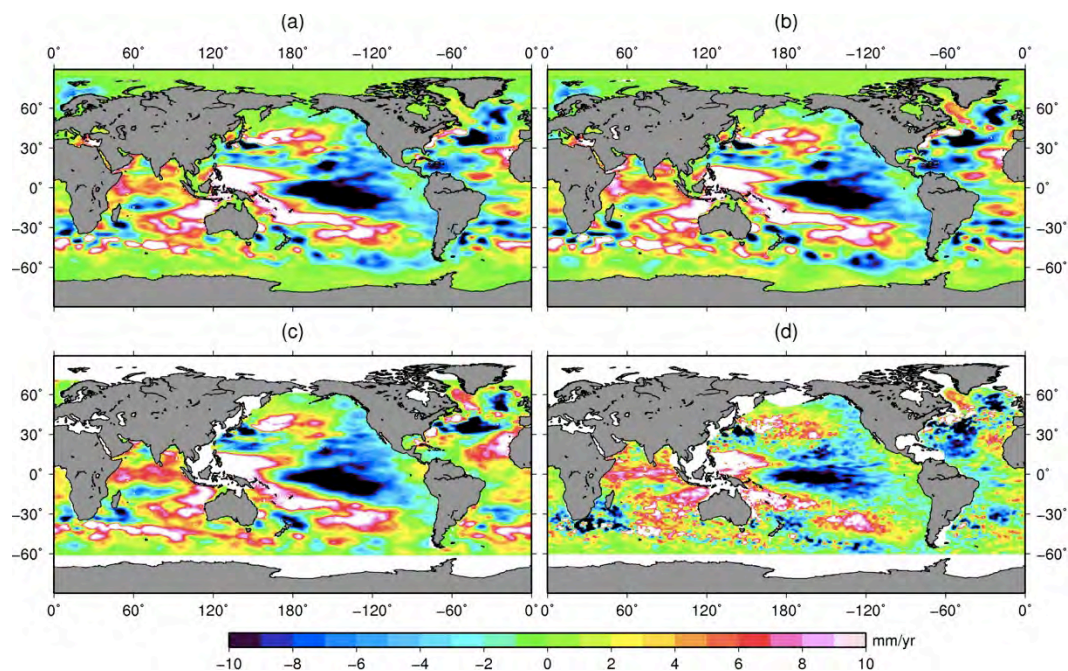
6.2.3 Steric- (or Thermal-) Corrected Sea-Level Change

When subtracting steric or thermal component from observed total sea-level change from radar altimetry, we will have the so-called steric-corrected or thermal-corrected sea-

level change. In principle, this will be comparable to the ocean mass component obtained from other techniques such as GRACE.

The steric-corrected and thermal-corrected sea level changes are plotted in Figure 6.12, Figure 6.14 and Figure 6.23 for the respective time span. The differences result from the differences in respect steric (or thermal) component.
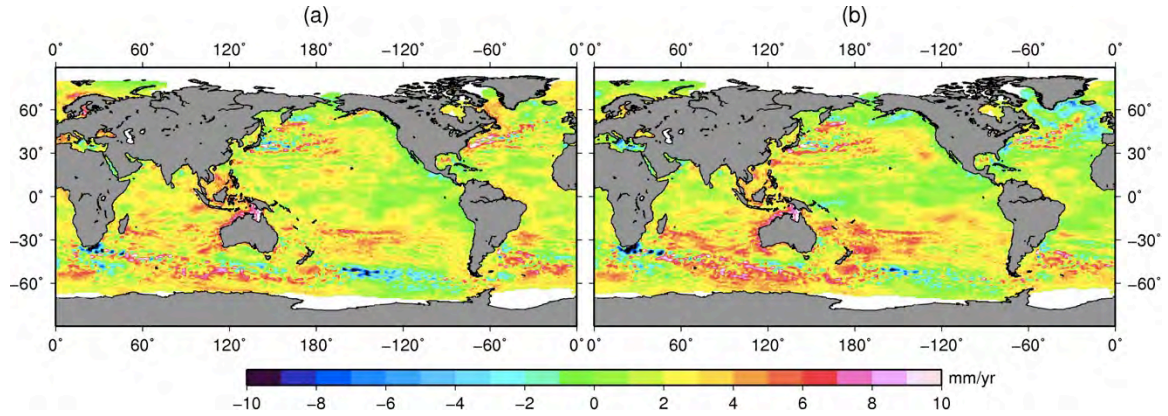
Figure 6.12 Ishii steric-corrected (a) and thermal-corrected (b) mean sea-level, 0–1500m, 1993.01~2011.12.

Figure 6.13 Time series of sea-level variation extracted from Ishii (0–1500m) steric- (thermal-) corrected multi-satellite altimeter data. Top: seasonal signal included; Bottom: seasonal signals removed

Table 6.4 Steric and thermal effect on sea-level variations (unit: mm/yr). Average is made using all available data.

Data	From	To	Steric (mm/yr)	Thermal (mm/yr)
Ishii (0–1500m)	1993.01	2011.12	0.83	0.92
Ishii (0–700m)	1993.01	2011.12	0.64	0.74
JAMSTEC (0–2000m)	2001.01	2011.12	1.53	1.42
SIO (0–2000m)	2004.01	2010.12	0.30	0.23

Figure 6.14 JAMSTEC Steric- (a) and thermal- (b) corrected mean sea-level trend (2001.01~2011.12).

Figure 6.15 Time series of sea-level variation extracted from JAMSTEC (0–2000m) steric- (thermal-) corrected multi-satellite altimeter data (AVISO). Top: Seasonal signal included; Bottom: Seasonal signal removed.
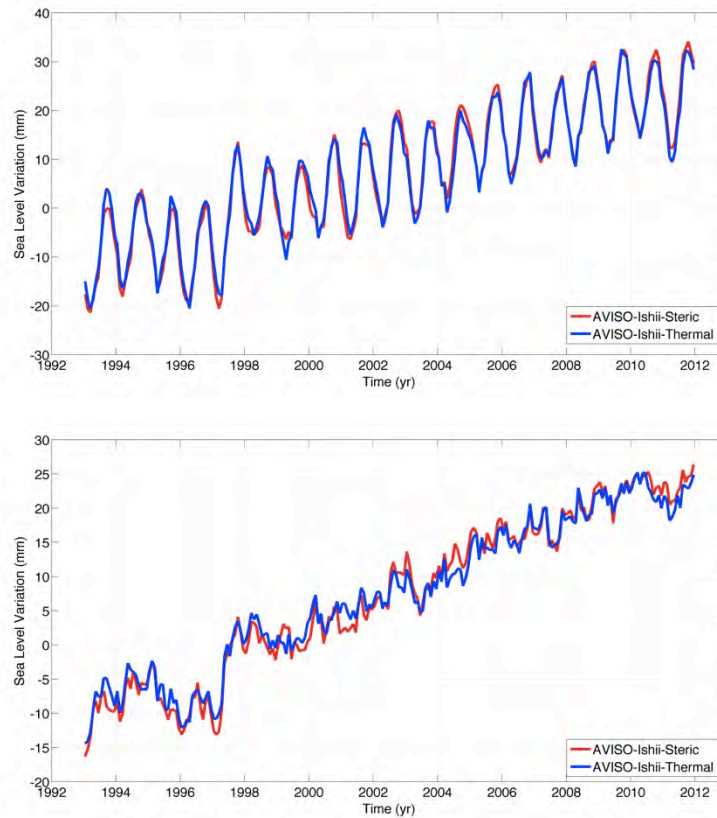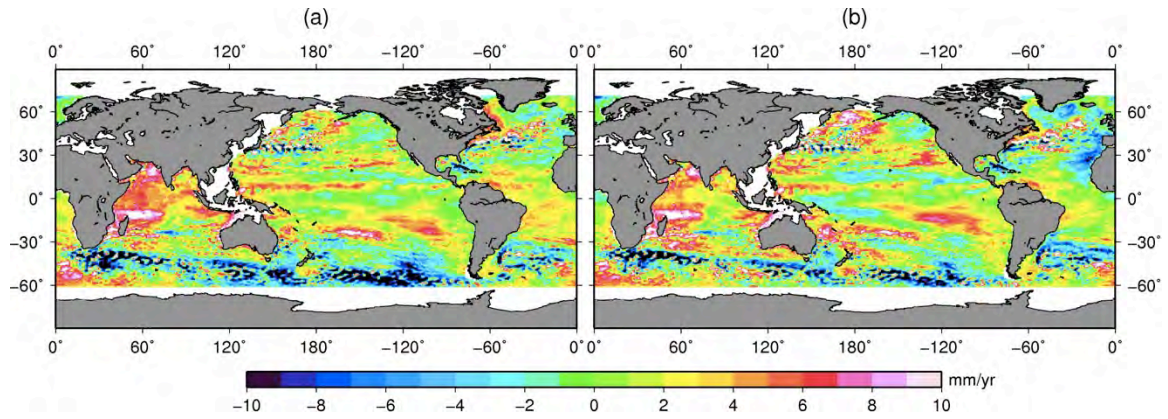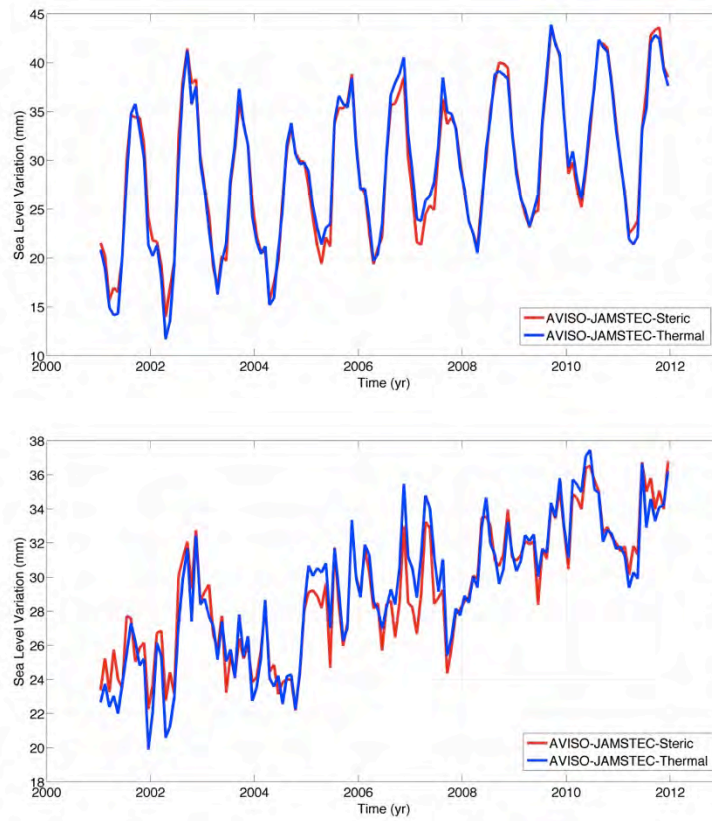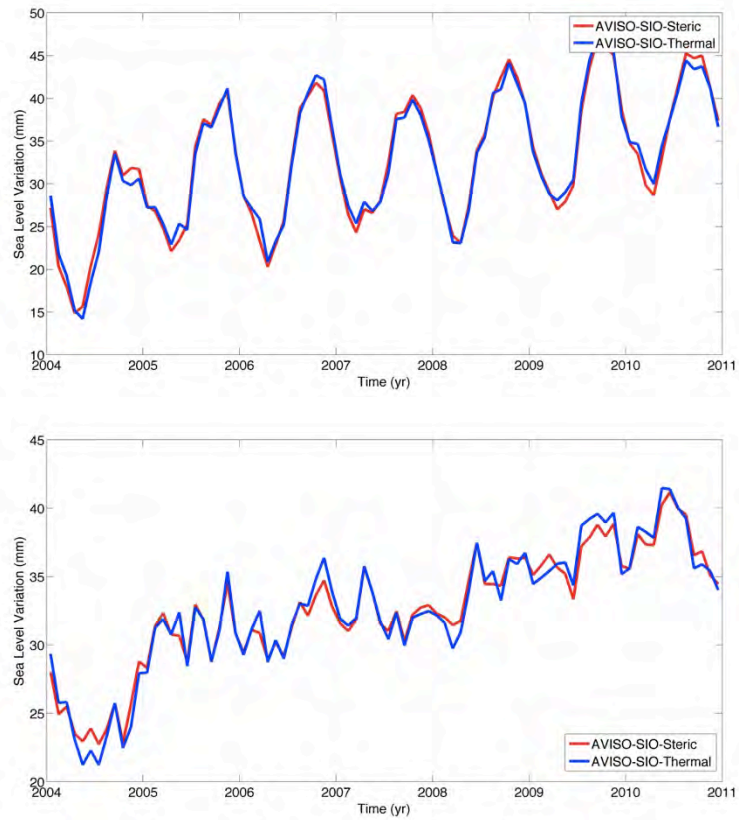
Figure 6.16 Time series of sea-level variation extracted from SIO (0–2000m) steric- (thermal-) corrected multi-satellite altimeter data (AVISO). Top: Seasonal signal included; Bottom: Seasonal signal removed.

Table 6.5 Steric- (thermal-) corrected sea-level variations from multi-satellite altimeter data (AVISO) (unit: mm/yr). Average is made using all available data.

Data	From	To	Steric-Corrected Trend (mm/yr)	Thermal-Corrected Trend (mm/yr)
AVISO-Ishii	1993.01	2011.12	2.02	1.93
AVISO-JAMSTEC	2001.01	2011.12	0.78	0.89
AVISO-SIO	2004.01	2010.12	1.79	1.87

6.2.4 GRACE

GRACE Level-2 RL05 monthly data products from three official data centers are used in this study: CSR, GFZ and JPL. Two types of their product are used: GSM and GAD.

According to GRACE Level-2 user handbook, 'G' here denotes 'geopotential coefficients', 'S' denotes 'estimate made from only GRACE data', 'A' denotes 'average of any background model over a time period', 'M' denotes the 'estimates of the static field', 'D' denotes 'bottom-pressure over oceans, zero over land'. Thus, 'GSM' indicates the geopotential coefficients of static field that are estimated from only GRACE data.

103

'GAD' indicates that the geopotential coefficients of ocean bottom-pressure that are averaged over a certain time period.

For the time span, in order to be consistent with radar altimetry result, monthly solutions from January 2004 to December 2011 are chosen to extract the mass component of sea-level change.

There are 4 months missing in GSM product due to insufficient good observation in the computation, the missing months are: June 2003, January 2011, June 2011, May 2012. In this study, the missing months are linearly interpolated by using data from 2 months before and 2 month after.

The processing procedure is described in Chapter 4.

The difference between CSR and GFZ solution is due to the chosen of replacement of C_{20}. From Table 6.13, the effect of C_{20} is almost the same with the difference of CSR and GFZ solutions.
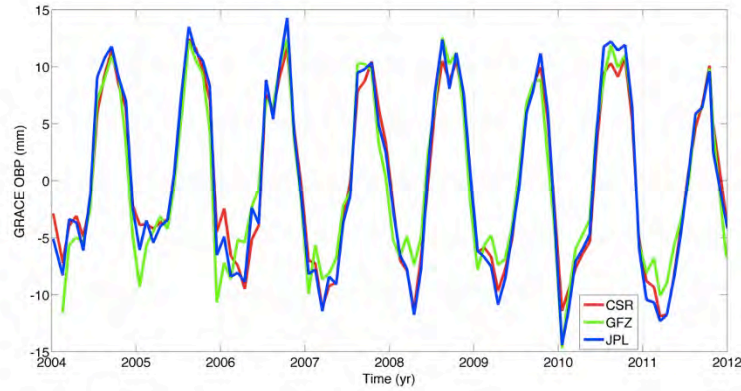
Figure 6.17 Time series of GRACE-derived Ocean Bottom Pressure (OBP) extracted from three data centers (GSM+GAD). Red: CSR; Green: GFZ; Blue: JPL. For CSR and JPL, C_{20} is replaced using SLR-derived values. A 350 km Gaussian smoothing is applied. No GIA model is applied.
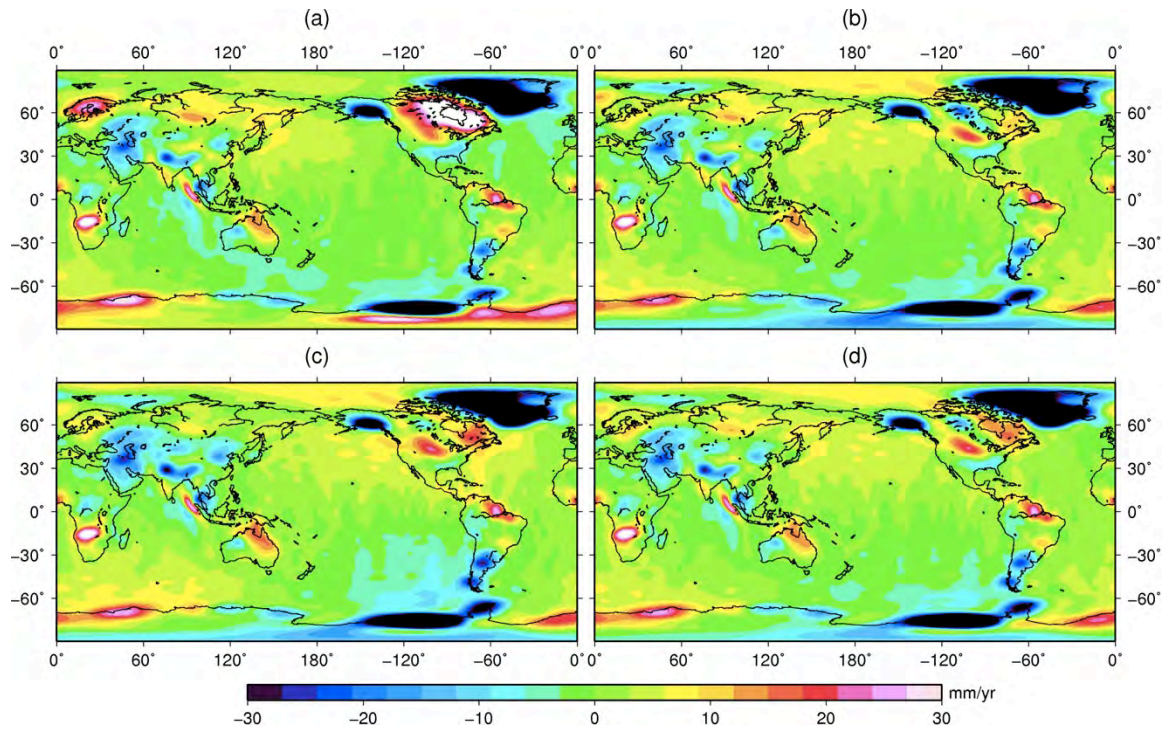
Figure 6.18 GRACE-derived Mass Change Rate from CSR RL05 (2004.01~2011.12), Decorrelation [*Duan et al.*, 2009], 350 km Gaussian smoothing. (a) No GIA model applied; (b) Pau_5_R GIA model applied; (c) Pel_5_VM2_R GIA model applied; (d) vdW_5_R GIA model applied.

Table 6.6 Effect of different solution on derived ocean bottom pressure over study region.

Solution	OBP (mm/yr)
CSR-GFZ	-0.22
CSR-JPL	0.00
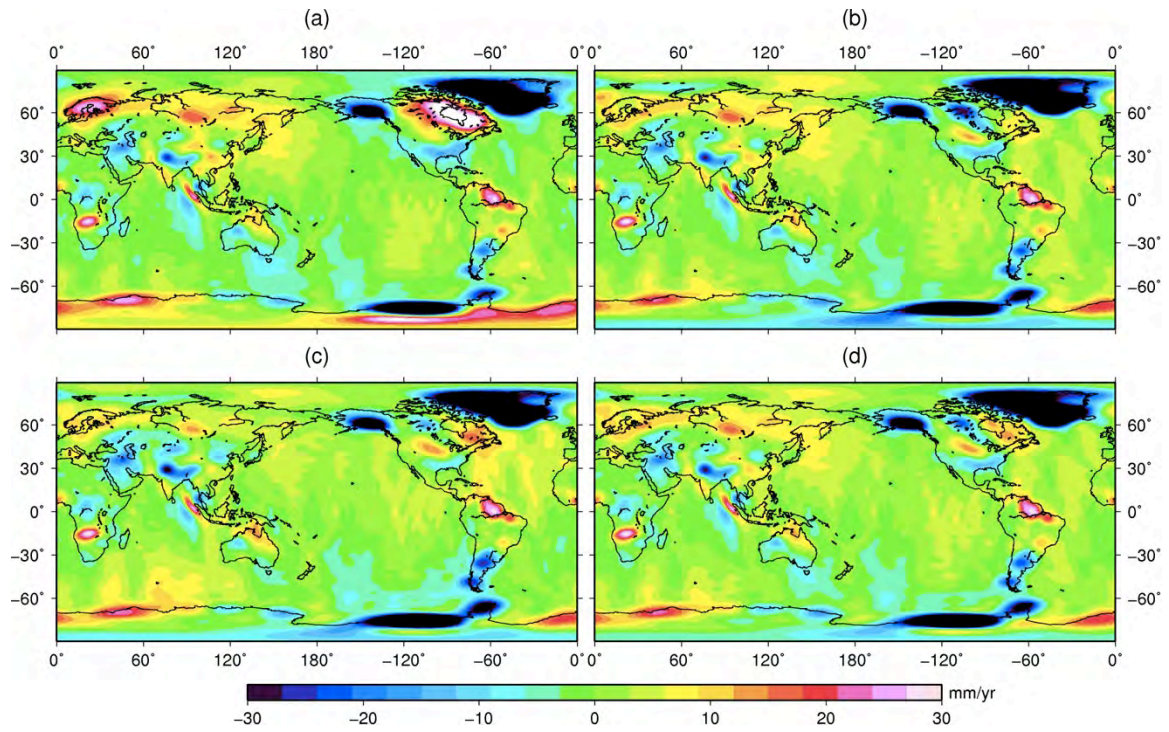
Figure 6.19 GRACE-derived Mass Change Rate from GFZ RL05 (2004.01~2011.12), Decorrelation [*Duan et al.*, 2009], 350 km Gaussian smoothing. (a) No GIA model applied; (b) Pau_5_R GIA model applied; (c) Pel_5_VM2_R GIA model applied; (d) vdW_5_R GIA model applied.
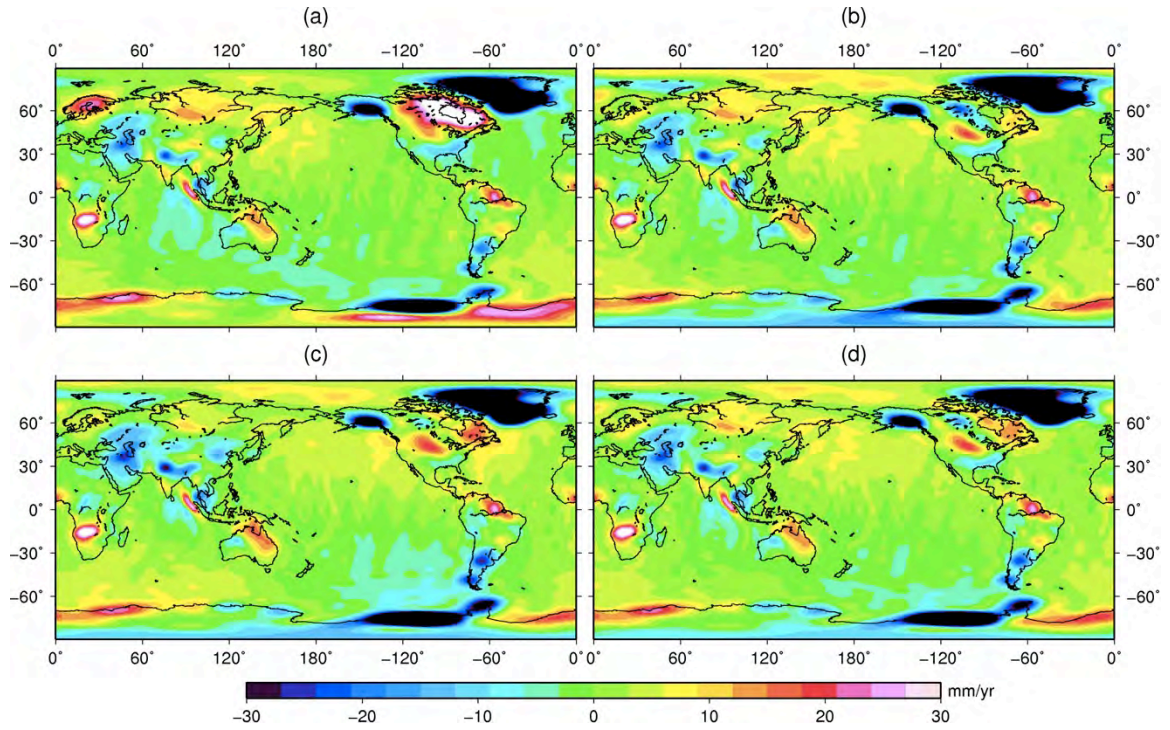
Figure 6.20 GRACE-derived Mass Change Rate from JPL RL05 (2004.01~2011.12) C_{20} terms is replaced using SLR-derived C_{20}. Decorrelation [*Duan et al.*, 2009], 350 km Gaussian smoothing. (a) No GIA model applied; (b) Pau_5_R GIA model applied; (c) Pel_5_VM2_R GIA model applied; (d) vdW_5_R GIA model applied.
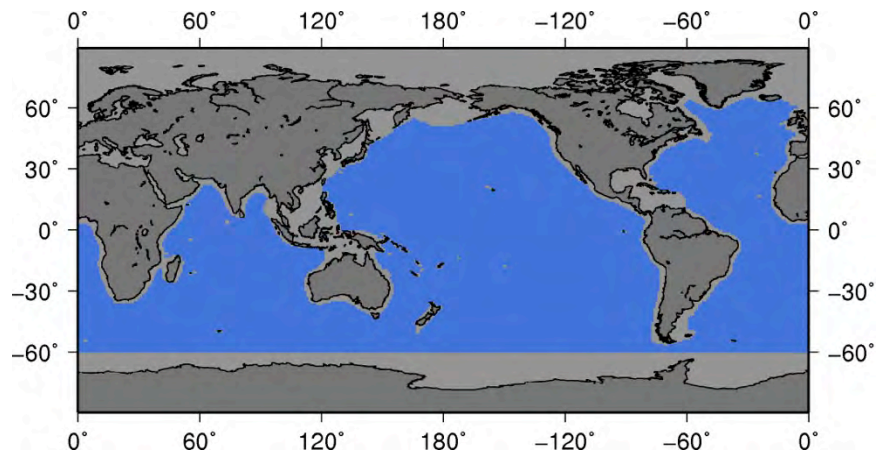
Figure 6.21 Selected study region (blue area) in which all the data are available.
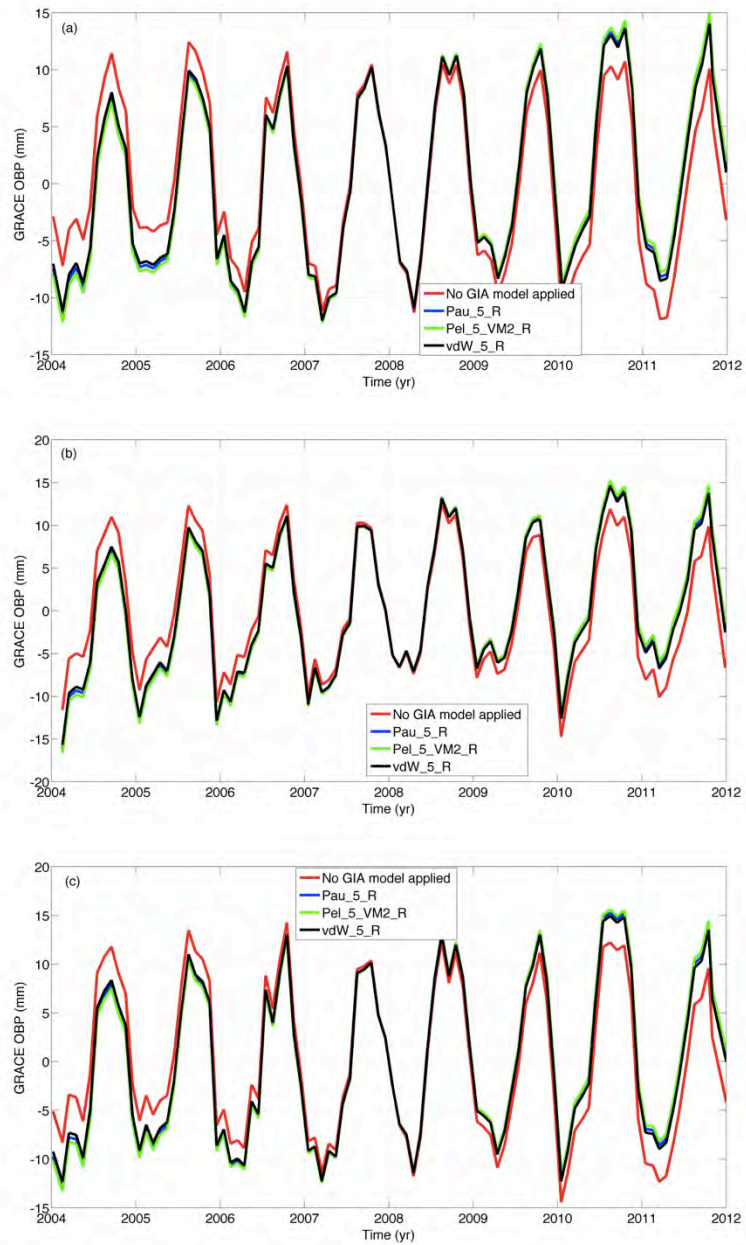
Figure 6.22 Time series of GRACE-derived Ocean Bottom Pressure (OBP) extracted from GRACE RL05 product (2004.01~2011.12), (a) CSR; (b) GFZ; (c) JPL. C_{20} is replaced by SLR-derived values for CSR and JPL. A 350km Gaussian smoothing is applied. Red: no GIA model applied. Blue: Pau_5_R model applied; Green: Pel_5_VM2_R model applied; Black: vdW_5_R model applied.

6.3   Sea-Level Budget Closure and Major Factors that Influence the Estimation of Global Sea-Level Change

Figure 6.21 shows the study region. It represents the region where three types of measurements are available. In the chosen time span, the steric-corrected mean sea level that using three data sets is shown geographically in the left column of Figure 5.26. The time series were shown in the left column of Figure 5.27. It was shown that both the amplitude and phase are similar in the steric-corrected mean sea-level using three steric data sets. Compared to GRACE-derived ocean mass component, seasonal signals provide similar pattern, but the trends are different from each other.

According to this study, we still cannot say that the ocean mass component of the sea-level rise budget is in closure. In order to further investigate the secular trend, we will discuss several larger contributions to this trend, that is (1) GIA; (2) Geocenter motion (degree 1 terms); (3) C_{20} (or J_2).

Table 6.7 Steric and thermal effect on sea-level variations (unit: mm/yr). Average is made over the study region (2004.01 to 2010.12 or 2011.12)

Data	From	To	Steric (mm/yr)	Thermal (mm/yr)
Ishii (0–1500m)	2004.01	2011.12	0.36	0.34
Ishii (0–700m)	2004.01	2011.12	0.16	0.16
JAMSTEC (0–2000m)	2004.01	2011.12	0.79	0.92
SIO (0–2000m)	2004.01	2010.12	0.30	0.23

Table 6.8 Steric- (thermal-) corrected sea level variations from AVISO (unit: mm/yr). Average is made over study region (2004.01 to 2010.12 or 2011.12).

Data	From	To	Steric-Corrected Trend (mm/yr)	Thermal-Corrected Trend (mm/yr)
AVISO-Ishii	2004.01	2011.12	1.52	1.55
AVISO-JAMSTEC	2004.01	2011.12	1.10	0.96
AVISO-SIO	2004.01	2010.12	1.79	1.87

Table 6.9 Trend of Ocean Bottom Pressure from GRACE RL05.

Data	From	To	CSR (mm/yr)	GFZ (mm/yr)	JPL (mm/yr)
GRACE (No GIA)	2004.01	2011.12	-0.35	-0.16	-0.38
GRACE (Paulson)	2004.01	2011.12	0.80	0.99	0.78
GRACE (Pel-5-VM2-R)	2004.01	2011.12	0.94	1.13	0.91
GRACE (vdW-5-R)	2004.01	2011.12	0.69	0.88	0.67
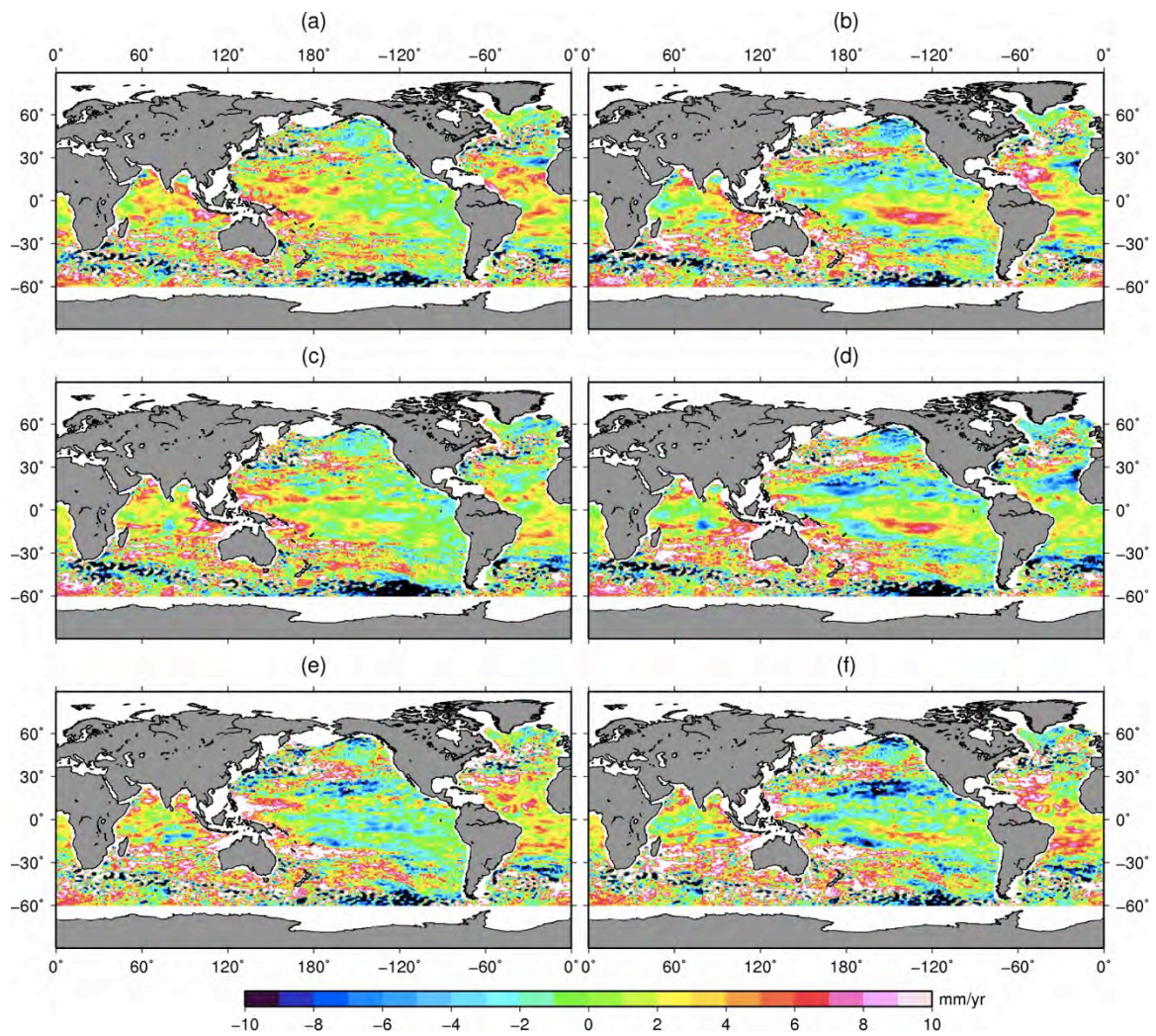
Figure 6.23 Steric- (left) and thermal- (right) corrected mean sea-level using from all three data set (Ishii and JAMSTEC: 2004.01~2011.12; SIO: 2004.01~2010.12). From top to bottom: Ishii (0–1500m); JAMSTEC (0–2000m) and SIO (0–2000m).
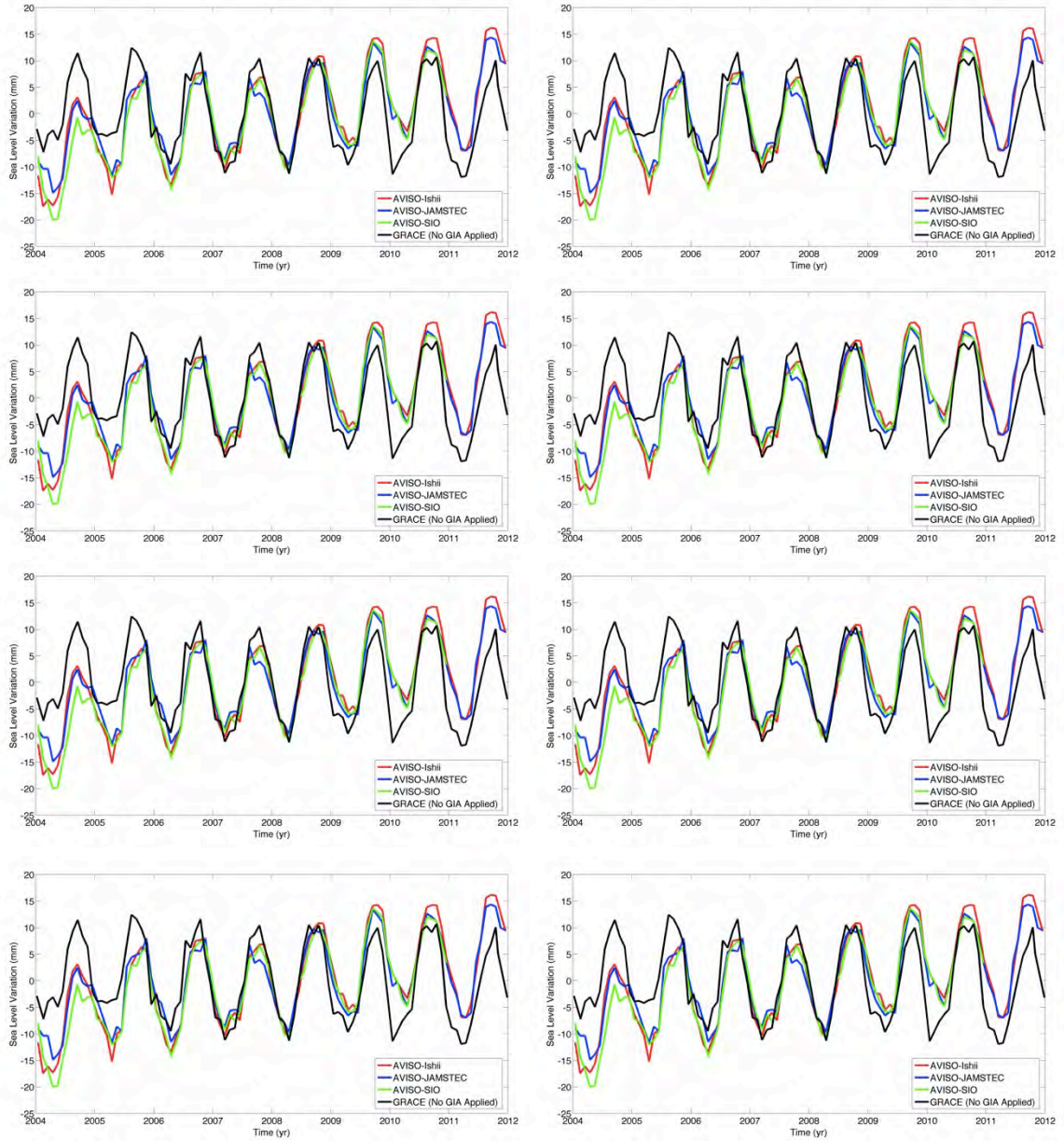
Figure 6.24 Sea level variation time series extracted from Steric-corrected AVISO and GRACE. From top to bottom: No GIA model applied; Pau_5_R GIA model; Pel_5_VM2_R; vdW_5_R GIA model. Left: with seasonal signals. Right: without seasonal signals.
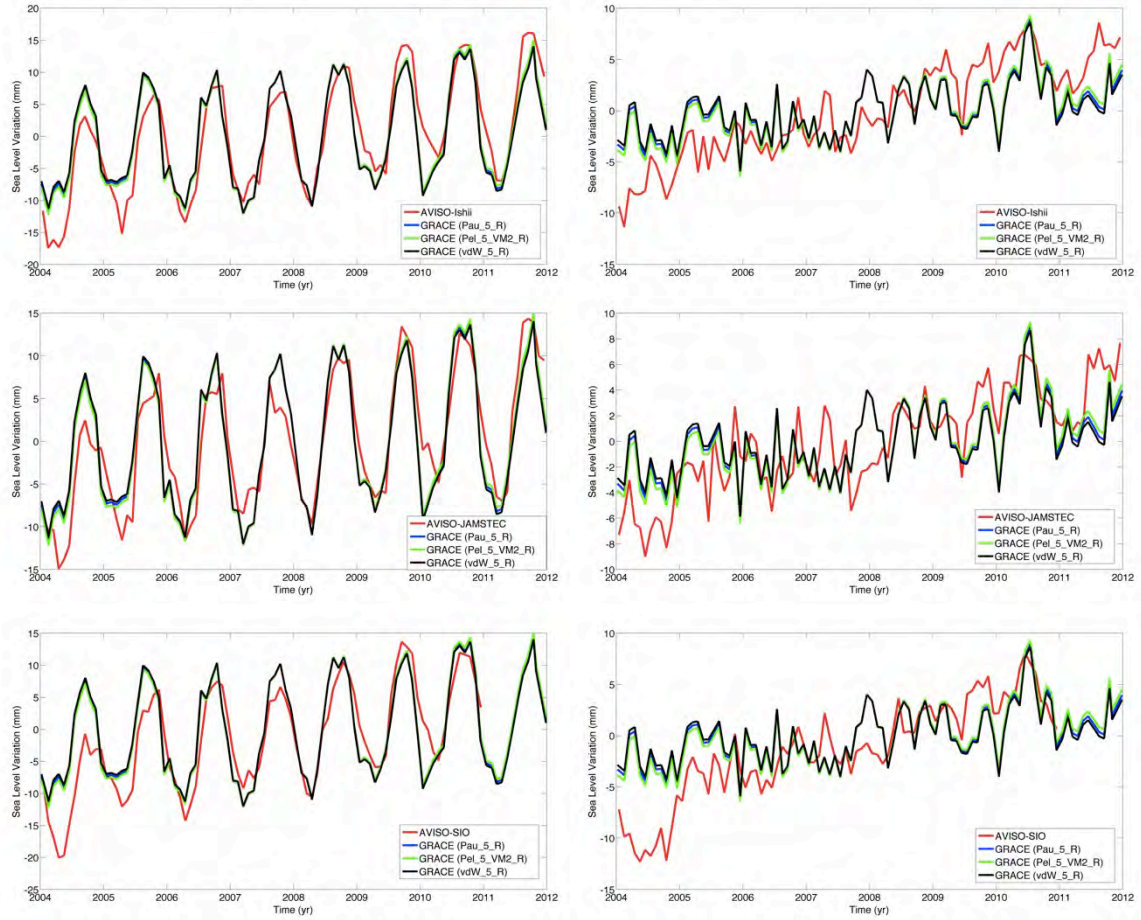
Figure 6.25 Sea level variation time series extracted from Steric-corrected AVISO and GRACE. Three steric product are used: Ishii (top), JAMSTEC (middle), SIO (bottom). Left: with seasonal signals. Right: without seasonal signals.

6.3.1   GIA

For a time scale less than 100 years, GIA signal could be treated as a linear trend, and its effect on both radar altimetry measurement and GRACE result behave as a secular trend. About the comparison between contemporary GIA models, we have already discussed it in detail in Chapter 3.

Table 6.10 and Table 6.11 summarize the GIA correction over the study region. For the study region, the GIA correction for radar altimetry observations is -0.29±0.08 mm/yr. While for GRACE observed ocean mass component, this number increase to -1.25±0.44 mm/yr. We could conclude that GIA play a vital role in the derived secular trend of the ocean mass component from GRACE observations. It is thus vital to choose the most accurate GIA model.

It is shown that GIA contribution to satellite altimetry measurement is relatively smaller than the contribution to GRACE measurement. That is because the density of mantle mass is almost four times than the density of water, this ocean deepening due to

GIA results in larger mass loss in ocean area (mantle mass from ocean area to the pre-glaciated area) that could be captured by satellite gravity mission.

Table 6.10 GIA contribution in Satellite altimetry measured sea level variation over study region.

MODEL	GIA (mm/yr)
Pel_4_VM2	−0.24
Pel_5_VM2_R	−0.29
Pel_5_VM2_R_O	−0.39
Pel_5_VM4_R_O	−0.32
SaS_1	−0.15
SaS_3	−0.38
SKM_O_R	−0.25
SVv_3_REF	−0.38
SVv_L_ALT	−0.15
vdW_5	−0.24
vdW_5_R	−0.27
WaO_EGOD	−0.24
WaW_4	−0.34
WaW_5	−0.38
Mean and STD	**−0.29±0.08**

Table 6.11 Statistics of GRACE-Type Mass Rate over study region.

Model	GIA correction (mm/yr)
Pau_5_R	−1.21
Pel_4_VM2	−1.02
Pel_5_VM2_R	−1.33
Pel_5_VM2_R_O	−1.76
Pel_5_VM4_R_O	−1.60
SaS_1	−0.68
SaS_3	−1.72
SKM_O_R	−0.84
SVv_3_REF	−1.80
SVv_L_ALT	−0.37
vdW_5	−0.96
vdW_5_R	−1.09
WaO_EGOD	−1.03
WaW_4	−1.59
WaW_5	−1.69
Mean and STD	**−1.25±0.44**

6.3.2 Degree 1 (Geocenter Motion)

The effect of geocenter motion is already captured by satellite radar altimetry observations, but GRACE observation is not sensitive to this effect (in the GRACE Level-2 product, degree 1 terms are set to be zero). To compare the steric-corrected altimetry result with the ocean mass component derived from GRACE, it is necessary to take into account the contribution of degree 1 terms. Figure 6.26 and Figure 6.27 present the simulation study of the effect of geocenter motion to both satellite altimetry and satellite gravity observations. Results are given in Table 6.12.

For altimetry, the formula is:

$$\Delta R(\theta,\lambda) = \Delta X \cos\lambda\cos\theta + \Delta Y \sin\lambda\cos\theta + \Delta Z \sin\theta \qquad\qquad 6\text{-}3$$

where (θ,λ) denote the co-latitude and longitude respectively, ΔX, ΔX and ΔX are the estimated geocenter motion.

For GRACE, the formula is:

$$\Delta(\theta,\lambda) = \frac{a\rho_E}{3}\sum_{n=0}^{\infty}\left(\frac{2n+1}{1+k_n^{'}}\right)\sum_{m=0}^{n}\left[\Delta\bar{C}_{nm}\cos m\lambda + \Delta\bar{S}_{nm}\sin m\lambda\right]\bar{P}_{nm}(\cos\theta) \qquad 6\text{-}4$$

where a is the radius of the Earth, (θ,λ) denote the co-latitude and longitude respectively, $k_n^{'}$ is the load Love number, n and m are the degree and order. $\Delta\bar{C}_{nm}$ and $\Delta\bar{S}_{nm}$ are the degree n order m spherical harmonic coefficients (SHCs). $\bar{P}_{nm}$ is normalized associated Legendre functions.

In this case $n=1$,

$$\left\{\Delta\bar{C}_{11},\Delta\bar{S}_{11},\Delta\bar{C}_{10}\right\} = \frac{\{\Delta X,\Delta Y,\Delta Z\}}{\sqrt{3}a} \qquad\qquad 6\text{-}5$$

Combining equation (6-4) and (6-5), we could compute the geocenter motion effect for GRACE observations. Note that the load Love number is dependent on the frame used [*Blewitt*, 2003].

Table 6.12 Simulation study of effect of geocenter motion (Center of Mass (CM) relative to Center of Figure (CF)) on sea-level variation over study region.

ΔX (mm/yr)	ΔY (mm/yr)	ΔZ (mm/yr)	Sea-level change (mm/yr)	Ocean mass component (mm/yr)
1	0	0	−0.12	−0.52
0	1	0	−0.08	−0.36
0	0	1	−0.15	−0.65
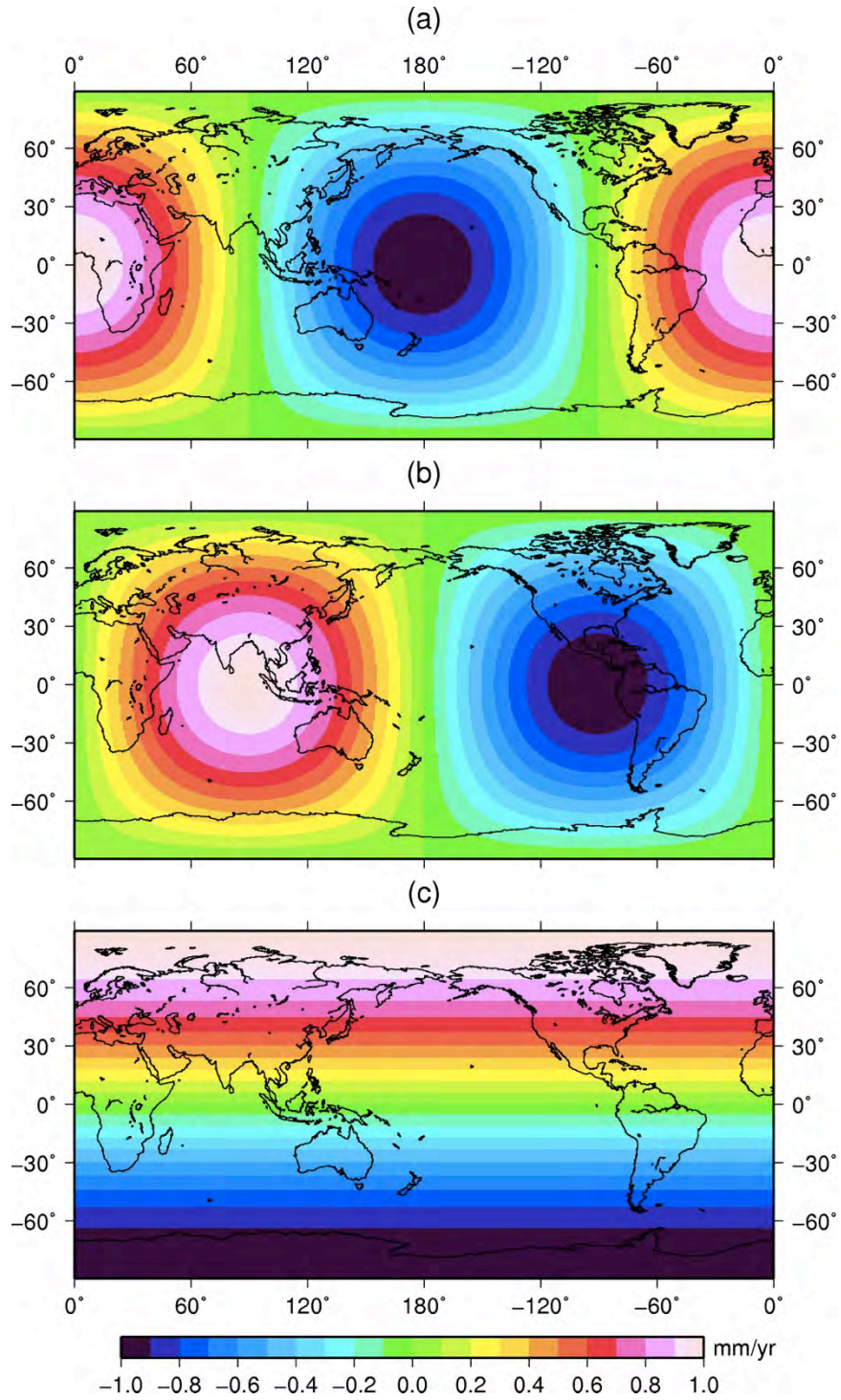
Figure 6.26 Effect of geocenter motion on sea level variation observed by altimetry. (a) $\Delta X = 1$ mm/yr, $\Delta Y = 0$ m/yr, $\Delta Z = 0$ mm/yr; (b) $\Delta X = 0$ mm/yr, $\Delta Y = 1$ m/yr, $\Delta Z = 0$ mm/yr; (c) $\Delta X = 0$ mm/yr, $\Delta Y = 0$ mm/yr, $\Delta Z = 1$ mm/yr.
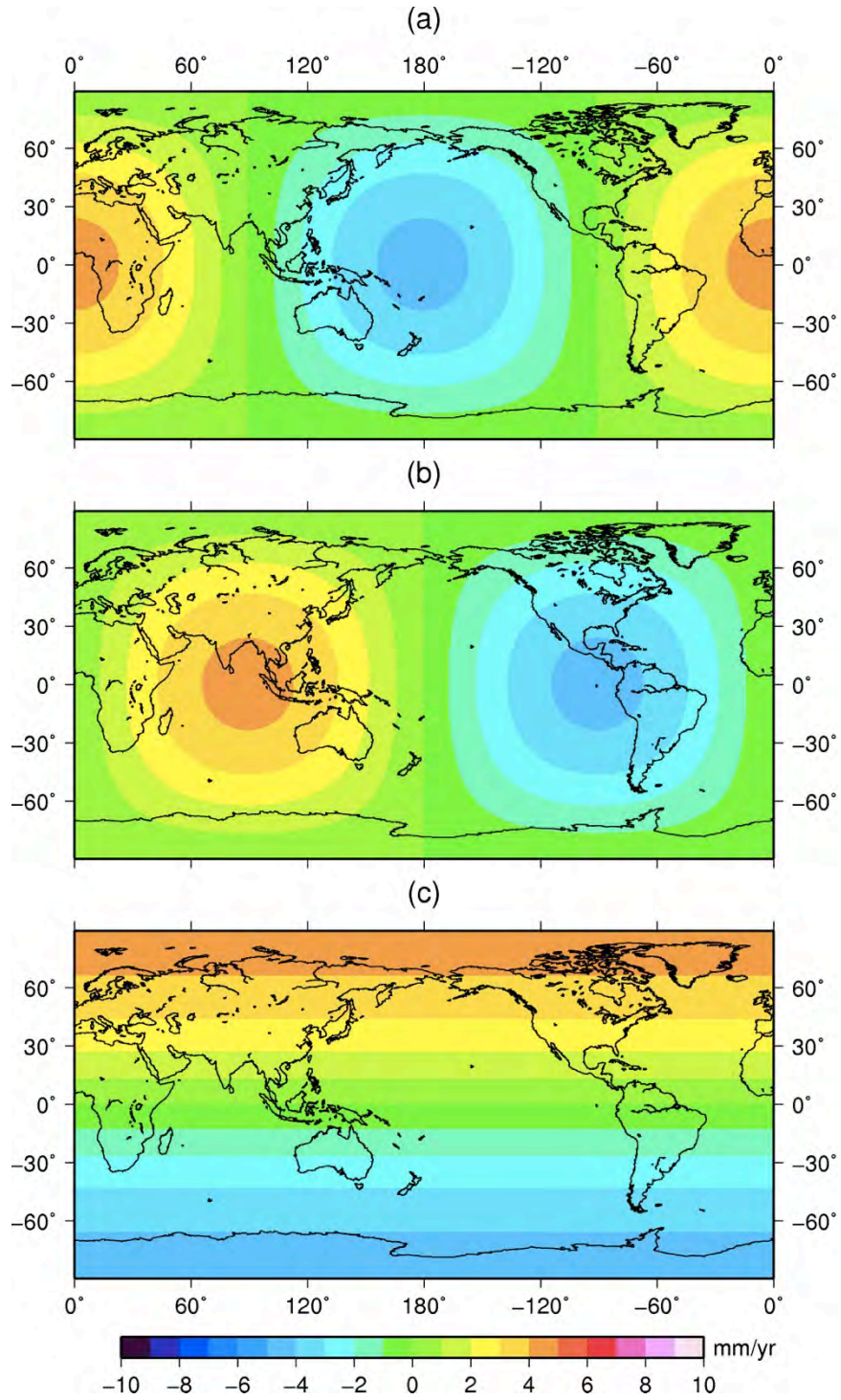
Figure 6.27 Effect of geocenter motion on ocean mass component for GRACE. (a) $\Delta X = 1$ mm/yr, $\Delta Y = 0$ m/yr, $\Delta Z = 0$ mm/yr; (b) $\Delta X = 0$ mm/yr, $\Delta Y = 1$ m/yr, $\Delta Z = 0$ mm/yr; (c) $\Delta X = 0$ mm/yr, $\Delta Y = 0$ mm/yr, $\Delta Z = 1$ mm/yr.

6.3.3 C_{20} Replacement in GRACE

In GRACE data processing, the spherical harmonic coefficient C_{20} is widely replaced by that derived from Satellite Laser Ranging (SLR) following the suggestion of *Chambers* [2006]. The effect of this replacement to GRACE derived ocean mass component is summarized in Table 6.13. For the GFZ solution, it was suggested that C_{20} should not be replaced by SLR-derived values due to the fact it was already replaced in the GRACE RL05 data generating process (This has been discussed in detail in Chapter 5).

It was shown in Figure 6.28 that the effect of C_{20} replacement by SLR derived values. After the replacement, the phases agree between GRACE and steric-corrected altimetry results. In this case, we use the CSR solution with Pel_5_VM2_R model corrected for both radar altimetry and GRACE observations.

Table 6.13 Effect of replacement of C_{20} on ocean bottom pressure over the study region.

Data	OBP (mm/yr)
SLR C_{20}-CSR C_{20}	−0.59
SLR C_{20}-GFZ C_{20}	−0.24
SLR C_{20}-JPL C_{20}	−0.67
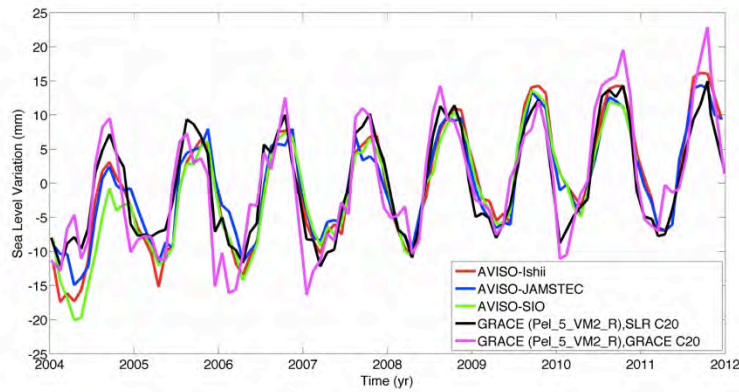
Figure 6.28 Effect of C_{20} replacement on time series of ocean mass component.

6.4 GIA Separation over Ocean

Ocean floor deformation due to GIA is still ongoing, and both GRACE and radar altimetry will be sensitive to this effect. Thus, it is necessary to remove this effect before studying the climate-related sea-level change.

The contribution of the ocean floor to radar altimeter measurement is the ocean floor deformation that will change the surface of the ocean, and along with GIA process, the mantle materials redistribution causes the change in the gravity field that will be in the GRACE measurement. Due to the different characteristic of this GIA effect to the measurement, in principle it is possible to separate the GIA effect from the present day mass change contribution to sea-level rise.

The formulations shown bellow are provided to this study, courtesy Junyi Guo, The Ohio State University, and Chungyen Kuo, National Cheng Kung University, Taiwan [*Pers. Comm.*, unpublished manuscript].

6.4.1 Notations

- δh_{SL}^{ALT} : Steric-corrected altimetry measured sea-level change (relative to the terrestrial reference frame).
- δh_{SL}^{TG} : Steric-corrected tide gauge measured sea-level change (relative to the ocean bottom, could be understood as the change due to ocean water mass change).
- δu_{CU}^{GIA} : Crustal uplift due to GIA.
- δu_{CU}^{EL} : Crustal uplift due to elastic loading resulting from present-day mass change.
- δg_{FM}^{GRACE} : GRACE measured free air gravity change, mass contributions only. This is in fact the total free air gravity change (mass contributions only).
- δg_{FM}^{GIA} : GIA contribution to free air gravity change, mass contribution only.
- δg_{FM}^{SL} : Sea level contribution to free air gravity change, mass contribution only (direct effect).
- δg_{FM}^{EL} : Elastic loading contribution to free air gravity change, mass contribution only (indirect effect to present day mass change).
- ρ_W : Density of water.
- ρ_{UM} : Density of upper mantle.

6.4.2 Basic Relations

The basic assumption is that GRACE measured gravity change includes only the contribution of mass changes in the Earth, land water storage and GIA.

$$\delta h_{SL}^{ALT} - \delta h_{CU}^{EL} = \delta h_{SL}^{TG} + \delta h_{CU}^{GIA} \qquad \text{6-6}$$

$$\delta g_{FM}^{GRACE} - \delta g_{FM}^{EL} = \delta g_{FM}^{SL} + \delta g_{FM}^{GIA} \qquad \text{6-7}$$

$$\delta g_{FM}^{SL} = 2\pi G \rho_W \bullet \delta h_{SL}^{TG} \qquad \text{6-8}$$

$$\delta g_{FM}^{GIA} \approx 2\pi G \rho_{UM} \bullet \delta u_{CU}^{GIA} \qquad \text{6-9}$$

In (6-9), *Wahr et al.* [1995] provides another relation $\delta g_{FM}^{GIA} \approx \alpha \times \delta u_{CU}^{GIA}$ with $\alpha \approx 0.154 \, \mu gals \, / \, mm$ determined by GIA models within a range of Earth parameters.

Substitute (6-8) and (6-9) into (6-7), and combine with (6-6), we have:

$$\begin{bmatrix} \delta h_{SL}^{ALT} - \delta u_{CU}^{EL} \\ \delta g_{FM}^{GRACE} - \delta g_{FM}^{EL} \end{bmatrix} = \begin{bmatrix} 1 & 1 \\ 2\pi G \rho_W & 2\pi G \rho_{UM} \end{bmatrix} \begin{bmatrix} \delta h_{SL}^{TG} \\ \delta U_{CU}^{GIA} \end{bmatrix} \qquad \text{6-10}$$

118

To obtain $\begin{bmatrix} \delta h_{SL}^{TG} \\ \delta U_{CU}^{GIA} \end{bmatrix}$, using simple algebra, yields to:

$$\begin{bmatrix} \delta h_{SL}^{TG} \\ \delta U_{CU}^{GIA} \end{bmatrix} = \begin{bmatrix} 1 & 1 \\ 2\pi G \rho_W & 2\pi G \rho_{UM} \end{bmatrix}^{-1} \begin{bmatrix} \delta h_{SL}^{ALT} - \delta u_{CU}^{EL} \\ \delta g_{FM}^{GRACE} - \delta g_{FM}^{EL} \end{bmatrix}$$

$$6\text{-}11$$

Solve (6-11), we have:

$$\delta h_{SL}^{TG} = \frac{\delta g^{GRACE} - \delta g_{FM}^{EL}}{2\pi G (\rho_W - \rho_{UM})} + \left(-\frac{\rho_W}{\rho_W - \rho_{UM}} \right) \times \left(\delta h_{SL}^{ALT} - \delta u_{CU}^{EL} \right)$$

$$6\text{-}12$$

$$\delta u_{CU}^{GIA} = \frac{\delta g^{GRACE} - \delta g_{FM}^{EL}}{2\pi G (\rho_{UM} - \rho_W)} + \left(\frac{\rho_{UM}}{\rho_W - \rho_{UM}} \right) \times \left(\delta h_{SL}^{ALT} - \delta u_{CU}^{EL} \right)$$

$$6\text{-}13$$

In this study, two cases of α are considered in the computation.

1. The **CASE 1** is: $1/\alpha = 6.5\, mm\, /\, \mu$gals [*Wahr et al.*, 1995].
2. The **CASE 2** is: $1/\alpha = 5.23\, mm\, /\, \mu$gals , this ratio is calculated from all the GIA models, and as an average of all point ratios over the altimetry result coverage (light blue area in Figure 6.30).

6.4.3 Data Analysis

GRACE CSR Level-2 RL05 product (2003.01 to 2011.12), GAC is added back to account for the geopotential changes due to variations in the atmosphere and ocean that is removed from in GRACE processing. Degree 1 coefficients from JPL Tellus are added for the geocenter correction. The C_{20} coefficients are replaced by the values derived using satellite laser ranging (SLR). Other procedures such as de-correlation and leakage reduction are applied. A 600 km Gaussian smoothing is also applied.

Ishii (0–1500m) steric-corrected altimeter result from 2003.01 to 2011.12 is used. For the GIA model, Peltier's ICE5G (VM2) that is updated in 2012 is used.

All the computation and separation are conducted in the spatial domain.

6.4.4 Iteration Procedures

The objective is to separate the mass component and GIA contribution of sea level change. This could be one way to quantify which GIA model provides the 'best' prediction, that is, after correct elastic loading, the 'best' GIA model prediction and the estimation over ocean has the smallest misfits.

1. In the first iteration, the elastic loading effect δu_{CU}^{EL} and δg_{FM}^{EL} are ignored. First solve (6-11) and obtain the initial result of δh_{SL}^{TG} and δu_{CU}^{GIA}.
2. Then δh_{SL}^{TG} is combined with GRACE-derived mass change as the input to the elastic loading computation (See Figure 6.30).
3. The elastic responses of the Earth to its surface loading are computed in terms of the vertical displacement and gravity changes according to the elastic loading

119

theory described in Chapter 2. These results are then being used into (6-11) to perform another iteration.

4. The newer estimate of δh_{SL}^{TG}, then combined with the GRACE-derived mass change over land (here, the GRACE-derived mass change also need to remove the elastic effect obtained from previous elastic loading computation) to conduct another elastic loading computation, and the outputs are used to do another iteration to estimate the δh_{SL}^{TG} and δu_{CU}^{GIA}.

5. The criteria for the iteration are chosen to make sure that the elastic effect should be stable, and the difference of δh_{SL}^{TG} and δu_{CU}^{GIA} between two iterations are less than 0.1% of the signals themself.

6.4.5 Ocean GIA Separation Results

After iterations, results are stable and shown as in Figure 6.31, Figure 6.32, Table 6.14 and Table 6.15.

For two cases, the iteration results are:

CASE 1:

δh_{SL}^{TG} :   2.39 **mm/yr**

δu_{CU}^{GIA} :   −0.65 **mm/yr**

δu_{CU}^{EL} :   −0.17 **mm/yr**

δg_{FM}^{EL} :   −0.014 **µgal/yr**

CASE 2:

δh_{SL}^{TG} :   2.23 **mm/yr.**

δu_{CU}^{GIA} :   −0.49 **mm/yr**

δu_{CU}^{EL} :   −0.16 **mm/yr**

δg_{FM}^{EL} :   −0.018 **µgal/yr**

6.4.6 Discussion

The estimated averaged ocean GIA crustal uplift ranges from –0.65 mm/yr to –0.49 mm/yr, compared to –0.29±0.08 mm/yr that is averaged using an ensemble of 14 GIA models. In the geographical plot (Figure 6.31 and Figure 6.32), the pattern of the estimated GIA uplift are similar in the regions which has larger GIA signals, such as the Scandinavia, ocean near Svalbard Island and Hudson Bay. This could be seen in Figure 6.33, in which the differences between the estimated ocean GIA uplift from this study and that from model prediction (Peltier's ICE5GVM2 model). For regions like Scandinavia and ocean near Svalbard Island, case 1 provides the similar result with the model prediction while case 2 provides the most similar result in Hudson Bay (Figure 6.34 and Figure 6.35)

For the other regions, the pattern of estimated ocean GIA uplift is negatively correlated to the estimated present day sea-level change. It could be the reason that for the regions that GIA signal is small, it is difficult to separate this GIA signal with present day mass change signal, given the uncertainty of measurement is almost the same amplitude with the GIA signal itself.

The estimated present-day ocean mass change causing sea level to rise between 2.23 to 2.39 mm/yr, as opposed to the steric-corrected sea level change from radar altimetry observations at 1.52 mm/yr. Present-day ocean mass component estimated from this study is also compared with that estimated from tide gauge records using the same time span. It was shown in Figure 6.36 that most of the signs are consistent with each other, but the amplitudes differ from each other due to the short time span used in the estimation.
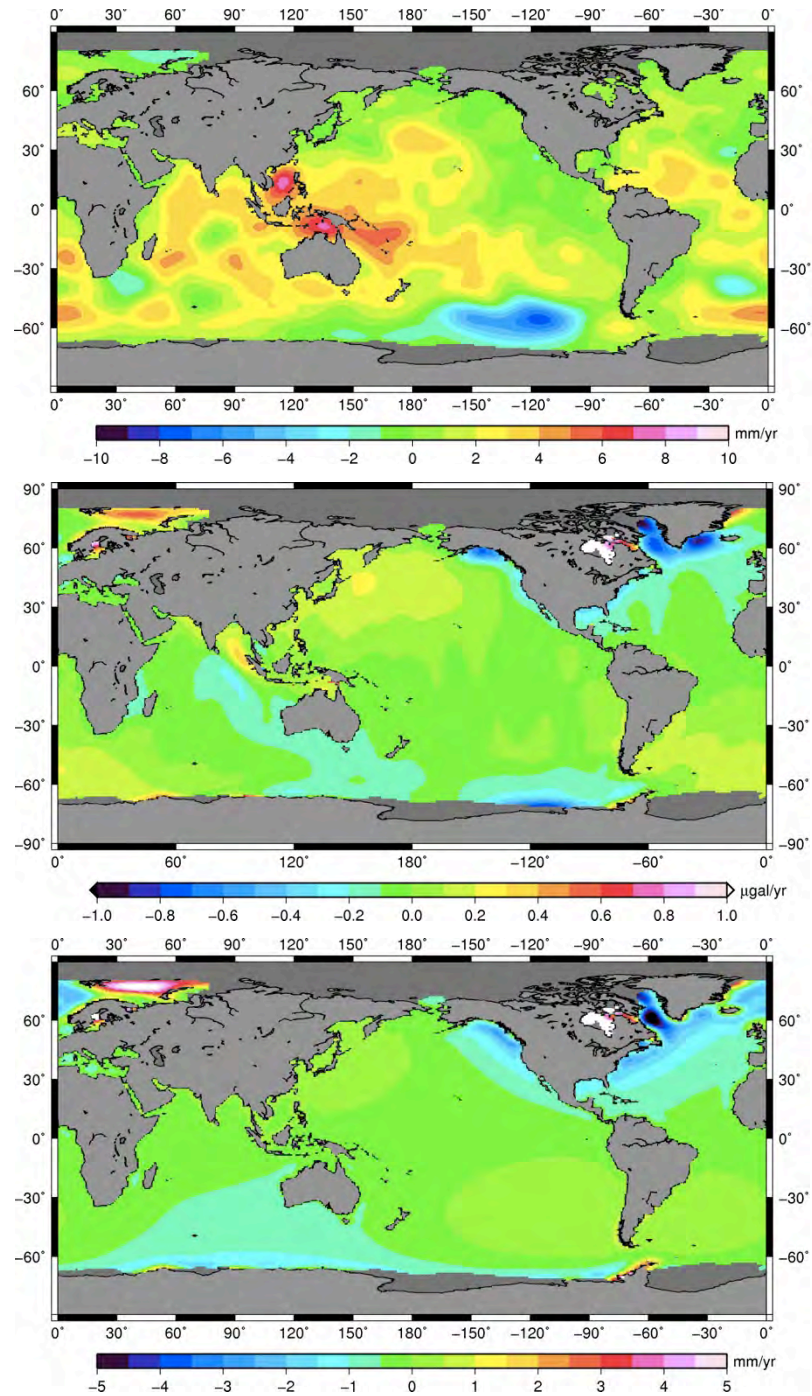
Figure 6.29 Before iteration. Up: Steric-corrected sea-level change rate; Middle: GRACE-derived gravity change rate (CSR RL05, 600 km Gaussian smoothing). Bottom: GIA prediction of uplift rate (Peltier ICE5GVM2 GIA model).
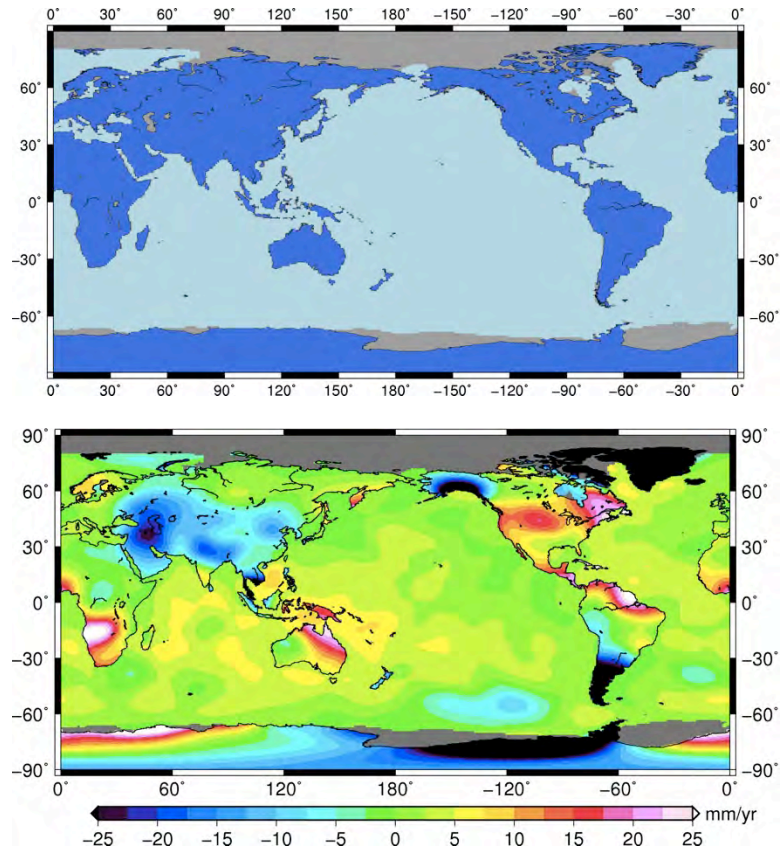
Figure 6.30 Top: Mask of input signals (Light blue: altimetry data, Blue: GRACE-derived mass change, Peltier's ICE5GVM2 GIA model applied). Bottom: Input signals for elastic loading computation (ocean mass variation varies in each iteration, here it is from the last iteration of case 1).

Figure 6.31 Case 1 ($1/\alpha$ =6.5 mm/μgals): Results after iteration. Top: Present day mass induced sea-level change; Bottom: GIA contribution in terms of uplift.

Table 6.14 Case 1 ($1/\alpha$ =6.5 mm/μgals): GIA separation iteration, results are averaged over altimetry result coverage.

Iteration	1	2	3	4	5
δh_{SL}^{TG} (mm/yr)	2.28	2.23	2.39	2.40	2.39
δu_{CU}^{GIA} (mm/yr)	–0.71	–0.66	–0.66	–0.65	–0.65
δu_{CU}^{EL} (mm/yr)	0.003	-0.16	–0.17	–0.17	–0.17
δg_{FM}^{EL} (μgal/yr)	–0.006	–0.012	–0.014	–0.014	–0.014
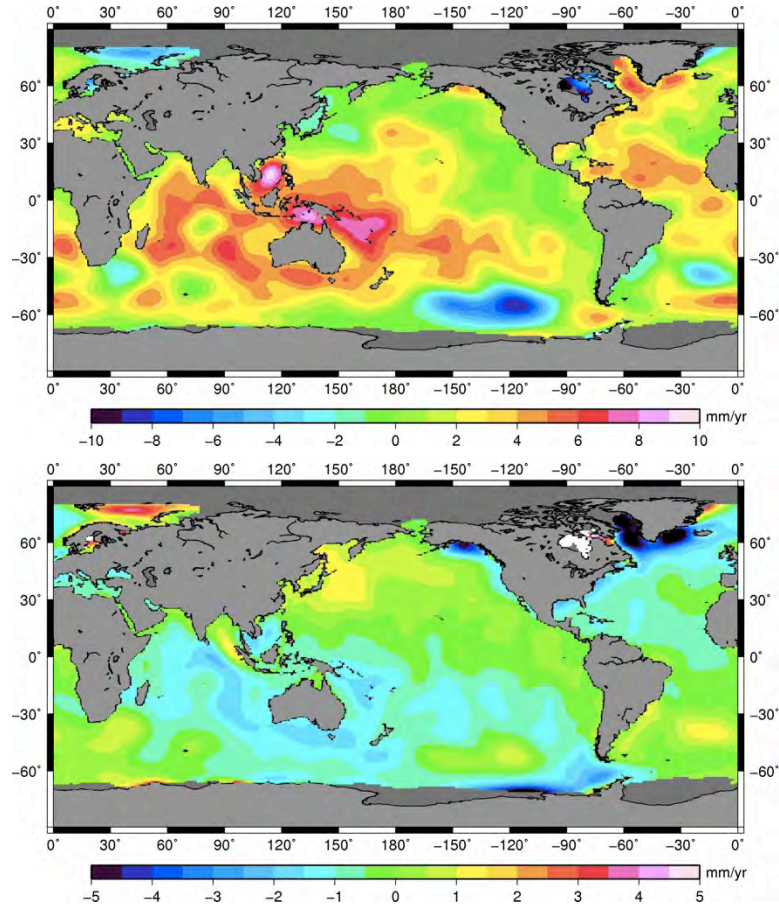
Figure 6.32 Case 2 (1/α =5.23 mm/μgals): results after iteration. Top: Present day mass induced sea-level change; Bottom: GIA contribution in terms of uplift.

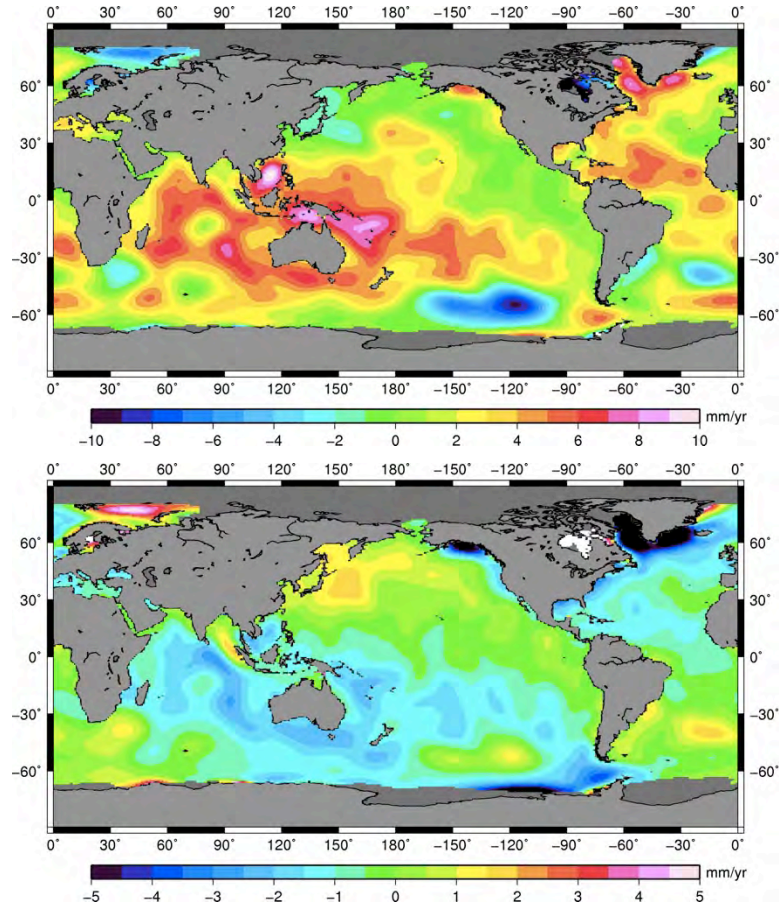Table 6.15 GIA separation iteration, results are averaged over altimetry result coverage. (Case 2: 1/α =5.23 mm/μgals), this ratio is computed from all the GIA models as an average of all the point ratios over altimetry result coverage.

Iteration	1	2	3	4	5
δh_{SL}^{TG} (mm/yr)	2.11	2.07	2.22	2.23	2.23
δu_{CU}^{GIA} (mm/yr)	–0.54	–0.50	–0.50	–0.49	–0.49
δu_{CU}^{EL} (mm/yr)	–0.003	–0.147	–0.159	–0.160	–0.160
δg_{FM}^{EL} (μgal/yr)	–0.006	–0.012	–0.013	–0.013	–0.013
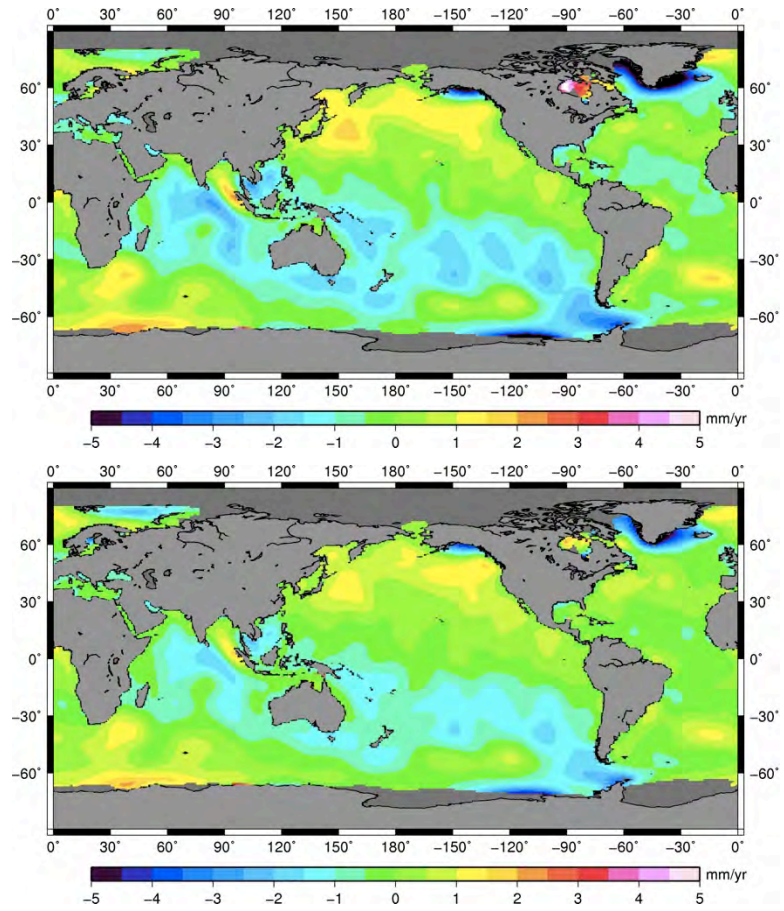
Figure 6.33 Differences between estimated ocean GIA uplift (this study) and predicted ocean GIA uplift. Top: Case 1 ($1/\alpha$ =6.5 mm/μgals); Bottom: Case 2 ($1/\alpha$ =5.23 mm/μgals).
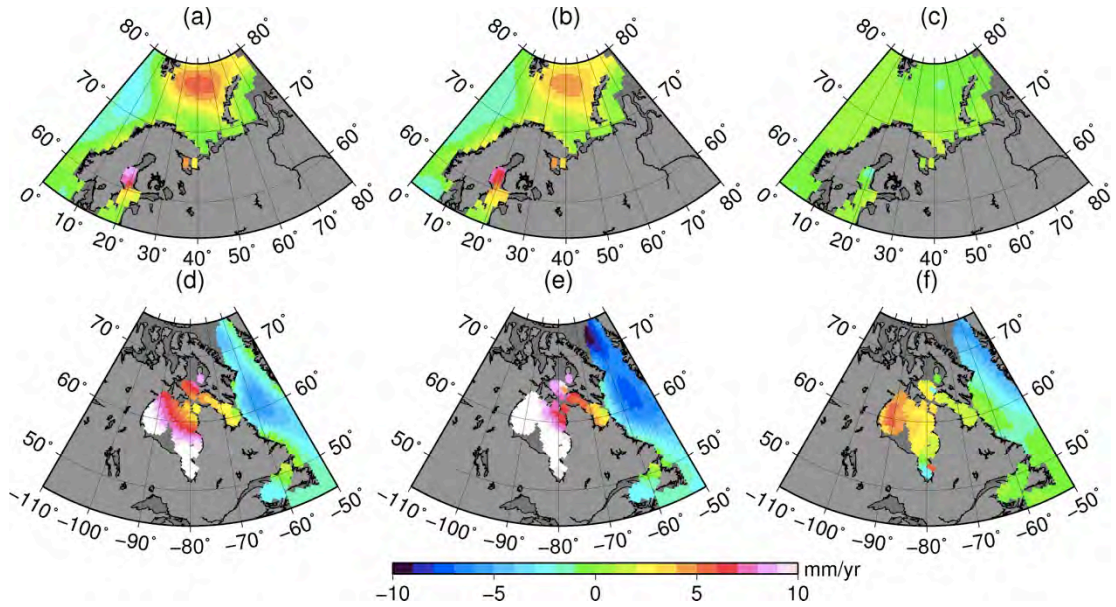
Figure 6.34 Comparison of ocean GIA uplift between this study (left) and model prediction from Peltier ICE5GVM2 (middle) and also the differences (right) over Scandinavia (Top) and Hudson Bay (Bottom). Case 1 (1/α =6.5 mm/μgals)
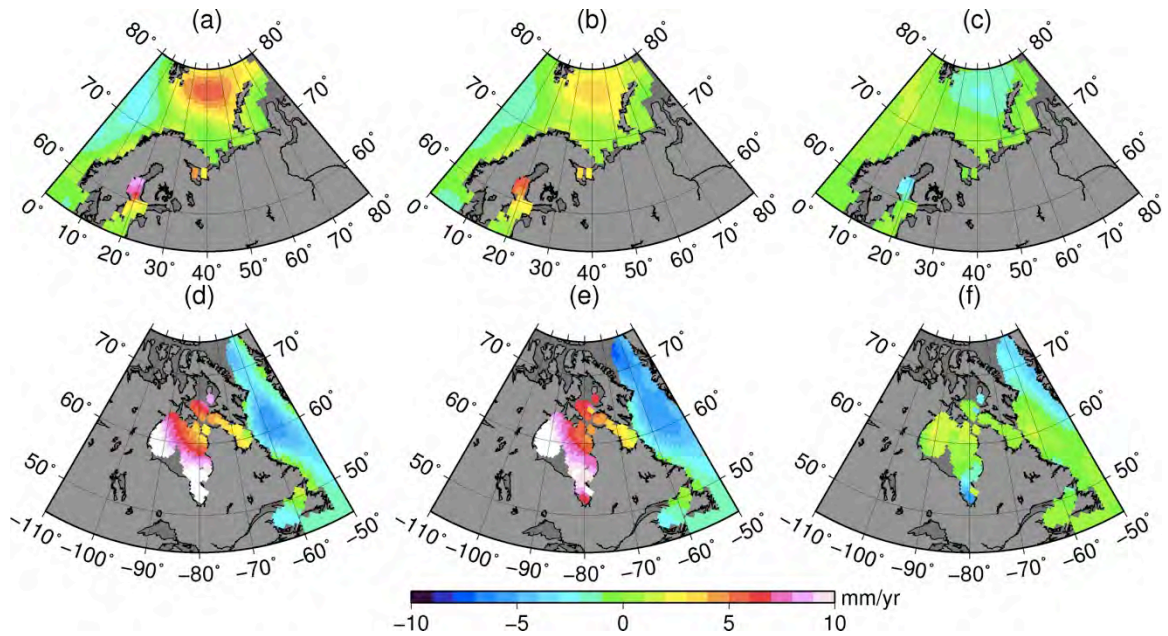
Figure 6.35 Comparison of ocean GIA uplift between this study (left) and model prediction from Peltier ICE5GVM2 (middle) and also the differences (right) over Scandinavia (Top) and Hudson Bay (Bottom). Case 2 (1/α =5.23 mm/μgals)
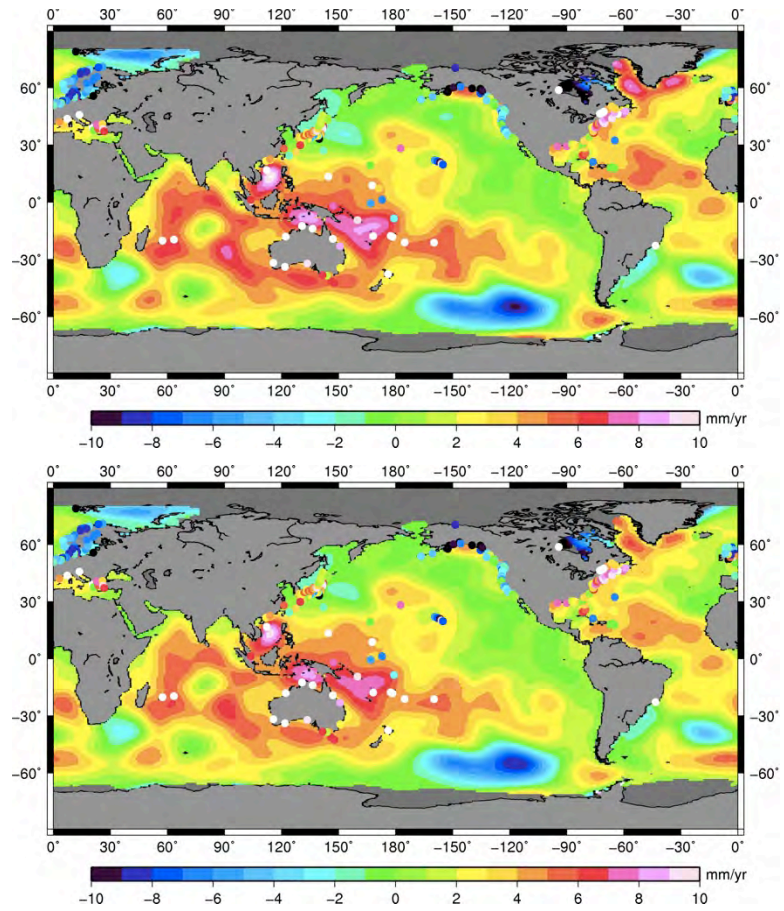
Figure 6.36 Comparison of mass component between the estimation from this separation and estimation derived from tide gauge records using the same time span. Top: Case 1 (1/α =6.5 mm/μgals); Bottom: Case 2 (1/α =5.23 mm/μgals).

6.5   Chapter Summary

To sum up, the ocean mass component of sea-level budget closure is still an open problem from our investigation above. The discrepancies between sea-level change from steric-corrected satellite altimetry sea-level change and GRACE-derived ocean bottom pressure may caused by:

1. Deep ocean steric effect
   This is limited by the availability of in-situ observations. The deep ocean (depth >700m) contribution could be 1.1 mm/yr from 1993 to 2008 according to *Song and Colberg* [2011].
2. Effect of geocenter motion
   Determination of geocenter motion is still an open question. The effects of geocenter motion on both radar altimetry and GRACE measurement are still unknown. From the simulation study and recent geocenter motion estimation, the discrepancy still cannot be explained.
3. Effect of C_{20} replacement
   Although after replacement, the phases seem to fit each other between the steric-corrected sea-level change and GRACE-derived ocean mass component, it still has a problem with these C_{20} replacements. This replacement could cause a change of 0.60 mm/yr in the estimated trend that is almost half of the total.
4. Effect of GIA
   GIA contribution to ocean mass component of mean sea-level change is dominant in the trend. GIA model is different with each other and its accuracy is depending on both the ice loading history and Earth model, which are far way from determined. It is vital to develop a more accurate and more appropriate GIA model for all these use.

About the ocean GIA separation, it was shown that in the regions where GIA signal is strong, the estimated GIA uplift from the separation is comparable with the prediction from GIA forward modeling. In other regions, however, the result does not fit well with the model prediction. Conclusions on the ocean GIA separation are summarized as follows:

1. Limitation is still the quality of data used in the separation, such as the accuracy of GRACE-derived gravity change rates, and also the steric-corrected sea level change from satellite altimetry.
2. Replacing C_{20} using SLR-derived values or not, cause a difference about 0.04 mm/yr in the final result.
3. From the two cases, results show that the value of the ratio between the uplift-gravity relationships used is important. When using different ratios derived from GIA models that may cause 30 percent changes in the result. Different ratios may indicate the spatial variation of rheology parameters. For the two cases, the residuals of this study after subtracting model prediction show that, over Scandinavia and ocean near Svalbard Island, Case 1 agrees more with the model prediction than Case 2 while the result of Hudson Bay agrees more in Case 2 than Case 1.

4. Elastic loading effect play a relatively small role in the iteration, considering this effect cause a change less than 10 percent in the final result.
5. The estimated present-day ocean mass change causing sea level to rise at a range of 2.23 to 2.39 mm/yr, as compared with the steric-corrected sea level change from radar altimetry observations at 1.52 mm/yr. The estimated averaged ocean GIA crustal uplift ranges from –0.49 to –0.65 mm/yr, which is larger than the value of –0.29±0.08 mm/yr which is the average of the predicted values using an ensemble of 14 GIA models.

Chapter 7   Conclusions

With about 200 million people living within the coastal region that is less than 1 meter above current sea level, sea-level rise becomes one of the major social-economic hazards associated with global warming. The 20th and the onset 21st century global sea-level signal is measurable by using geodetic observations including tide gauge and radar altimetry. However, quantifying and understanding the causes of the small rate of the sea-level rise at ~2 mm/yr remains challenging.

With the deployment of global *in situ* hydrographic observations (Argo) since 2004, which is an update from the XBT/MBT hydrographic data that started from the 1950s, continuous repeat-track satellite radar altimeter measurements since 1992, and temporal gravity field measurements from space-borne gravimetry mission (GRACE), our study focuses on addressing whether one could explain the sea-level budget closure for the ocean mass component of the present-day sea-level rise.

Geodetic measurements, including tide gauge, radar altimetry and GRACE, are contaminated by the ongoing glacial isostatic adjustment (GIA) process that is the response of the Earth system to changes in ice and ocean loading during a glacial cycle. Traditionally GIA effect is removed by using a GIA forward model prediction from various geodetic observations including sea-level and ice-sheet mass balance measurements. The limitation in accuracy of the GIA models, in our studies, has prevented more accurate measurements of ice-sheet mass balance, especially over Antarctica, and GRACE measurements of ocean bottom pressure change.

In this dissertation, we have accomplished the following goals and they are summarized as follows:

1. We have described the theoretical treatment of how the GIA effect should be specifically addressed on various geodetic observations for global sea-level and ice-sheet mass balance measurements, including treatment for tide gauge, radar altimetry and GRACE. *Huang et al.* [2013] used Arctic Ocean as an example to demonstrate how to properly correct GIA for the above mentioned three data types to study Arctic sea-level rise. In addition to an updating similar work by *Tamisiea* [2011], we argue that, besides the additional centrifugal potential related to GIA induced polar drift that does not influence GRACE observations, the contribution of the GIA caused polar drift to the pole tide under the assumption of elastic solid Earth's response should not be removed because it has already been done in the GRACE data processing when removing the effect of pole tide. This work has been published by *Guo et al.* [2012].

2. We used an ensemble of 15 predicted/estimated GIA models as a means to estimate the current uncertainty in the GIA models. Here we also address the validity of two approximate inherent relations about the viscous contribution of GIA published by *Wahr et al.* [1995]. We find that this relationship is approximately correct globally for most of the models with ~ 20% discrepancy,

131

however significant differences exist in published GIA models [*Guo et al.*, 2012]. In addition, this study uncovered a possible error in one of the most commonly used GIA model ICE5G(VM2), which has since then updated by the author.

3. We have summarized recent studies and dispute the claim of ocean mass component of the sea-level budget, approximately from 2002 to present, have been effectively closed. We argue that the dominant errors preventing the sea-level budget "closure" is the accuracy of the GIA model, followed by short data spans, and errors in the observations (Argo, satellite altimetry and GRACE) [*Huang et al.*, 2012; *Shum et al.*, 2012].

4. We assessed and quantified the dominant effort of the degree 2 zonal coefficient (J_2) or the Earth's oblateness change, on both ice-sheet mass balance and ocean mass variation estimates, in light of the fact that GRACE's J_2 is poorly constrained. We use the sea-level fingerprint method based on elastic loading theory to interpret recent changes in J_2 resulting from current ice-sheet and mountain glacier/ice cap mass losses into the ocean. Sensitivity test is conducted using published and our estimates of present-day land ice loss on the effect of J_2. Results show that mass losses from Antarctica and Greenland are still the major contributors that is consistent with a previous study by *Nerem and Wahr* [2011]. However, our study shows that the mass losses from the Canadian Arctic Archipelago and Alaska glacier/ice caps also contributed to the recent changes of J_2 which is not negligible. This method potentially could serve as an alternate means of projection of the mass component of future sea-level rise.

5. We adopted the approximate relationship found by *Wahr et al.* [1995] as the constraint and have implemented an innovative method to separate GIA and present-day mass change signals by combining GRACE and steric-corrected radar altimetry observations over the ocean, while assuming the geocenter motion is known and perfectly corrected. Elastic loading effect as the criteria for iteration is removed from both observations. The estimated present-day ocean mass change causing sea level to rise between 2.23 to 2.39 mm/yr, as opposed to the steric sea level change from radar altimetry observations at 1.52 mm/yr. The estimated averaged ocean GIA crustal uplift ranges from –0.49 to –0.65 mm/yr, which is comparable to –0.29±0.08 mm/yr that is averaged using an ensemble of 14 GIA models. It was shown that in the regions where GIA signal is strong, the estimated GIA uplift from the separation is comparable with the prediction from GIA forward modeling. In other regions, however, the result does not fit well with the model prediction. The limitations include the short data span, errors in the observations including hydrogaphic data did not adequately sample the full depth of the ocean or in time, lack of accurate sea-level measurements from satellite altimetry over permanently or seasonally covered polar oceans, Argo data and GRACE data, and mismodeling of the geocenter motion effects. We demonstrate the first possibility to separate GIA and present-day mass change, which would lead to the exact closure of the ocean mass component of the global sea-level rise budget.

132

Further improved understanding of global sea-level rise and its geophysical causes lies in the availability of more accurate measurements with much increased data spans, and also the refinement of the necessary corrections, such as GIA. Future work includes the improvement of the validation and accuracy assessment of the ocean GIA separation and present-day ocean mass trend, and the study of possible estimates of the gravity rate and uplift relationship to optimize the separation of GIA and present ocean mass change.

Bibliography

Benjamin, D., J. Wahr, R. D. Ray, G. D. Egbert, and S. D. Desai (2006), Constraints on mantle anelasticity from geodetic observations, and implications for the J(2) anomaly, *Geophys J Int*, *165*(1), 3-16.

Bindoff, N. L., et al. (2007), Observations: oceanic climate change and sea level. *Rep. 0521880092*, United Kingdom and New York, NY, USA.

Blewitt, G. (2003), Self-consistency in reference frames, geocenter definition, and surface loading of the solid Earth, *J Geophys Res-Sol Ea*, *108*(B2).

Cazenave, A., and W. Llovel (2010), Contemporary Sea Level Rise, *Annu Rev Mar Sci*, *2*, 145-173.

Cazenave, A., K. Dominh, S. Guinehut, E. Berthier, W. Llovel, G. Ramillien, M. Ablain, and G. Larnicol (2009), Sea level budget over 2003-2008: A reevaluation from GRACE space gravimetry, satellite altimetry and Argo, *Global Planet Change*, *65*(1-2), 83-88.

Chambers, D. P. (2006), Observing seasonal steric sea level variations with GRACE and satellite altimetry, *J Geophys Res-Oceans*, *111*(C3).

Chambers, D. P., and J. Schroter (2011), Measuring ocean mass variability from satellite gravimetry, *J Geodyn*, *52*(5), 333-343.

Chambers, D. P., J. Wahr, and R. S. Nerem (2004), Preliminary observations of global ocean mass variations with GRACE, *Geophys Res Lett*, *31*(13).

Chambers, D. P., J. Wahr, M. E. Tamisiea, and R. S. Nerem (2010), Ocean mass from GRACE and glacial isostatic adjustment, *J Geophys Res-Sol Ea*, *115*.

Chao, B. F., and R. S. Gross (1987), Changes in the Earths Rotation and Low-Degree Gravitational-Field Induced by Earthquakes, *Geophys J Roy Astr S*, *91*(3), 569-596.

Chao, B. F., W. P. Oconnor, A. T. C. Chang, D. K. Hall, and J. L. Foster (1987), Snow Load Effect on the Earths Rotation and Gravitational-Field, 1979-1985, *J Geophys Res-Solid*, *92*(B9), 9415-9422.

Chen, J. L., C. R. Wilson, D. D. Blankenship, and B. D. Tapley (2006), Antarctic mass rates from GRACE, *Geophys Res Lett*, *33*(11).

Cheng, M. K., and B. D. Tapley (2004), Variations in the Earth's oblateness during the past 28 years, *J Geophys Res-Sol Ea*, *109*(B9).

Cheng, M. K., B. D. Tapley, and J. C. Ries (2013), Deceleration in the Earth's oblateness, *Journal of Geophysical Research: Solid Earth*, *118*(2), 740-747.

Church, J. A., and N. J. White (2011), Sea-Level Rise from the Late 19th to the Early 21st Century, *Surv Geophys*, *32*(4-5), 585-602.

Clark, J. A., W. E. Farrell, and W. R. Peltier (1978), Global Changes in Post-Glacial Sea-Level - Numerical-Calculation, *Quaternary Res*, *9*(3), 265-287.

Cox, C. M., and B. F. Chao (2002), Detection of a large-scale mass redistribution in the terrestrial system since 1998, *Science*, *297*(5582), 831-833.

De Linage, C., J. Hinderer, and Y. Rogister (2007), A search for the ratio between gravity variation and vertical displacement due to a surface load, *Geophys J Int*, *171*(3), 986-994.

Devoti, R., V. Luceri, C. Sciarretta, G. Bianco, G. Di Donato, L. L. A. Vermeersen, and R. Sabadini (2001), The SLR secular gravity variations and their impact on the inference of mantle rheology and lithospheric thickness, *Geophys Res Lett*, *28*(5), 855-858.

Dickey, J. O., S. L. Marcus, O. de Viron, and I. Fukumori (2002), Recent Earth oblateness variations: Unraveling climate and postglacial rebound effects, *Science*, *298*(5600), 1975-1977.

Douglas, B. C., and W. R. Peltier (2002), The puzzle of global sea-level rise, *Phys Today*, *55*(3), 35-40.

Duan, X. J., J. Y. Guo, C. K. Shum, and W. van der Wal (2009), On the postprocessing removal of correlated errors in GRACE temporal gravity field solutions, *J Geodesy*, *83*(11), 1095-1106.

Dziewonski, A. M., and D. L. Anderson (1981), Preliminary reference Earth model, *Phys Earth Planet In*, *25*(4), 297-356.

Fang, M., and B. H. Hager (2001), Vertical deformation and absolute gravity, *Geophys J Int*, *146*(2), 539-548.

Farrell, W. E. (1972), Deformation of the Earth by surface loads, *Rev Geophys*, *10*(3), 761-797.

Farrell, W. E., and J. A. Clark (1976), Postglacial Sea-Level, *Geophys J Roy Astr S*, *46*(3), 647-667.

Fleming, K., and K. Lambeck (2004), Constraints on the Greenland Ice Sheet since the Last Glacial Maximum from sea-level observations and glacial-rebound models, *Quaternary Sci Rev*, *23*(9-10), 1053-1077.

Guo, J. Y., X. J. Duan, and C. K. Shum (2010), Non-isotropic Gaussian smoothing and leakage reduction for determining mass changes over land and ocean using GRACE data, *Geophys J Int*, *181*(1), 290-302.

Guo, J. Y., Z. W. Huang, C. K. Shum, and W. van der Wal (2012), Comparisons among contemporary glacial isostatic adjustment models, *J Geodyn*, *61*(0), 129-137.

Guo, J. Y., Y. B. Li, Y. Huang, H. T. Deng, S. Q. Xu, and J. S. Ning (2004), Green's function of the deformation of the Earth as a result of atmospheric loading, *Geophys J Int*, *159*(1), 53-68.

Han, D. Z., and J. Wahr (1989), Postglacial Rebound Analysis for a Rotating Earth, *Slow Deformation and Transmission of Stress in the Earth*, *49*, 1-6.

Hosoda, S., T. Ohira, and T. Nakamura (2008), A monthly mean dataset of global oceanic temperature and salinity derived from Argo float observations, *JAMSTEC Rep. Res. Dev*, *8*, 47-59.

Huang, Z. W., C. K. Shum, J. Y. Guo, J. B. Duan, and C. Y. Kuo (2012), Role of Glacial Isostatic Adjustment Process in the Presetn-Day Sea-Level Budget Closure, in *AUG Fall Meeting*, San Francisco, California, December 3-7, 2012.

Huang, Z. W., J. Y. Guo, C. K. Shum, J. K. Wan, J. B. Duan, H. S. Fok, and C. Y. Kuo (2013), On the accuracy of glacial isostatic adjustment models for geodetic observations to estimate arctic ocean sea-level change, *Terr. Atmos. Ocean. Sci.*, *in press*.

IPCC (2007), Intergovernmental Panel on Climate Change, Climate Change 2007: The Physical Science Basis, Summary for Policymakers.

Ishii, M., and M. Kimoto (2009), Reevaluation of historical ocean heat content variations with time-varying XBT and MBT depth bias corrections, *Journal of Oceanography*, *65*(3), 287-299.

Ivins, E. R., and T. S. James (2005), Antarctic glacial isostatic adjustment: a new assessment, *Antarct Sci*, *17*(4), 541-553.

Jacob, T., J. Wahr, R. Gross, S. Swenson, and A. Geruo (2012), Estimating geoid height change in North America: past, present and future, *J Geodesy*, *86*(5), 337-358.

James, T. S., and E. R. Ivins (1998), Predictions of Antarctic crustal motions driven by present-day ice sheet evolution and by isostatic memory of the Last Glacial Maximum, *J. Geophys. Res.*, *103*(B3), 4993-5017.

Jekeli, C. (1981), Alternative methods to smooth the Earth's gravity field. *Rep. 327*, Ohio state University, Columbus.

Johnston, P. (1993), The Effect of Spatially Nonuniform Water Loads on Prediction of Sea-Level Change, *Geophys J Int*, *114*(3), 615-634.

Kaufmann, G., P. Wu, and G. Y. Li (2000), Glacial isostatic adjustment in Fennoscandia for a laterally heterogeneous earth, *Geophys J Int*, *143*(1), 262-273.

Kemp, A. C., B. P. Horton, J. P. Donnelly, M. E. Mann, M. Vermeer, and S. Rahmstorf (2011), Climate related sea-level variations over the past two millennia, *P Natl Acad Sci USA*, *108*(27), 11017-11022.

Kendall, R. A., J. X. Mitrovica, and G. A. Milne (2005), On post-glacial sea level - II. Numerical formulation and comparative results on spherically symmetric models, *Geophys J Int*, *161*(3), 679-706.

King, M. A., R. J. Bingham, P. Moore, P. L. Whitehouse, M. J. Bentley, and G. A. Milne (2012), Lower satellite-gravimetry estimates of Antarctic sea-level contribution, *Nature*, *advance online publication*.

Knudsen, P. (2003), Ocean tides in GRACE monthly averaged gravity fields, *Space Sci Rev*, *108*(1-2), 261-270.

Lambeck, K., and M. Nakada (1990), Late Pleistocene and Holocene Sea-Level Change Along the Australian Coast, *Global Planet Change*, *89*(1-2), 143-176.

Lambeck, K., C. Smither, and M. Ekman (1998), Tests of glacial rebound models for Fennoscandinavia based on instrumented sea- and lake-level records, *Geophys J Int*, *135*(2), 375-387.

Latychev, K., J. X. Mitrovica, J. Tromp, M. E. Tamisiea, D. Komatitsch, and C. C. Christara (2005), Glacial isostatic adjustment on 3-D Earth models: a finite-volume formulation, *Geophys J Int*, *161*(2), 421-444.

Leuliette, E. W., and L. Miller (2009), Closing the sea level rise budget with altimetry, Argo, and GRACE, *Geophys Res Lett*, *36*.

Leuliette, E. W., and J. K. Willis (2011), Balancing the Sea Level Budget, *Oceanography*, *24*(2), 122-129.

Levitus, S., J. I. Antonov, T. P. Boyer, R. A. Locarnini, H. E. Garcia, and A. V. Mishonov (2009), Global ocean heat content 1955-2008 in light of recently revealed instrumentation problems, *Geophys Res Lett*, *36*.

Marcus, S. L., J. O. Dickey, J. K. Willis, and F. Seitz (2009), Earth oblateness changes reveal land ice contribution to interannual sea level variability, *Geophys Res Lett*, *36*.

Martinec, Z. (2000), Spectral-finite element approach to three-dimensional viscoelastic relaxation in a spherical earth, *Geophys J Int*, *142*(1), 117-141.

Meyssignac, B., M. Becker, W. Llovel, and A. Cazenave (2012), An Assessment of Two-Dimensional Past Sea Level Reconstructions Over 1950-2009 Based on Tide-Gauge Data and Different Input Sea Level Grids, *Surv Geophys*, *33*(5), 945-972.

Milne, G. A. (1998), Refining models of the glacial isostatic adjustment process, Dissertation thesis, University of Toronto, Toronto.

Milne, G. A., and J. X. Mitrovica (1998), Postglacial sea-level change on a rotating Earth, *Geophys J Int*, *133*(1), 1-19.

Mitrovica, J. X., and W. R. Peltier (1991), On Postglacial Geoid Subsidence over the Equatorial Oceans, *J Geophys Res-Sol Ea*, *96*(B12), 20053-20071.

Mitrovica, J. X., and W. R. Peltier (1993), Present-Day Secular Variations in the Zonal Harmonics of Earths Geopotential, *J Geophys Res-Sol Ea*, *98*(B3), 4509-4526.

Mitrovica, J. X., and G. A. Milne (2003), On post-glacial sea level: I. General theory, *Geophys J Int*, *154*(2), 253-267.

Mitrovica, J. X., and J. Wahr (2011), Ice Age Earth Rotation, *Annu Rev Earth Pl Sc*, *39*, 577-616.

Mitrovica, J. X., G. A. Milne, and J. L. Davis (2001), Glacial isostatic adjustment on a rotating earth, *Geophys J Int*, *147*(3), 562-578.

Munk, W. H., and G. J. MacDonald (1960), *The rotation of the earth; a geophysical discussion*, 323 p. pp., University Press, Cambridge Eng.

Nakada, M., and K. Lambeck (1988), The Melting History of the Late Pleistocene Antarctic Ice-Sheet, *Nature*, *333*(6168), 36-40.

Nakada, M., and K. Lambeck (1991), Late Pleistocene and Holocene Sea-Level Change - Evidence for Lateral Mantle Viscosity Structure, *Nato Adv Sci I C-Mat*, *334*, 79-94.

Nerem, R. S., and J. Wahr (2011), Recent changes in the Earth's oblateness driven by Greenland and Antarctic ice mass loss, *Geophys Res Lett*, *38*.

Paulson, A., S. J. Zhong, and J. Wahr (2005), Modelling post-glacial rebound with lateral viscosity variations, *Geophys J Int*, *163*(1), 357-371.

Paulson, A., S. J. Zhong, and J. Wahr (2007), Inference of mantle viscosity from GRACE and relative sea level data, *Geophys J Int*, *171*(2), 497-508.

Peltier, W. R. (1974), Impulse Response of a Maxwell Earth, *Rev Geophys*, *12*(4), 649-669.

Peltier, W. R. (1976), Glacial-Isostatic Adjustment .2. Inverse Problem, *Geophys J Roy Astr S*, *46*(3), 669-705.

Peltier, W. R. (1994), Ice-Age Paleotopography, *Science*, *265*(5169), 195-201.

Peltier, W. R. (1998), Postglacial variations in the level of the sea: Implications for climate dynamics and solid-earth geophysics, *Rev Geophys*, *36*(4), 603-689.

Peltier, W. R. (2001), Global Glacial Isostatic Adjustment and Modern Instrumental Records of Relative Sea Level History, in *Sea Level Rise: History and Consequences*, edited by B. C. Douglas, M. S. Kearney and S. R. Leatherman, p. 31 Academic Press, , San Diego.

Peltier, W. R. (2002), Global glacial isostatic adjustment: palaeogeodetic and space-geodetic tests of the ICE-4G (VM2) model, *J Quaternary Sci*, *17*(5-6), 491-510.

Peltier, W. R. (2004), Global glacial isostasy and the surface of the ice-age earth: The ice-5G (VM2) model and grace, *Annual Review of Earth and Planetary Sciences*, *32*, 111-149.

Peltier, W. R. (2009), Closure of the budget of global sea level rise over the GRACE era: the importance and magnitudes of the required corrections for global glacial isostatic adjustment, *Quaternary Sci Rev*, *28*(17-18), 1658-1674.

Peltier, W. R., and J. T. Andrews (1976), Glacial-Isostatic Adjustment .1. Forward Problem, *Geophys J Roy Astr S*, *46*(3), 605-646.

Peltier, W. R., and A. M. Tushingham (1991), Influence of Glacial Isostatic-Adjustment on Tide-Gauge Measurements of Secular Sea-Level Change, *J Geophys Res-Solid*, *96*(B4), 6779-6796.

138

Peltier, W. R., R. Drummond, and K. Roy (2012), Comment on "Ocean mass from GRACE and glacial isostatic adjustment" by D. P. Chambers et al, *Journal of Geophysical Research: Solid Earth*, *117*(B11), B11403.

Purcell, A., A. Dehecq, P. Tregoning, E. K. Potter, S. C. McClusky, and K. Lambeck (2011), Relationship between glacial isostatic adjustment and gravity perturbations observed by GRACE, *Geophys Res Lett*, *38*.

Rahmstorf, S., A. Cazenave, J. A. Church, J. E. Hansen, R. F. Keeling, D. E. Parker, and R. C. J. Somerville (2007), Recent climate observations compared to projections, *Science*, *316*(5825), 709-709.

Roemmich, D., and J. Gilson (2009), The 2004–2008 mean and annual cycle of temperature, salinity, and steric height in the global ocean from the Argo Program, *Prog Oceanogr*, *82*(2), 81-100.

Roemmich, D., G. C. Johnson, S. Riser, R. Davis, J. Gilson, W. B. Owens, S. L. Garzoli, C. Schmid, and M. Ignaszewski (2009), The Argo Program: Observing the global ocean with profiling floats.

Rubincam, D. P. (1984), Postglacial Rebound Observed by Lageos and the Effective Viscosity of the Lower Mantle, *J Geophys Res*, *89*(Nb2), 1077-1087.

Sasgen, I., V. Klemann, and Z. Martinec (2012), Towards the inversion of GRACE gravity fields for present-day ice-mass changes and glacial-isostatic adjustment in North America and Greenland, *J Geodyn*, *59*, 49-63.

Shepherd, A., et al. (2012), A Reconciled Estimate of Ice-Sheet Mass Balance, *Science*, *338*(6111), 1183-1189.

Shum, C. K., and C. Y. Kuo (2011), Observation and Geophysical Causes of Present-Day Sea-Level Rise, *Climate Change and Food Security in South Asia*, 85-104.

Shum, C. K., and C. Y. Kuo (2013), Climate Change and Sea-Level Rise, edited by Y. Q. Wang, Taylor and Francis.

Shum, C. K., C. Y. Kuo, J. Y. Guo, J. B. Duan, and Z. W. Huang (2012), Present-Day Ocean Sea-Level Budget, in *AOGS-AGU (WPGM) Joint Assembly*, Singapore, August 13-17, 2012.

Simpson, M. J. R., G. A. Milne, P. Huybrechts, and A. J. Long (2009), Calibrating a glaciological model of the Greenland ice sheet from the Last Glacial Maximum to present-day using field observations of relative sea level and ice extent, *Quaternary Sci Rev*, *28*(17-18), 1631-1657.

Song, Y. T., and F. Colberg (2011), Deep ocean warming assessed from altimeters, Gravity Recovery and Climate Experiment, in situ measurements, and a non-Boussinesq ocean general circulation model, *J Geophys Res-Oceans*, *116*.

Spada, G., V. R. Barletta, V. Klemann, R. E. M. Riva, Z. Martinec, P. Gasperini, B. Lund, D. Wolf, L. L. A. Vermeersen, and M. A. King (2011), A benchmark study for glacial isostatic adjustment codes, *Geophys J Int*, *185*(1), 106-132.

Stern, N. H., and G. Britain (2006), *Stern Review: The economics of climate change*, HM treasury London.

Swenson, S., and J. Wahr (2006), Post-processing removal of correlated errors in GRACE data, *Geophys Res Lett*, *33*(8).

Tamisiea, M. E. (2011), Ongoing glacial isostatic contributions to observations of sea level change, *Geophys J Int*, *186*(3), 1036-1044.

Tamisiea, M. E., and J. X. Mitrovica (2011), The Moving Boundaries of Sea Level Change Understanding the Origins of Geographic Variability, *Oceanography*, *24*(2), 24-39.

Tamisiea, M. E., J. X. Mitrovica, and J. L. Davis (2007), GRACE gravity data constrain ancient ice geometries and continental dynamics over Laurentia, *Science*, *316*(5826), 881-883.

Tapley, B. D., S. Bettadpur, M. Watkins, and C. Reigber (2004), The gravity recovery and climate experiment: Mission overview and early results, *Geophys Res Lett*, *31*(9).

Tushingham, A. M., and W. R. Peltier (1991), Ice-3g - a New Global-Model of Late Pleistocene Deglaciation Based Upon Geophysical Predictions of Postglacial Relative Sea-Level Change, *J Geophys Res-Solid*, *96*(B3), 4497-4523.

van der Wal, W., E. Kurtenbach, J. Kusche, and B. Vermeersen (2011), Radial and tangential gravity rates from GRACE in areas of glacial isostatic adjustment, *Geophys J Int*, *187*(2), 797-812.

Velicogna, I., and J. Wahr (2002), A method for separating antarctic postglacial rebound and ice mass balance using future ICESat Geoscience Laser Altimeter System, Gravity Recovery and Climate Experiment, and GPS satellite data, *J Geophys Res-Sol Ea*, *107*(B10).

Velicogna, I., and J. Wahr (2005), Greenland mass balance from GRACE, *Geophys Res Lett*, *32*(18).

Vermeer, M., and S. Rahmstorf (2009), Global sea level linked to global temperature, *Proceedings of the National Academy of Sciences*, *106*(51), 21527-21532.

Wahr, J., H. Dazhong, and A. Trupin (1995), Predictions of Vertical Uplift Caused by Changing Polar Ice Volumes on a Viscoelastic Earth, *Geophys Res Lett*, *22*(8), 977-980.

Wahr, J., M. Molenaar, and F. Bryan (1998), Time variability of the Earth's gravity field: Hydrological and oceanic effects and their possible detection using GRACE, *J Geophys Res-Sol Ea*, *103*(B12), 30205-30229.

Wahr, J., S. Swenson, V. Zlotnicki, and I. Velicogna (2004), Time-variable gravity from GRACE: First results, *Geophys Res Lett*, *31*(11).

Wang, H., and P. Wu (2006), Effects of lateral variations in lithospheric thickness and mantle viscosity on glacially induced surface motion on a spherical, self-gravitating Maxwell Earth, *Earth Planet Sc Lett*, *244*(3-4), 576-589.

Whitehouse, P. L., M. J. Bentley, G. A. Milne, M. A. King, and I. D. Thomas (2012), A new glacial isostatic adjustment model for Antarctica: calibrated and tested using observations of relative sea-level change and present-day uplift rates, *Geophys J Int*, *190*(3), 1464-1482.

Willis, J. K., D. P. Chambers, and R. S. Nerem (2008), Assessing the globally averaged sea level budget on seasonal to interannual timescales, *J Geophys Res-Oceans*, *113*(C6).

Willis, J. K., D. P. Chambers, C. Y. Kuo, and C. K. Shum (2010), Global Sea Level Rise RECENT PROGRESS AND CHALLENGES FOR THE DECADE TO COME, *Oceanography*, *23*(4), 26-35.

Woodworth, P. L., and R. Player (2003), The permanent service for mean sea level: An update to the 21st century, *J Coastal Res*, *19*(2), 287-295.

Wu, P. (2005), Effects of lateral variations in lithospheric thickness and mantle viscosity on glacially induced surface motion in Laurentia, *Earth Planet Sc Lett*, *235*(3-4), 549-563.

Wu, P., and W. R. Peltier (1982), Viscous Gravitational Relaxation, *Geophys J Roy Astr S*, *70*(2), 435-485.

Wu, P., and W. van der Wal (2003), Postglacial sealevels on a spherical, self-gravitating viscoelastic earth: effects of lateral viscosity variations in the upper mantle on the inference of viscosity contrasts in the lower mantle, *Earth Planet Sc Lett*, *211*(1-2), 57-68.

Wu, X. P., M. B. Heflin, H. Schotman, B. L. A. Vermeersen, D. A. Dong, R. S. Gross, E. R. Ivins, A. Moore, and S. E. Owen (2010), Simultaneous estimation of global present-day water transport and glacial isostatic adjustment, *Nat Geosci*, *3*(9), 642-646.

Yoder, C. F., J. G. Williams, J. O. Dickey, B. E. Schutz, R. J. Eanes, and B. D. Tapley (1983), Secular Variation of Earths Gravitational Harmonic J2 Coefficient from Lageos and Nontidal Acceleration of Earth Rotation, *Nature*, *303*(5920), 757-762.

Zhong, S. J., A. Paulson, and J. Wahr (2003), Three-dimensional finite-element modelling of Earth's viscoelastic deformation: effects of lateral variations in lithospheric thickness, *Geophys J Int*, *155*(2), 679-695.

Zwally, H., M. Giovinetto, M. Beckley, and J. Saba (2012), Antarctic and Greenland Drainage Systems, GSFC Cryospheric Sciences Laboratory.